

Abstract

PETRIE, RANDALL JAMES. Polymerization in Confined Geometries. (Under the direction of Professors Christopher B. Gorman and Jan Genzer.)

The work presented in this PhD thesis is centered on nanometer-sized pores. Two detailed objectives include: 1) investigating the confinement effect on “grafting from” polymerization carried out directly inside the pore, and 2) using porous silicon as a novel platform for controlled motion of liquid drops moving along wettability gradients created on the pores. In chapter 2 we investigate the confinement effect of the pore (< 50 nm) on the polymerization of poly methyl methacrylate (PMMA) in porous silicon. Porous silicon has the unique quality of acting as a replacement for the conventional organic matrix used in matrix assisted laser desorption ionization (MALDI). To this end, porous silicon not only acts as the substrate in which the polymerization takes place, but also serves as an in situ platform for the direct molecular weight analysis of the pore-grown polymer. We also report on the efficiency of porous silicon to produce MALDI spectra of PMMA as compared to MALDI spectra obtained using a conventional organic matrix.

Chapter 3 focuses upon the use of an alternative substrate, anodic aluminum oxide (AAO), for the in-pore polymerization of PMMA. AAO is attractive for its homogeneous pore distribution and commercial availability. Although AAO does not serve as an organic matrix replacement for MALDI like porous silicon, a procedure for the ex situ characterization of the pore grown PMMA via MALDI is discussed.

In chapter 4 we report on the motion of water droplets on porous and flat silicon surfaces decorated with molecular gradients comprising semifluorinated (SF) organosilanes. SF molecular gradients deposited on flat silica substrates facilitate faster motion of water droplets relative to the specimens covered with an analogous hydrocarbon gradient. Further increase in the drop speed is achieved by advancing it along porous substrates coated with the SF wettability gradients. The results of our experiments are in quantitative agreement with a simple scaling theory that describes the faster liquid motion in terms of reduced friction at the liquid/substrate interface.

Polymerization in Confined Geometries

by

Randall James Petrie

A dissertation submitted to the Graduate Faculty of
North Carolina State University
in partial fulfillment of the requirements for the Degree of
Doctor of Philosophy

Chemistry

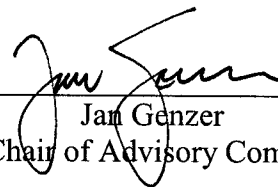
Raleigh, NC, USA

2005

Approved by



Chris B. Gorman
Co-Chair of Advisory Committee



Jan Genzer
Co-Chair of Advisory Committee



Ed Bowden



Kenneth Hanck

DEDICATION

This dissertation is dedicated to my parents, Claude and Janice.

Without their incredible inspiration and unwavering
support this work would not have been possible.

BIOGRAPHY

Randall James Petrie was born on August 30th, 1978 in Reading, PA to Claude and Janice Petrie. He grew up the youngest of three sisters and a brother, Mabelle, Valerie, Jill, and Travis. He graduated from Hamburg Area High School in the top ten of his class in the spring of 1996. He continued his education at the University of Scranton in Scranton, Pa and enrolled in the Chemistry program in the fall of 1996. He completed his B.S. in Chemistry in the spring of 2000. During the last two years at Scranton, he worked for Acton Technologies Inc. in Pittston, Pa. In the fall of 2000, he enrolled in the Masters program of the Chemistry department at North Carolina State University in Raleigh, NC under the direction of Drs. Christopher B. Gorman and Jan Genzer. In the fall of 2002 he decided to continue in his graduate studies in the Chemistry department and complete his Ph.D. He completed his Ph.D in the fall of 2005 while investigating polymer brushes, the characterization of polymer brushes through the utilization of MALDI-DIOS, and the investigation of liquid motion on chemical gradients.

ACKNOWLEDGMENTS

First, I would like to express my gratitude to my mother and father. The support and love they provided and faith they instilled in me has made me the person I am today. I love you both and credit you with all that I am. I was lucky to be the youngest of five wonderful people in my family. My oldest sister, Machele, practically raised me in my younger years. She is now the proud mother of two boys Drew and Mason, whom I wish I were able to be around more. I spent a great deal of time talking to my sister Valerie during the tough times of my journey through graduate school. Thanks for listening Val. My youngest sister Jill inspires me to speak my mind in any situation and absolutely never apologize for who I am. She also is the mother of three beautiful children, Carter, Madison, and Owen. I miss you guys so much. It's always so tough to leave whenever I visit. I would also like to say thanks to my best friend and brother Travis. He was always willing to drive down from the north and help me move or travel together to hang out and relieve some stress. I would also like to say thanks to my brothers, Chris and Scott, and my future sister Jodi.

My journey into chemistry began in the 10th grade. My teacher, Mr. Jeff Wolfe made chemistry interesting to me, this helped me decide to make chemistry my major in college at the University of Scranton. At the end of my junior year I met a very intelligent and interesting consultant at Acton Technologies, Dr. AJ Attar. He took my good friend Joe Labukas and I under his wing and taught us and encouraged us both to continue into graduate school. Many thanks for your encouragement Dr. Attar.

I will be forever indebted to my pair of advisors, Jan Genzer and Chris Gorman for their insight, encouragement and patience in guiding me through the PhD gauntlet. Dr. Gorman was my chemistry advisor who pushed me to work hard and do my very best. Dr.

Genzer allowed me to work and feel like a part of the chemical engineering department. He was always willing to talk about anything and made me feel at ease with his humor no matter the situation. I would also like to thank my other committee members, Dr. Ken Hanck and Dr. Ed Bowden. I would also like to thank Dr. Lin He for allowing me the use of her MALDI-MS.

I had many friends from both the north and the south. I would like to say thanks to you all. I would also like to thank my colleagues from chemistry and chemical engineering, Mike Tomlinson, Kirill Effimenko, Jim Semler, Tao Wu, and Julie Crowe from chemical engineering and Ryan Furier, Szymon Dembowy, Drew Wassel, and Chris Monceaux from chemistry.

Lastly and most importantly I want to thank my love Shannon. She had to deal the daily stress of me during the most critical time of the PhD process. Thank you so much for putting up with my daily complaining and taking care of me while I was writing up this work. I love you so much and look forward to our future together.

TABLE OF CONTENTS

	PAGE
List of Tables	ix
List of Figures	x
1. General Introduction and Project Goals	1
1.1 Matrix Assisted Laser Desorption Ionization (MALDI) of Synthetic Polymers	1
1.1.1 General mechanism for matrix assisted laser desorption ionization..	2
1.1.2 Organic matrix selection for MALDI	3
1.2 Porous Silicon: Formation and surface modification	5
1.2.1 Mechanism for porous silicon formation	6
1.2.2 Desorption ionization on silicon (DIOS)	7
1.2.3 Surface modifications for porous silicon: Improvements in DIOS sensitivity	8
1.2.4 Alternatives substrates investigated for DIOS	10
1.3 Surface Atom Transfer Radical Polymerization (ATRP)	12
1.3.1 Mechanism of ATRP	13
1.4 Self Assembled Monolayers (SAMs): Initiator Systems for Surface Polymerization	14
1.5 References	16
2. Surface-Based Polymerization in Porous Silicon	20
2.1 Project Goals and Motivation	20
2.2 Polymer brushes prepared via ATRP	21
2.2.1 Polymer brushes prepared via “grafting from” <i>versus</i> “grafting to” ..	21
2.2.2 Initiator systems	22
2.2.3 Optimization of initiator deposition conditions	23
2.2.3 Aqueous based ATRP	25
2.3 Polymer Growth in Porous Silicon: Characterization via Infrared Spectroscopy (IR)	25
2.4 Mass Spectrometry of Absorbed Polymers	27
2.4.1 MALDI analysis of absorbed polymers	28
2.4.2 DIOS analysis of absorbed polymers	31

2.4.3	Molecular weight analysis and model fits of MALDI and DIOS Spectra.....	34
2.5	Desorption/ Ionization on Silicon (DIOS): Grown Polymers.....	42
2.5.1	Scanning electron microscopy image of porous silicon.....	43
2.5.2	DIOS on grown PMMA.....	44
2.5.3	Reactive ion etched (RIE) porous silicon.....	46
2.6	Conclusions.....	49
2.7	Experimental.....	51
2.8	References.....	56
3.	Surface-Based Polymerization in Anodic Aluminum Oxide.....	58
3.1	Motivation.....	58
3.2	Polymer Growth in Anodic Aluminum Oxide: Characterization via Infrared Spectroscopy (IR).....	59
3.3	Anodic Aluminum Oxide – Grown Polymers.....	61
3.3.1	PMMA cleavage from AAO.....	61
3.3.2	MALDI spectra of cleaved PMMA.....	63
3.3.3	End group determination of AAO-grown PMMA.....	68
3.3.4	Molecular weight analysis and model fits of MALDI spectra.....	71
3.3.5	Gel Permeation Chromatography (GPC) of AAO-grown PMMA....	83
3.4	Conclusions.....	88
3.5	Experimental.....	89
3.6	References.....	93
4.	Fast Directed Motion of “Fakir” Droplets.....	96
4.1	Introduction.....	96
4.2	Results and Discussion.....	99
4.2.1	Characterization of semifluorinated wettability gradient.....	99
4.2.2	Contact angle hysteresis.....	101
4.2.3	Velocities of drops moving on flat and porous substrates decorated with semifluorinated wettability gradients.....	103
4.3	Conclusions	105

4.4	Experimental.....	107
4.5	References.....	109
5.	Outlook.....	112
5.1	SEM study of porous silicon.....	112
5.2	Systematic study of pore size in anodic aluminum oxide (AAO).....	113
5.3	Replacement of porous silicon with AAO for water motion on wettability gradients.....	114
A1	Appendix 1 – Schultz and “Point-by-Point” distribution fits.....	115
A2	Appendix 2 – MALDI characterization of various dendrimers.....	117

LIST OF TABLES	PAGE
Table 1.1 Table 1.1- General guidelines for the selection of a matrix for polymer analysis in MALDI.....	4
Table 2.1 Description of the deposition conditions used in the NEXAFS experiments.....	25
Table 2.2 Weight average molecular weight (M_w), number average molecular weight (M_n), and polydispersity index (PDI) values for poly(methyl methacrylate) standards.....	41
Table 2.3 Chart showing breakdown of pore diameter, period, and the distance between pores for the different areas within the reactive ion etched silicon.....	48
Table 3.1 Weight average molecular weight, number average molecular weight, and polydispersity values for grown poly(methyl methacrylate).....	78
Table 3.2 The table shows the number average molecular weight for solution grown poly(methyl methacrylate) (PMMA).....	86

LIST OF FIGURES	PAGE
Figure 1.1. Simplified schematic showing matrix assisted laser desorption ionization (MALDI).....	2
Figure 1.2. Scanning electron microscopy (SEM) images of different porous silicon morphologies.....	5
Figure 1.3. Surface-bound oxidation scheme for the formation of SiH _x	6
Figure 1.4. (Pentafluorophenyl)propyldimethylchlorosilane (PFPPDCS) (left) and (3-Aminopropyl)dimethylethoxysilane) (APDMES) (right) were attached to the oxidized surface of porous silicon. The attachment of PFPPDCS has been shown to in crease the sensitivity of DIOS for small analytes that are hydrophobic as well as hydrophillic. The attachment of APDMES was shown to in crease the sensitivity of DIOS for small analytes that are only hydrophillic.....	9
Figure 1.5 Proposed mechanism for alkene addition to hydride terminated silicon..	10
Figure 1.6 Illustration of performing Atom Transfer Radical Polymerization (ATRP) by growing the polymer in solution and then attaching the chain to the surface (grafting onto) The left side shows growing the polymer from a substrate anchored initiator. (grafting from).....	12
Figure 2.1 Two-step surface synthesis of polymerization initiator.....	22
Figure 2.2 One step surface synthesis of [11-(2-Bromo-2-methyl)propionyloxy) undecyltrichlorosilane.....	23
Figure.2.3 Normalized carbon edge data for various monolayer deposition temperatures and times (cf. Table 1). The data have been shifted vertically for clarity APTES/PO mixture for 5 minutes. The area around the PEY NEXAFS line denotes the measurement uncertainty (based on 9 line scans along the gradient taken between -3 mm and +3 mm from the center).....	24
Figure 2.4 IR of BiB deposition, PMMA growth, HF vapor etch, and PMMA extraction.....	26
Figure 2.5 MALDI spectra of four poly(methyl methacrylate) standards with nominal molecular weights of 1.8, 3.25, 6.4, and 6.6 kDa, respectively. The spectra are presented (top left to bottom right) according to the number average molecular weight provided by the manufacturer.....	29

Figure 2.6	MALDI spectra of two poly(methyl methacrylate) standards with nominal molecular weights of (left) 12.3 and (right) 22.2 kDa. The repeat unit of one hundred is no longer visible when going from the top spectrum to the bottom spectrum. The signal-to-noise is also significantly decreased.....	30
Figure 2.7	DIOS spectra of four poly(methyl methacrylate) standards with nominal molecular weights of 1.8, 3.25, 6.4, and 6.6 kDa, respectively. The spectra are presented (top left to bottom right) according to the number average molecular weight provided by the manufacturer.....	33
Figure 2.8	MALDI and DIOS spectra comparison of the Schultz distribution and point by point fit of Poly(methyl methacrylate) standards with nominal molecular weight of 1.8 kDa (information given by manufacturer collected via GPC). The black squares (■) in the top spectrum and the green circles (●) in the bottom spectrum indicate the local maxima for each monomer unit. The line indicating the Schultz distribution fit is shown as a red line (□) in for the MALDI spectra and as a blue line (□) for the DIOS spectra.....	35
Figure 2.9	MALDI and DIOS spectra comparison of the Schultz distribution and point by point fit of Poly(methyl methacrylate) standards with nominal molecular weight of 3.25 kDa (information given by manufacturer collected via GPC). The black squares (■) in the top spectrum and the green circles (●) in the bottom spectrum indicate the local maxima for each monomer unit. The line indicating the Schultz distribution fit is shown as a red line (□) in for the MALDI spectra and as a blue line (□) for the DIOS spectra.....	36
Figure 2.10	MALDI and DIOS spectra comparison of the Schultz distribution and point by point fit of Poly(methyl methacrylate) standards with nominal molecular weight of 6.4 kDa (information given by manufacturer collected via GPC). The black squares (■) in the top spectrum and the green circles (●) in the bottom spectrum indicate the local maxima for each monomer unit. The line indicating the Schultz distribution fit is shown as a red line (□) in for the MALDI spectra and as a blue line (□) for the DIOS spectra.....	37

Figure 2.11 MALDI and DIOS spectra comparison of the Schultz distribution and point by point fit of Poly(methyl methacrylate) standards with nominal molecular weight of 6.6 kDa (information given by manufacturer collected via GPC). The black squares (■) in the top spectrum and the green circles (●) in the bottom spectrum indicate the local maxima for each monomer unit. The line indicating the Schultz distribution fit is shown as a red line (□) in for the MALDI spectra and as a blue line (□) for the DIOS spectra.....	38
Figure 2.12 MALDI spectra collected from Poly(methyl methacrylate) standards with nominal molecular weight of 12.3 and 22.2 kDa. The black squares (■) indicate the local maxima for each monomer unit with respect to the 12.2 kDa graph. The black squares (■) indicate all data points for the 22.2 kDa graph. The signal to noise was insufficient to determine local maxima. The Schultz distribution fit is shown as a red line (□) for each MALDI spectra.....	39
Figure 2.13 Weight average molecular weight (M_w), number average molecular weight (M_n), and polydispersity index (PDI) values for poly(methyl methacrylate) standards. The manufacturer information is listed first, followed by the values obtained via conventional MALDI (Schultz distribution fit followed by point-by-point fit), and lastly the values obtained using the MS-DIOS technique (Schultz distribution fit followed by point-by-point fit). The manufacturers information was determined with Gel Permeation Chromatography (GPC). A MS-DIOS signal could not be obtained for the 12.3 and 22.2 kDa PMMA standards. The red bar (■) indicates number average molecular weight (M_n). The black bar (■) indicates polydispersity (PDI).....	40
Figure 2.14 SEM image of porous silicon cross-section. The porous silicon has been sputter coated with gold to increase image resolution.....	44
Figure 2.15 DIOS Spectra of Grown (3 hours) PMMA in Porous Silicon.....	45
Figure 2.16 SEM image of Reactive Ion Etched Silicon. Courtesy of Nancy Finkel (NCSU, Chemistry).....	47
Figure 2.17 DIOS spectra of RIE silicon. No signal from grown polymer is visible..	49
Figure 3.1 Scanning electron microscopy image of Anodic Aluminum Oxide. Image courtesy of Whatman Corporation.....	59
Figure 3.2 IR of BiB deposition, PMMA growth, PMMA standard on silica, and cleaved PMMA.....	61

Figure 3.3	Zoomed in MALDI spectra of a poly methyl methacrylate sample grown for 30 minutes and cleaved from the AAO with concentrated HF. The repeat unit of the HF-modified polymer is approximately 75 Da.....	62
Figure 3.4	MALDI spectra of two poly methyl methacrylate samples grown for 30 minutes. The left spectrum corresponds to PMMA grown in solution. The right spectrum corresponds to PMMA grown in the pores of an AAO membrane. The inset in the right spectra shows the repeat unit of 100 Da.....	64
Figure 3.5	MALDI spectra of two poly methyl methacrylate samples grown for 60 minutes. The top spectrum corresponds to PMMA grown in solution. The bottom spectrum corresponds to PMMA grown in the pores of an AAO membrane.....	65
Figure 3.6	MALDI spectra of two poly methyl methacrylate samples grown for 90 minutes. The top spectrum corresponds to PMMA grown in solution. The bottom spectrum corresponds to PMMA grown in the pores of an AAO membrane.....	66
Figure 3.7	MALDI spectra of two poly(methyl methacrylate) samples grown for 130 minutes. The top spectrum corresponds to PMMA grown in solution. The bottom spectrum corresponds to PMMA grown in the pores of an AAO membrane.....	67
Figure 3.8	(Left) Schematic showing the surface initiator plus MMA monomer attached to the AAO membrane. The black arrows denote the site at which bond cleavage takes place. (Right) Zoomed-in MALDI spectra of 30 min AAO polymerization. Each monomer unit is separated by 100 Da and has and end with the number “84”.....	70
Figure 3.9	Schematic showing the surface initiator plus MMA monomer attached to the AAO membrane. The black arrows denote the site at which bond cleavage takes place. (Right) Zoomed-in MALDI spectra of 30 min AAO polymerization. Each monomer unit is separated by 100 Da and has and end with the number “00”.....	70
Figure 3.10	Schematic showing the surface initiator plus MMA monomer attached to the AAO membrane. The black arrow denotes the site at which bond cleavage takes place.....	71
Figure 3.11	Comparison of solution and pore grown (30min) poly(methyl methacrylate). The data is fit using a Schultz distribution and a point-by-point fit. The top plot shows the solution polymerization, while and the two AAO-grown distribution plots are shown in the plot split to the	

bottom. The black squares (■) in the top spectrum and the green circles (●) and blue triangles (▲) in the bottom spectrum indicate the local maxima for each monomer unit. The line indicating the Schultz distribution fit is shown as a red line (□) in for the solution polymerization, as a blue line (□) for the first AAO-polymerization distribution, and as a purple line (□) for the second AAO-polymerization distribution.....

73

Figure 3.12 Comparison of solution and pore grown (60min) poly(methyl methacrylate). The data is fit using a Schultz distribution and a point-by-point fit. The top plot shows the solution polymerization, while and the two AAO-grown distribution plots are shown in the plot split to the bottom. The black squares (■) in the top spectrum and the green circles (●) and blue triangles (▲) in the bottom spectrum indicate the local maxima for each monomer unit. The line indicating the Schultz distribution fit is shown as a red line (□) in for the solution polymerization, as a blue line (□) for the first AAO-polymerization distribution, and as a purple line (□) for the second AAO-polymerization distribution.....

74

Figure 3.13 Comparison of solution and pore grown (90min) poly(methyl methacrylate). The data is fit using a Schultz distribution and a point-by-point fit. The top plot shows the solution polymerization, while and the two AAO- grown distribution plots are shown in the plot split to the bottom. The black squares (■) in the top spectrum and the green circles (●) and blue triangles (▲) in the bottom spectrum indicate the local maxima for each monomer unit. The line indicating the Schultz distribution fit is shown as a red line (□) in for the solution polymerization, as a blue line (□) for the first AAO-polymerization distribution, and as a purple line (□) for the second AAO-polymerization distribution.....

75

Figure 3.14 Comparison of solution and pore grown (130min) poly(methyl methacrylate). The data is fit using a Schultz distribution and a point-by-point fit. The top plot shows the solution polymerization and the AAO- grown distribution plot is shown in the plot split to the bottom. The black squares (■) in the top spectrum and the green circles (●) in the bottom spectrum indicate the local maxima for each monomer unit. The line indicating the Schultz distribution fit is shown as a red line (□) in for the solution polymerization and as a blue line (□) for the first AAO-polymerization.....

76

Figure 3.15 Weight average molecular weight, number average molecular weight, and polydispersity values for grown poly(methyl methacrylate). The solution polymerization information is listed first (Schultz distribution fit followed by point-by-point fit) followed by the values obtained for

both pore distributions (Schultz distribution fit followed by point-by-point fit). Both solution and AAO-grown PMMA was collected via conventional MALDI. The grown PMMA is shown in ascending order (30 (top left), 60 (top right), 90 (bottom left), 130 minutes (bottom right)). The red bar (■) indicates number average molecular weight (M_n). The black bar (■) indicates polydispersity (PDI).....

77

Figure 3.16 The figure plots number average molecular weight (M_n) of solution grown polymer samples with the increasing polymerization time (30, 60, 90, and 130 min). The black square (■) indicates the M_n value as fit by the Schultz distribution model. The red line (□) indicates the linear fit of the Schultz distribution data. The filled green circles (●) indicate the M_n value as fit by the point-by-point analysis of the local maxima of each monomer unit. The blue line (□) indicates the linear fit of the (Pt-by-pt) data.....

79

Figure 3.17 The figure plots number average molecular weight (M_n of surface distribution #1) with increasing polymerization time (30, 60, 90, and 130 min). The black square (■) indicates the M_n value as fit by the Schultz distribution model. The red line (□) indicates the linear fit of the Schultz distribution data. The filled green circles (●) indicate the M_n value as fit by the point-by-point analysis of the local maxima of each monomer unit. The blue line (□) indicates the linear fit of the point-by-point data.....

82

Figure 3.18 The figure plots number average molecular weight (M_n of surface distribution #2) with increasing polymerization time (30, 60, 90, and 130 min). The black square (■) indicates the M_n value as fit by the Schultz distribution model. The red line (□) indicates the linear fit of the Schultz distribution data. The filled green circles (●) indicate the M_n value as fit by the point-by-point analysis of the local maxima of each monomer unit. The blue line (□) indicates the linear fit of the point-by-point data.....

83

Figure 3.19 Sample chromatogram for the 90-minute polymerization of PMMA in solution and in the AAO pores. A chromatogram of a 3.25 kDa PMMA standard is also shown. One peak was observed for the solution-grown PMMA and the PMMA standard. Two peaks were observed for the AAO-grown PMMA. A calibration curve of three PMMA standards was used to convert elution time (the standard x-axis for the chromatograms output) into a log 10 scale of number average molecular weight. The y-axis shows the intensity as collected by the refractive index detector.....

84

Figure 3.20	The figure plots number average molecular weight given by the manufacturer (GPC) with the number average molecular weight found with MALDI. The filled black squares (■) indicate the M_n value of the PMMA standards as fit by the Schultz distribution model. The open black squares (□) indicate the M_n value of the PMMA standards as fit by the point-by-point analysis of the local maxima of each monomer unit. The filled red circles (●) indicate the M_n value of the solution grown PMMA as fit by the Schultz distribution model. The open red circles (○) indicate the M_n value of the solution grown PMMA as fit by the point-by-point analysis of the local maxima of each monomer unit. The red line (—) indicates the linear fit of the Schultz distribution and point-by-point data.....	87
Figure 4.1	(Left) Cross sectional scanning electron microscopy image of porous silicon. The diagram depicts the outline of the porous region after etching. (Right) Relative fluorine concentration on the porous substrate decorated with the gradient in F8H2 self-assembled monolayer as determined from the combinatorial near-edge x-ray absorption fine structure spectroscopy experiments.....	101
Figure 4.2	Advancing (solid symbols) and receding (open symbols) contact angles of deionized water as a function of the position on the F8H2 molecular gradient created on top of a flat (a) and porous (b) silicon substrate. The volume of the probing liquid was 4 (■), 6 (●), 8 (▲), 10 (▼), and 12 (◆) μ l.....	102
Figure 4.3	Capillary number ($Ca=v/v^*$) as a function of the normalized drop radius ($R^*=R \cdot \partial \cos(\theta) / \partial x$) associated with motion of a droplet of deionized water along the F8H2 molecular gradient created on top of a flat (open symbols) and porous (solid symbols) silicon substrate. During the course of the experiment the drop velocity was collected at multiple positions on the sample. The data presented in Figure 3 have been compiled from the drop velocity data collected at the constant contact angle of water equal to: 70° (▽), 65° (△), 60° (M), 100° (■), and 80° (●). The lines are meant to guide the eye.....	104
Figure A2.1	Amphiphilic iron-sulfur core dendrimer (Generation 1).....	118
Figure A2.2	Amphiphilic iron-sulfur core dendrimer (Generation 2).....	119
Figure A2.3	Amphiphilic iron-sulfur core dendrimer (Generation 3).....	119
Figure A2.4	3,5-aromatic iron-sulfur core dendrimer (Generation 2).....	120

Figure A2.5 2,6-aromatic iron-sulfur core dendrimer (Generation 2).....	120
Figure A2.6 Osmium Tris(bipyridine) core dendrimer (Generation 1).....	121
Figure A2.7 Ruthenium Tris(bipyridine) core dendrimer (Generation 1).....	121

Chapter 1: General Introduction and Project Objective

The chief goal of this PhD dissertation is to study the effect of the confinement due to the concave geometry on the polymerization process that is initiated inside small pores. Characterization of the pore-grown polymer is key in understanding this behavior. Thus, the introduction will focus on three major concepts: 1) the use of matrix-assisted laser desorption ionization (MALDI) for the direct characterization of macromolecules, with a specific focus on polymers, 2) the replacement of the conventional organic matrix used in MALDI with porous silicon and, 3) utilizing porous silicon as a substrate for the controlled/living polymerization (via atom transfer radical polymerization (ATRP)) of poly methyl methacrylate. The combination of these three areas allows for the study of polymerization in confined geometries through the use of porous silicon as a platform for mass spectrometry characterization.

1.1 Matrix Assisted Laser Desorption Ionization (MALDI) of Synthetic Polymers

Mass spectrometry of synthetic polymers using the matrix assisted laser desorption ionization (MALDI) technique has become increasingly important as a direct molecular weight characterization of macromolecules. In the late 1980's Karas and Hillenkamp developed the use of an organic matrix (a small organic molecule) to improve upon the 10 kDa limit observed in molecular weight analysis prior to matrix development [1]. The organic matrix developed had a high absorbance at the laser wavelength and was ionizable. The matrix was cocrystallized with a small concentration of the analyte of interest onto a sample plate and a small spot of matrix and analyte was hit with a pulsed laser beam. Ions

ablated from the sample plate were then drawn towards the mass spectrometer via an extraction grid. (Figure 1.1)

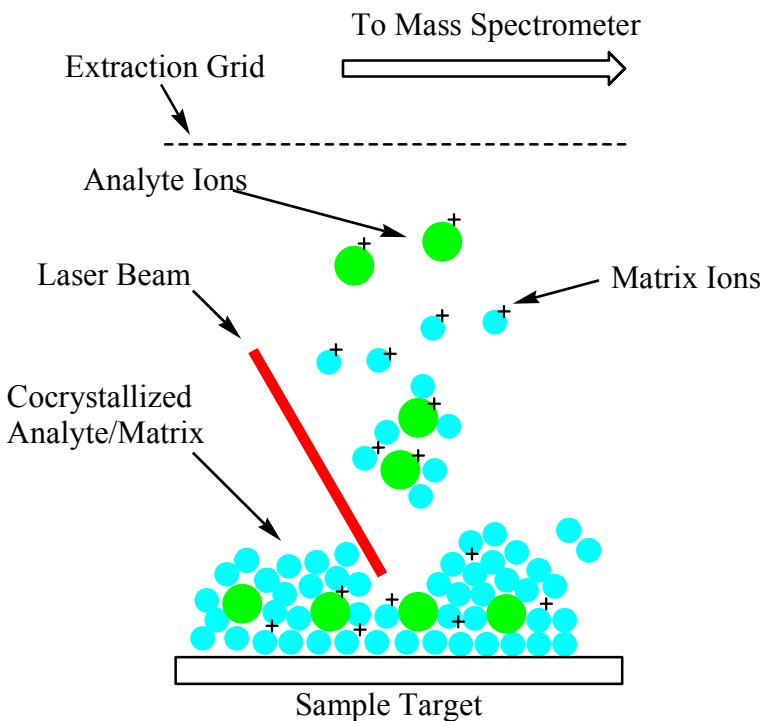


Figure 1.1- Simplified schematic showing matrix assisted laser desorption ionization (MALDI)

1.1.1 General mechanism for matrix assisted laser desorption ionization

The general mechanism of MALDI is believed to consist of three basic steps:

- (1) Formation of cocrystallized matrix and analyte: Excess matrix is utilized to separate the analyte molecules. The separation of the analyte molecules produce desorption of the analyte from the target.
- (2) Laser induced matrix excitation: The laser beam strikes the cocrystallized matrix/analyte and induces rapid vibration of the matrix. The reason for this rapid vibration is the coupling of matrix with the laser frequency. The vibration of the matrix causes breakup of the cocrystallized matrix/analyte.

(3) Analyte ionization: Proton transfer from the matrix to the analyte produces cation attachment. The cation attachment creates the distinctive $[M+\text{cation}]^+$ analyte ions, where the cation can be hydrogen, sodium, potassium etc. Conversely, an anion can also be attached to the analyte. The analyte ions are drawn by the extraction grid into the mass spectrometer [2-7].

Around the same time period of Karas and Hillenkamp's work, Tanaka demonstrated the application of MALDI to a whole range of proteins and biopolymers. Tanaka's work led him to eventually receive a share of the 2002 Nobel Prize for chemistry. Since this time, a large volume of work has been focused on increasing the mass range and the library of molecules characterized [3, 8-17]. The MALDI characterization of synthetic polymers has proven to be particularly difficult.

There are a couple reasons why the analysis of synthetic polymers is difficult. Synthetic polymers possess a molecular weight distribution instead of a single molecular weight, due to the limitations of polymer synthesis. In addition, synthetic polymers are terminated and initiated differently resulting in different end group functionality. In spite of these difficulties, polymers with narrow polydispersities and molecular weights of up to 1.5 MDa have been characterized [18].

1.1.2 Organic matrix selection for MALDI

Homogeneous cocrystallization of analyte and matrix molecules is the goal in the sample preparation for every MALDI experiment. Completely homogenous sample preparations are difficult to attain and so-called "sweet spots" are sought to obtain quality resolution. While much of the work done in the characterization of polymers via MALDI is

made on trial and error, a general trend has been established when searching for the appropriate matrix. Matching the polarity of the matrix with the polymer is the general rule of thumb. Hanton reported on these general guidelines [19]:

Table 1.1- General guidelines for the selection of a matrix for polymer analysis in MALDI. The polymers and matrices are listed from hydrophilic (top) to hydrophobic (bottom).

Matrices	Hydrophilic	Polymer
2,5-Dihydroxybenzoic acid		Polypropylene glycol
α -cyanohydroxycinnamic acid		Polyvinyl acetate
Ferulic acid		Polytetramethylene glycol
Indoleacrylic acid		Polymethylmethacrylate
Dithranol		Polystyrene
All trans-Retinoic acid		Polybutadiene
Diphenylbutadiene	Hydrophobic	Polydimethylsiloxane

While these general guidelines help match a matrix with the polymer under investigation, there are some caveats associated with the organic matrix material. Some matrices (e.g., indoleacrylic acid) self polymerize and block out the mass spectrum up to several thousand of Daltons. In fact, all matrices obscure the lower molecular weight region to some degree. For this reason, a replacement was sought to decrease the amount of background ions created by the matrix. Siuzdak and Buriak developed a matrix free strategy for MALDI based upon a solid porous silicon substrate [20].

1.2 Porous Silicon: Formation and surface modification

The modification of silicon has been and will continue to be a major emphasis of study because of its applications in several branches of science and technology, including electronics, analytical sciences, and optics. A multitude of silicon surface modification methods have been developed. They range from simply changing the end groups at the surface atoms of the silicon to hydroxyl or hydride termination to chemically bonding self assembled monolayers (SAMs) [21-24] to the surface, all the way to growing polymer off the surface of the silicon [25]. The modification of to porous silicon (p-Si) involves a photochemical etch of the silicon wafer to create hydride termination on the end groups of the surface atoms and a very unique porous surface morphology. The different surface morphologies of porous silicon are shown in Figure 1.2.

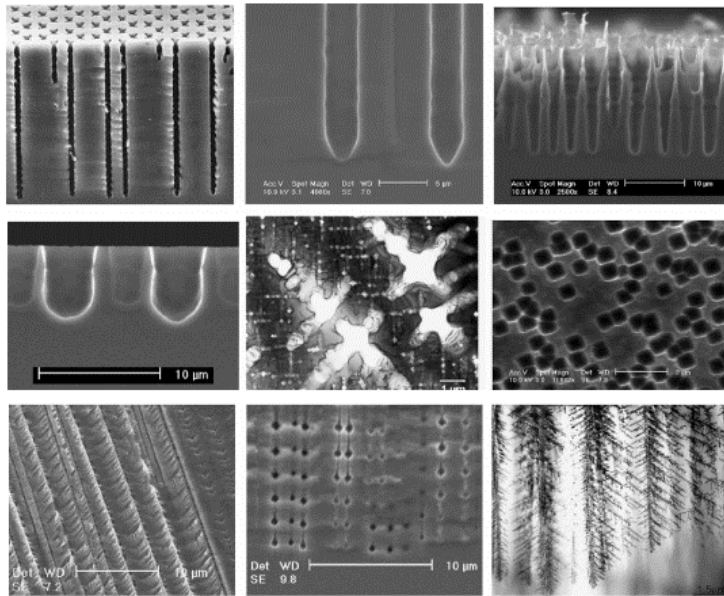


Figure 1.2 - Scanning electron microscopy (SEM) images of different porous silicon morphologies [26].

Modifying the surface chemistry of silicon and the surface morphology has been the focus of a number of different research studies. Although the formation of porous silicon

was reported first by Uhlir in 1956 [27], it has gained a new wave of interest recently due to its room temperature photoluminescence and electro luminescence properties that may find applications in various branches of optoelectronics [28-32]. Porous silicon also has potential applications in microelectronics, LED's, gas sensors, and as silicon solar cells [33-37].

1.2.1 Mechanism for porous silicon formation

The pore diameter, pore diameter distribution, and the morphology of the pores are dependent on the doping level and type of dopant, composition of the etching solution, white light intensity, and the current density [20, 38-40]. While the mechanism of surface modification is not completely understood, certain aspects of the process are known. Holes are required in the initial oxidation for pore formation in n-type silicon. Thus, for n-type silicon, illumination is required for hole formation. Every hole that is generated by white light illumination allows for the dissolution of one whole silicon atom. The proposed surface-bound oxidation scheme, shown in Figure 1.3, illustrates the formation of Si-H and the divalent silicon oxidation state [32].

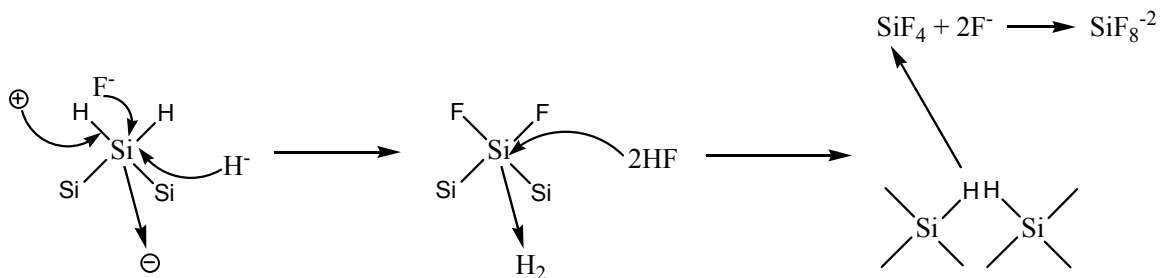


Figure 1.3 – Surface-bound oxidation scheme for the formation of SiH_x

1.2.2 Desorption ionization on silicon (DIOS)

Porous silicon has also gained attention for its use as a matrix-less substrate for Matrix Assisted Laser Desorption/ Ionization (MALDI) mass spectrometric analysis [20]. The traditional form of MALDI allows for the molecular weight analysis of molecules ranging from proteins to polymers. MALDI uses an ultraviolet light-absorbing organic matrix to desorb molecules from a stainless steel target for analysis. The matrix serves as an energy absorber and transfers some of its energy to the analyte being studied. Without this organic matrix, such as trans-cinnamic acid or 2,5-dihydroxybenzoic acid, the analyte would never desorb from the surface and be detected by the instrument. The technique using porous silicon as the matrix is known as Desorption/ Ionization on Silicon Mass Spectrometry (MS-DIOS). MS-DIOS has the advantage of transferring the energy from the laser directly to the analyte instead of first dissolving the analyte in an ultraviolet-absorbing organic acid matrix which is then ablated with the pulsed laser inside the instrument. The current method of MALDI analyses carries the matrix as well as the analyte to the detector that, in turn, saturates the detector with numerous contaminant and matrix ions. The MS-DIOS technique allows for the analyte to be trapped in the pores of the substrate. Thus, once the laser hits the highly UV-absorbing porous silicon, the energy is transferred directly to the analyte that is ablated from the surface and ionized. MS-DIOS is considered to be a direct desorption/ionization technique, in that it does not use a matrix. MS-DIOS is different from most direct techniques because little to no molecular fragmentation and sample contamination occur. While most research has focused mainly on low mass molecules ($M_w < 300$), e.g., such as proteins and enzymes, MS-DIOS has also been applied to larger molecules, e.g., peptides, carbohydrates, and polymers [20, 39, 41, 42].

The work done on these low molecular weight molecules has focused on optimizing the MS-DIOS's signal by tuning the pore size for a particular analyte. The original work reported by Siuzdak utilized microporous (≤ 2 nm pores) and mesoporous (2-50 nm pores) silicon [20]. Siuzdak and coworkers concluded that pores of a smaller size gave the best signal. A determination of "smaller" was not defined. Most molecules investigated in this study had a molecular weight less than 1 kDa with the exception of two moieties. Later work by Sweedler concluded that MS-DIOS spectra could be obtained with pore sizes that ranged from 2-200 nm. Further stating small pores (≈ 10 nm) were more effective in producing reproducible spectra for small analyte molecules but pore size and the overall porosity of the silicon had to be large enough to support a platform for MS-DIOS [39]. Again, this study dealt with molecules that were less than 1 kDa. A comprehensive analysis of pore size and its relationship with reproducible MS-DIOS spectra has been presented.

1.2.3 Surface modifications for porous silicon: Improvements in DIOS sensitivity

Recent advances have been focused on the surface modification of the porous silicon in to improve the sensitivity of the MS-DIOS technique [43]. Specifically, Siuzdak and coworkers have oxidized and then silylated the surface of porous silicon. Different functional groups were used depending on the analyte of interest. For example, the porous silicon was derivatised using (pentafluorophenyl)propyldimethylchlorosilane (PFPPDCS), shown in Figure 1.4, for the analysis of small hydrophobic and hydrophilic molecules. PFPPDCS was effective in increasing the sensitivity of the signal obtained for des-Arg⁹-Bradykinin. MS-DIOS spectra could be collected using porous silicon modified PFPPDCS down to a

concentration of 800 yoctomoles. The PFPPDCS modified DIOS chips showed a lifetime longer than 9 months without a distinct loss of sensitivity. They were also resistant to acid/base hydrolysis, air/oxidation, and showed the lowest number of background ions.

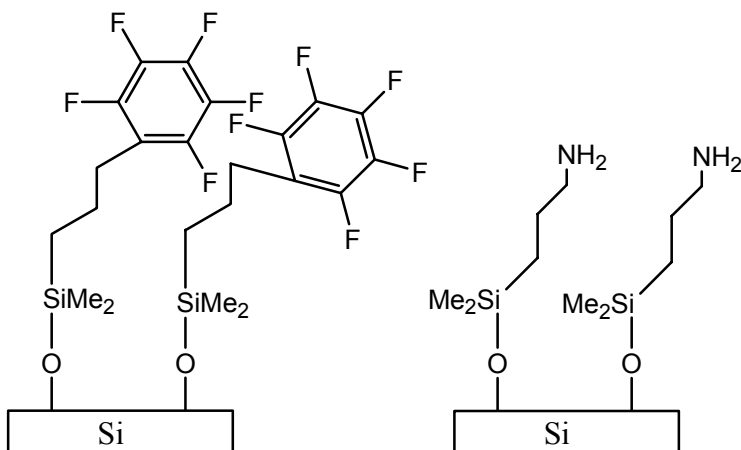


Figure 1.4 - (Pentafluorophenyl)propyldimethylchlorosilane (PFPPDCS) (left) and (3-Aminopropyl)dimethylethoxysilane (APDMES) (right) were attached to the oxidized surface of porous silicon. The attachment of PFPPDCS has been shown to increase the sensitivity of DIOS for small analytes that are hydrophobic as well as hydrophilic. The attachment of APDMES was shown to increase the sensitivity of DIOS for small analytes that are only hydrophilic.

The end group present at the surface of porous silicon allows for further modification of this substrate. For example, surface passivation of the porous silicon stabilizes the substrate against oxidation (a process that will occur within hours in air) and adsorption of contaminants from the air. This ‘degradation’ of p-Si causes the loss of its photoluminescence. Several methods of silicon surface functionalization are known. A notable method involves hydrosilation of an alkene or alkyne at a hydride-terminated silicon surface [23, 44, 45]. The mechanism used to create Si-C bond formation involved the nucleophilic attack of a surface localized positive charge, the hole created by illumination during photochemical etching, by an alkene or an alkyne. The Buriak group has focused on

the direct chemical modification of porous silicon by means of functionalized alkenes or alkynes. Figure 1.5 represents Buriak's proposed mechanism.

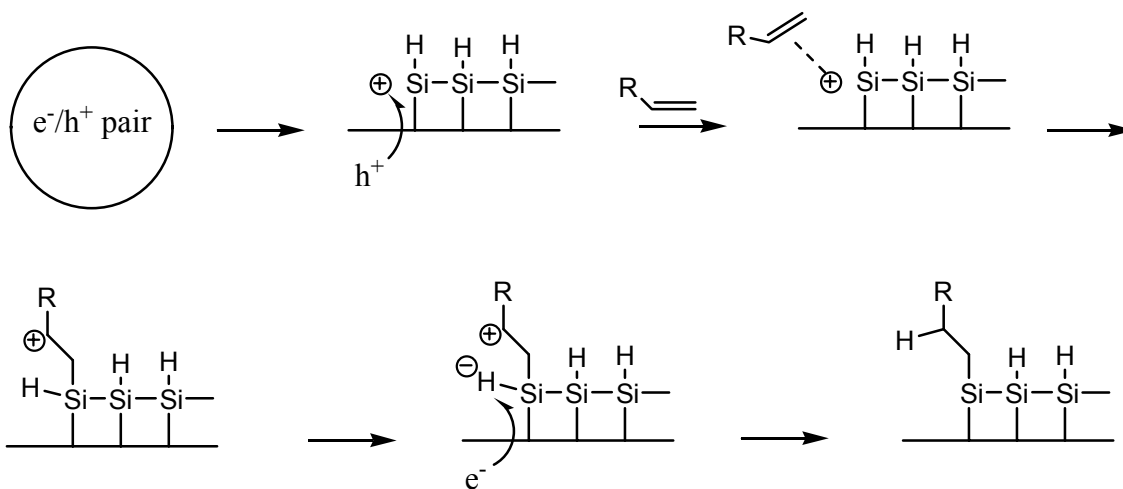


Figure 1.5 – Proposed mechanism for alkene addition to hydride terminated silicon

The hydrosilylation reaction allows for a broad range of chemical groups to be attached to the surface of the material without removing the properties that make porous silicon so unique such as its high surface area, porosity, and visible room temperature photoluminescence [23, 44, 45]. Other attachment chemistries have investigated utilizing hydrosilylation chemistry to form the Si-C bond. An organic linker was then applied to covalently attach biomolecules, such as proteins and enzymes [46]. Modifications to porous silicon have been the focus of improving the DIOS signal but different materials have also been studied.

1.2.4 Alternatives substrates investigated for DIOS

Several other surfaces have been studied as possible platforms for desorption/ionization. Specifically, p-GaAs and p-GaN has been investigated by Sweedler,

who reported that these matrices provide no analyte signal. These surfaces were prepared to give a surface morphology similar to that of p-Si. One parameter that is important in determining whether the substrate would be a good desorption/ionization platform is optical absorption. Because the optical absorption of p-GaAs and p-GaN is smaller than that of p-Si, energy from the laser would be absorbed at a shorter depth and possibly not transferred to the analyte as efficiently. p-Si is the only substrate known to date that combines a high surface area, large absorption at the wavelength of the laser, and the thermal conductivity needed to transfer the absorbed energy from the laser to the analyte to produce quality mass spectra over a wide range of molecules [39].

The properties of porous silicon can also be tailored using surface attached polymers. The ability to polymerize in the porous silicon substrate, which acts as a matrix, allows for the direct analysis of a surface grown polymer through MALDI characterization. The strategy also allows the study of the effect of the confinement of the polymerization process due to the concave geometry of the porous silicon. Changing polymerization time could vary the molecular weight of these polymers. Changing the pore size of the porous silicon would also affect the polymer by 1.) possibly changing the rate of polymerization and 2.) tuning the MS-DIOS signal for maximum ablation of the pore grown polymer. Control and characterization of these parameters would be vital in understanding how these surface modifications affect the properties of porous silicon as well as how the porous silicon affects the growth of the polymer [47].

1.3 Surface Atom Transfer Radical Polymerization (ATRP)

The focus of this work is on chemically bonding polymer brushes to a solid substrate using Atom Transfer Radical Polymerization (ATRP). The two ways of chemically bonding a polymer to a surface involve the “grafting from” and the “grafting onto” approaches. The “grafting onto” method utilizes formation of surface-anchored polymer by adsorbing the chains from solution onto the substrate. The “grafting from” method uses a substrate covered with chemisorbed initiator molecules to grow the polymer directly off the surface. The “grafting onto” method yields a low grafting density due to the high entropy associated with packing the chains on the surface. The “grafting from” method is preferred due to the ability to produce highly packed polymer brushes. Figure 1.6 illustrates the two ways of surface anchoring a polymer brush to a substrate.

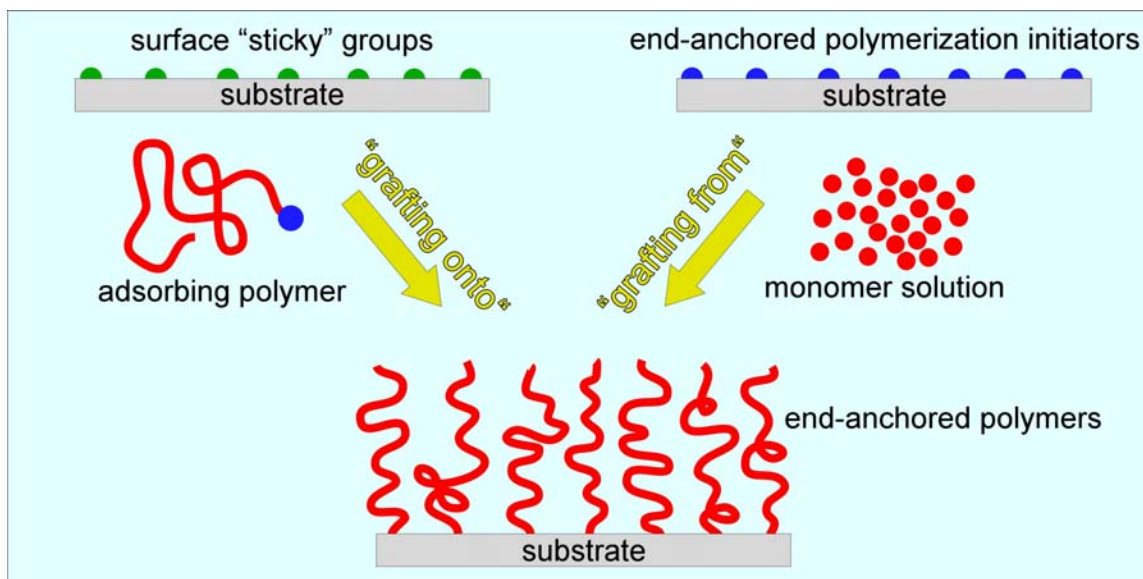
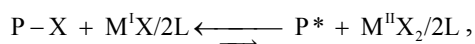


Figure 1.6: Illustration of performing Atom Transfer Radical Polymerization (ATRP) by growing the polymer in solution and then attaching the chain to the surface (grafting onto) The left side shows growing the polymer from a substrate anchored initiator. (grafting from)

1.3.1 Mechanism of ATRP

ATRP is a fairly new polymerization technique based on controlled/"living" radical process. Since its conception in 1995, ATRP has become a routine polymerization technique because of its robustness, the ability to form polymers with fairly narrow molecular weight distributions ($M_w/M_n < 1.5$), and ability to form polymers of various architectures and compositions [48-50].

The key reaction in ATRP is the reversible activation-deactivation process using metal (M)/ligand (L) complexes [51]:



where M is usually Cu, and X is Cl or Br. The propagating radical, P^* , produced by the halogen atom transfer from P-X to the $M^I X/2L$ complex, will undergo polymerization until it is deactivated by the $M^{II} X_2/2L$ complex. MCl_2 is usually added to the reaction mixture to regulate the reaction rate and chain polydispersity. The quick speed of the activation-deactivation cycles compared to rate of polymerization leads to a low concentration of the active radicals (relative to the P-X ones). The quick exchange of the halogen from the activator deactivator complex leads to polymers with narrow polydispersities [25].

A large library of polymers have been synthesized via ATRP including acrylamides, acrylonitrile, styrenes, methacrylates, acrylates, and vinylpyridine [48-50, 52]. Recently, Armes et al. and others have shown that ATRP can be simplified even further by synthesizing some polymers at room temperature using a water/solvent system. These

reactions have high polymerization rates and can be performed at room temperature. This new form of ATRP in an aqueous medium is ideal for fast polymerization and its mild reaction conditions [47, 53-55]. The increased polarity of H₂O/MeOH system over organic solvents serves to solubilize the catalyst system more efficiently. This leads to a more active catalyst and increases the rate of polymerization.

1.4 Self Assembled Monolayers (SAMs): Initiator Systems for Surface Polymerization

SAM's on gold and silicon have been studied extensively for their ability to tune the physico-chemical characteristics of surfaces, including, the surface energy, and the electrochemical activity. Alkoxy and chlorosilanes react with the hydroxyl-terminus silicon dioxide present to form SAMs whereas thiols will react with a gold substrate to form well-ordered SAMs. A library of functional groups has been studied for attachment to the surface of silicon. For the purposes of radical initiation, the end group functionalization needs to be an alkyl halide, with the tertiary alkyl halide being more efficient than the secondary or primary alkyl halides for ATRP polymerization. Haloesters, haloketones, and sulfonyl halides can also be used as radical initiating species. While bromide or chloride-based initiators have been shown to provide the best control over the molecular weight distributions, alkyl iodides have also been shown to work well for some specific cases such as acrylate and some modified styrene polymerizations. For the purpose of stabilizing the halogen exchange, the most stable electron donor groups are as follows:-: CN > C(O)R > C(O)OR > Ph > Cl > Me. Combining an efficient initiator with ATRP allows for a variety of very distinct surfaces to be created on silicon surfaces [56-59].

The “grafting from” ATRP approach combined with DIOS could offer a way to directly characterize the molecular weight of a surface grown polymer. Current efforts focus on measuring the thickness of the polymer grown in solution under the same conditions as the surface grown polymer [25]. Wirth and co-workers have investigated growing polyacrylamide on silica spheres, cleaving off the polymer and analyzing the polymer via size exclusion chromatography [58]. The work described in the next chapter involves growing polymer in the porous silicon substrate, which acts as a matrix and allows for the direct analysis of a surface grown polymer through MALDI characterization. The strategy also allows the study of the effect of the confinement due to the concave geometry of the porous silicon on the polymerization process.

1.5 References

1. Karas, M. and F. Hillenkamp, *Laser Desorption Ionization of Proteins with Molecular Masses Exceeding 10000 Daltons*. Analytical Chemistry, 1988. **60**(20): p. 2299-2301.
2. Karas, M., D. Bachmann, and F. Hillenkamp, *Influence of the Wavelength in High-Irradiance Ultraviolet-Laser Desorption Mass-Spectrometry of Organic-Molecules*. Analytical Chemistry, 1985. **57**(14): p. 2935-2939.
3. Karas, M., et al., *Matrix-Assisted Ultraviolet-Laser Desorption of Nonvolatile Compounds*. International Journal of Mass Spectrometry and Ion Processes, 1987. **78**: p. 53-68.
4. Hillenkamp, F., et al., *Matrix-Assisted Laser Desorption Ionization Mass-Spectrometry of Biopolymers*. Analytical Chemistry, 1991. **63**(24): p. A1193-A1202.
5. Ehring, H., M. Karas, and F. Hillenkamp, *Role of Photoionization and Photochemistry in Ionization Processes of Organic-Molecules and Relevance for Matrix-Assisted Laser Desorption Ionization Mass-Spectrometry*. Organic Mass Spectrometry, 1992. **27**(4): p. 472-480.
6. Beavis, R.C., *Matrix-Assisted Ultraviolet-Laser Desorption - Evolution and Principles*. Organic Mass Spectrometry, 1992. **27**(6): p. 653-659.
7. Gluckmann, M., et al., *Mechanisms in MALDI analysis: surface interaction or incorporation of analytes?* International Journal of Mass Spectrometry, 2001. **210**(1-3): p. 121-132.
8. Brown, R.S. and J.J. Lennon, *Mass Resolution Improvement by Incorporation of Pulsed Ion Extraction in a Matrix-Assisted Laser-Desorption Ionization Linear Time-of-Flight Mass-Spectrometer*. Analytical Chemistry, 1995. **67**(13): p. 1998-2003.
9. Bednarek, M., T. Biedron, and P. Kubisa, *Studies of atom transfer radical polymerization (ATRP) of acrylates by MALDI TOF mass spectrometry*. Macromolecular Chemistry and Physics, 2000. **201**(1): p. 58-66.
10. Compton, B.J. and G. Siuzdak, *Mass spectrometry in nucleic acid, carbohydrate and steroid analysis*. Spectroscopy-an International Journal, 2003. **17**(4): p. 699-713.
11. Cottrell, J.S., M. Koerner, and R. Gerhards, *The characterization of synthetic polymers by matrix-assisted laser desorption/ionization mass spectrometry*. Rapid Communications in Mass Spectrometry, 1995. **9**(15): p. 1562-1564.
12. Knochenmuss, R., E. Lehmann, and R. Zenobi, *Polymer cationization in matrix-assisted laser desorption/ionization*. European Mass Spectrometry, 1998. **4**(6): p. 421-426.
13. Koster, S., et al., *Endgroup determination of synthetic polymers by electrospray ionization Fourier transform ion cyclotron resonance mass spectrometry*. Journal of the American Society for Mass Spectrometry, 2000. **11**(6): p. 536-543.
14. Meier, M.A.R. and U.S. Schubert, *Evaluation of a new multiple-layer spotting technique for matrix-assisted laser desorption/ionization time-of-flight mass spectrometry of synthetic polymers*. Rapid Communications in Mass Spectrometry, 2003. **17**(7): p. 713-716.
15. Montaudo, G., et al., *Characterization of Polymers by Matrix-Assisted Laser-Desorption Ionization Time-of-Flight Mass-Spectrometry - Molecular-Weight*

- Estimates in Samples of Varying Polydispersity*. Rapid Communications in Mass Spectrometry, 1995. **9**(5): p. 453-460.
16. Wu, K.J. and R.W. Odom, *Characterizing synthetic polymers by MALDI MS*. Analytical Chemistry, 1998. **70**(13): p. 456A-461A.
 17. Yalcin, T., Y.Q. Dai, and L. Li, *Matrix-assisted laser desorption/ionization time-of-flight mass spectrometry for polymer analysis: Solvent effect in sample preparation*. Journal of the American Society for Mass Spectrometry, 1998. **9**(12): p. 1303-1310.
 18. Schriemer, D.C. and L. Li, *Detection of high molecular weight narrow polydisperse polymers up to 1.5 million Daltons by MALDI mass spectrometry*. Analytical Chemistry, 1996. **68**(17): p. 2721-2725.
 19. Hanton, S.D., P.A.C. Clark, and K.G. Owens, *Investigations of matrix-assisted laser desorption/ionization sample preparation by time-of-flight secondary ion mass spectrometry*. Journal of the American Society for Mass Spectrometry, 1999. **10**(2): p. 104-111.
 20. Wei, J., J.M. Buriak, and G. Siuzdak, *Desorption-ionization mass spectrometry on porous silicon*. Nature, 1999. **399**(6733): p. 243-246.
 21. Anderson, R.C., R.S. Muller, and C.W. Tobias, *Chemical Surface Modification of Porous Silicon*. Journal of the Electrochemical Society, 1993. **140**(5): p. 1393-1396.
 22. Barness, Y., et al., *Functionalized silanes for the preparation of siloxane-anchored monolayers*. Langmuir, 2000. **16**(1): p. 247-251.
 23. Buriak, J.M. and M.J. Allen, *Lewis acid mediated functionalization of porous silicon with substituted alkenes and alkynes*. Journal of the American Chemical Society, 1998. **120**(6): p. 1339-1340.
 24. Fadeev, A.Y. and T.J. McCarthy, *Self-assembly is not the only reaction possible between alkyltrichlorosilanes and surfaces: Monomolecular and oligomeric covalently attached layers of dichloro- and trichloroalkylsilanes on silicon*. Langmuir, 2000. **16**(18): p. 7268-7274.
 25. Ejaz, M., et al., *Controlled graft polymerization of methyl methacrylate on silicon substrate by the combined use of the Langmuir-Blodgett and atom transfer radical polymerization techniques*. Macromolecules, 1998. **31**(17): p. 5934-5936.
 26. Foll, H., et al., *Formation and application of porous silicon*. Materials Science & Engineering R-Reports, 2002. **39**(4): p. 93-141.
 27. Uhler, A., *Electrolytic Shaping of Germanium and Silicon*. Bell System Technical Journal, 1956. **35**(2): p. 333-347.
 28. Cullis, A.G., L.T. Canham, and P.D.J. Calcott, *The structural and luminescence properties of porous silicon*. Journal of Applied Physics, 1997. **82**(3): p. 909-965.
 29. Zangoie, S., R. Jansson, and H. Arwin, *Microstructural control of porous silicon by electrochemical etching in mixed HCl/HF solutions*. Applied Surface Science, 1998. **136**(1-2): p. 123-130.
 30. Canham, L.T., *Silicon Quantum Wire Array Fabrication by Electrochemical and Chemical Dissolution of Wafers*. Applied Physics Letters, 1990. **57**(10): p. 1046-1048.
 31. Halimaoui, A., et al., *Electroluminescence in the Visible Range During Anodic-Oxidation of Porous Silicon Films*. Applied Physics Letters, 1991. **59**(3): p. 304-306.
 32. Smith, R.L. and S.D. Collins, *Porous Silicon Formation Mechanisms*. Journal of Applied Physics, 1992. **71**(8): p. R1-R22.

33. Balucani, M., S. La Monica, and A. Ferrari, *200 MHz optical signal modulation from a porous silicon light emitting device*. Applied Physics Letters, 1998. **72**(6): p. 639-640.
34. Hirschman, K.D., et al., *Silicon-based visible light-emitting devices integrated into microelectronic circuits*. Nature, 1996. **384**(6607): p. 338-341.
35. Vitanov, P., et al., *Structure and morphological studies of thin porous silicon layers*. Vacuum, 2000. **58**(2-3): p. 351-357.
36. Martin-Palma, R.J., et al., *Morphological, optical and electrical characterization of antireflective porous silicon coatings for solar cells*. Optical Materials, 2001. **17**(1-2): p. 75-78.
37. Yerokhov, V.Y., et al., *Cost-effective methods of texturing for silicon solar cells*. Solar Energy Materials and Solar Cells, 2002. **72**(1-4): p. 291-298.
38. Janshoff, A., et al., *Macroporous p-type silicon Fabry-Perot layers. Fabrication, characterization, and applications in biosensing*. Journal of the American Chemical Society, 1998. **120**(46): p. 12108-12116.
39. Kruse, R.A., et al., *Experimental factors controlling analyte ion generation in laser desorption/ionization mass spectrometry on porous silicon*. Analytical Chemistry, 2001. **73**(15): p. 3639-3645.
40. Lehmann, V. and H. Foll, *Formation Mechanism and Properties of Electrochemically Etched Trenches in N-Type Silicon*. Journal of the Electrochemical Society, 1990. **137**(2): p. 653-659.
41. Shen, Z.X., et al., *Porous silicon as a versatile platform for laser desorption/ionization mass spectrometry*. Analytical Chemistry, 2001. **73**(3): p. 612-619.
42. Thomas, J.J., et al., *Desorption-ionization on silicon mass spectrometry: an application in forensics*. Analytica Chimica Acta, 2001. **442**(2): p. 183-190.
43. Trauger, S.A., et al., *High sensitivity and analyte capture with desorption/ionization mass spectrometry on silylated porous silicon*. Analytical Chemistry, 2004. **76**(15): p. 4484-4489.
44. Buriak, J.M., *Organometallic chemistry on silicon surfaces: formation of functional monolayers bound through Si-C bonds*. Chemical Communications, 1999(12): p. 1051-1060.
45. Schmeltzer, J.M., et al., *Hydride abstraction initiated hydrosilylation of terminal alkenes and alkynes on porous silicon*. Langmuir, 2002. **18**(8): p. 2971-2974.
46. Hart, B.R., et al., *New method for attachment of biomolecules to porous silicon*. Chemical Communications, 2003(3): p. 322-323.
47. Robinson, K.L., et al., *Controlled polymerization of 2-hydroxyethyl methacrylate by ATRP at ambient temperature*. Macromolecules, 2001. **34**(10): p. 3155-3158.
48. Matyjaszewski, K. and J.H. Xia, *Atom transfer radical polymerization*. Chemical Reviews, 2001. **101**(9): p. 2921-2990.
49. Matyjaszewski, K., et al., *Polymers at interfaces: Using atom transfer radical polymerization in the controlled growth of homopolymers and block copolymers from silicon surfaces in the absence of untethered sacrificial initiator*. Macromolecules, 1999. **32**(26): p. 8716-8724.

50. Matyjaszewski, K., T.E. Patten, and J.H. Xia, *Controlled/"living" radical polymerization. Kinetics of the homogeneous atom transfer radical polymerization of styrene*. Journal of the American Chemical Society, 1997. **119**(4): p. 674-680.
51. Wang, J.S. and K. Matyjaszewski, *Controlled Living Radical Polymerization - Atom-Transfer Radical Polymerization in the Presence of Transition-Metal Complexes*. Journal of the American Chemical Society, 1995. **117**(20): p. 5614-5615.
52. Patten, T.E. and K. Matyjaszewski, *Atom transfer radical polymerization and the synthesis of polymeric materials*. Advanced Materials, 1998. **10**(12): p. 901-+.
53. Wang, X.S., R.A. Jackson, and S.P. Armes, *Facile synthesis of acidic copolymers via atom transfer radical polymerization in aqueous media at ambient temperature*. Macromolecules, 2000. **33**(2): p. 255-257.
54. Huang, W.X., et al., *Functionalization of surfaces by water-accelerated atom-transfer radical polymerization of hydroxyethyl methacrylate and subsequent derivatization*. Macromolecules, 2002. **35**(4): p. 1175-1179.
55. Jones, D.M., A.A. Brown, and W.T.S. Huck, *Surface-initiated polymerizations in aqueous media: Effect of initiator density*. Langmuir, 2002. **18**(4): p. 1265-1269.
56. Jones, D.M. and W.T.S. Huck, *Controlled surface-initiated polymerizations in aqueous media*. Advanced Materials, 2001. **13**(16): p. 1256-1259.
57. Husseman, M., et al., *Controlled synthesis of polymer brushes by "Living" free radical polymerization techniques*. Macromolecules, 1999. **32**(5): p. 1424-1431.
58. Huang, X. and M.J. Wirth, *Surface initiation of living radical polymerization for growth of tethered chains of low polydispersity*. Macromolecules, 1999. **32**(5): p. 1694-1696.
59. Huang, X.Y. and M.J. Wirth, *Surface-initiated radical polymerization on porous silica*. Analytical Chemistry, 1997. **69**(22): p. 4577-4580.

Chapter 2: Surface-Based Polymerization in Porous Silicon

2.1 Project Goals and Motivation

The focus of Chapters 2 and 3 is the polymerization of methyl methacrylate (MMA), in confined concave geometries. The chief goal of these chapters is to study the effect of the confinement due to the concave geometry on the polymerization process that is initiated inside the small pores. Specifically, will this geometry limit the molecular weight of the grown polymer as compared to a planar, non-porous surface? Moreover, will this geometry have any influence on the polydispersity of the resulting polymer?

Another reason for studying the polymerization in porous silicon was to investigate if this support can act as a platform to characterize the surface grown polymer using Matrix Assisted Laser Desorption Ionization (MALDI) [1-3]. The latter goal is important, as currently there is no direct method [4-6], which would facilitate to directly measure the molecular weight and molecular weight distribution of polymers grown off surfaces. Here, attempts are described to employ MALDI to directly analyze the molecular weight distribution of surface-grown polymers.

Several previous studies demonstrated that the conventional organic matrix used in MALDI might be replaced with porous silicon when analyzing the molecular weight of oligomeric species [1, 3, 7] using so-called Desorption Ionization on Silicon (DIOS). It was reckoned that the DIOS technique could potentially have additional advantages as well. First, porous silicon has a high surface area and could provide a greater number of initiating

sites for the polymer chains to grow from. DIOS has the added advantage of eliminating the extra signal associated with the organic matrix normally used to analyze synthetic polymers [1, 8-10]. Thus, if low molecular weight fractions of the polymer existed on the surface, their presence would not be obscured by matrix. In order to explore the effect of the size of the pore on the polymerization, we utilize two substrates with different pore sizes. One substrate of interest to us is anodic aluminum oxide (AAO), a commercially available substrate with a homogeneous pore size (0.2 μm). The first substrate studied is porous silicon (p-Si) with pore sizes of <50 nm.

2.2 Polymer brushes prepared via ATRP

2.2.1 Polymer brushes prepared via “grafting from” versus “grafting to”

The methodology for undertaking this study involved several steps. First, a reliable and reproducible method of covering the surfaces of the capillaries with the polymer had to be established. There are two ways of tethering a polymer to a surface: 1) “grafting from” and 2) “grafting onto” approaches. The “grafting onto” technique forms surface-anchored polymers by chemisorbing functionalized polymers from solution onto the substrate. The “grafting from” method uses a substrate covered with chemisorbed initiator molecules, which then act as seeds for polymer growth directly off the surface. The “grafting onto” method generally leads to brushes with very low grafting densities, due to the entropy barrier associated with packing the chains onto the surface and stretching them in order to increase their grafting density. The confinement present in the concave geometry would likely minimize the amount of polymer that can be delivered inside the pores. Because of those two limitations, in our work we have adopted the “grafting from” method [11-13].

2.2.2 Initiator systems

In order to immobilize the initiator molecules onto the surfaces of the pores, we have utilized the organosilane-based chemistry. Organosilane molecules readily chemisorb onto surfaces covered with a thin oxide layers by reacting with the surface-bound hydroxyl groups [14-16]. In our study surfaces comprising silicon oxide on silicon and aluminum oxide on alumina will be used.

The next issue at hand was to determine how to construct a reliable, reproducible self-assembled monolayer (SAM) of the initiator on the substrate. The first initiator system explored was adopted from the literature and involved a two-step surface-confined-synthesis [17]. The reactions are shown below in Figure 2.1.

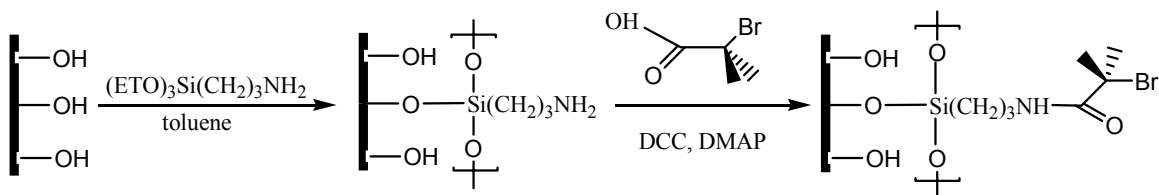


Figure 2.1 – Two-step surface synthesis of polymerization initiator.

The synthesis shown above in Figure 2.1 proved to be unreliable and very time consuming. The vapor deposition of aminopropyltriethoxysilane consisted of refluxing a 10 mM solution of (APTES) in toluene while the silicon wafers were suspended in the condensing vapors. While contact angles measured on APTES self-assembled monolayers (SAMs) deposited onto flat silica-covered substrates were usually around 55° [18], ellipsometry results revealed that multilayers of APTES were formed. Multilayers seem evident by the fact that the

thickness of the aminopropyl layer was generally above 35 Å, while a value based upon a simple molecular model of the molecule in an extended conformation suggests a maximum thickness of 20 Å. Thus it was concluded that this methodology was not reliable to obtain well-ordered SAMs of APTES.

A second approach that was ultimately adopted for all subsequent studies was the use of [(11-(2-Bromo-2-methyl) propionyloxy) undecyltrichlorosilane (BiB) as a surface-bound initiator. BiB was synthesized by adopting a procedure from the literature [19]. The initiator was deposited on the surface of ultraviolet/ozone (UVO)-treated silicon in anhydrous toluene at -10°C. Figure 2.2 illustrates the chemistry behind this one step initiator deposition.

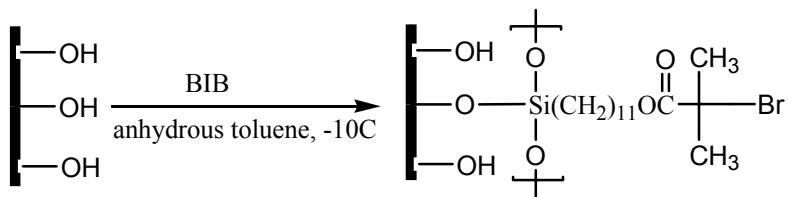


Figure 2.2 – One step surface synthesis of [(11-(2-Bromo-2-methyl)propionyloxy) undecyltrichlorosilane.

2.2.3 Optimization of initiator deposition conditions

The initiator was reported [19] to yield high coverage SAMs at 25°C but through our investigation it was determined that the low temperature deposition was required. Trial and error experiments in conjunction with a battery of experimental probes revealed that the optimal conditions for preparing dense and well-organized SAMs of BiB involve depositions carried out at -10°C for 15 hours from anhydrous toluene solutions. Experiments using near edge x-ray absorption fine structure (NEXAFS) spectroscopy revealed that at those deposition conditions, the BiB molecules formed well-organized and densely packed SAMs.

In Figure 2.3 the carbon K-edge NEXAFS spectra for BiB SAMs deposited under various conditions are shown. The intensity of the carbonyl bond ($E=284$ eV) for varying conditions of initiator deposition indicates that sample 3 shows the strongest intensity. Thus, it was concluded that lower reaction temperatures, but longer reaction times were optimal for preparation of this initiating SAM. Ellipsometry measurements on a similarly prepared sample gave a thickness of 18 \AA , a value that is expected for a densely packed SAM based upon the models of BiB molecules in an extended geometry. This initiator-SAM had previously been used to initiate polymerization of (tert-butyl acrylate) and styrene [19]. Moreover, bromopropionic-terminated initiators had been shown to polymerize polyacrylamide [17] and poly(methyl methacrylate) [20]. Thus we deemed the BiB-SAM initiator a good candidate for use in this work. The next step was to find an appropriate medium to carry out the polymerization.

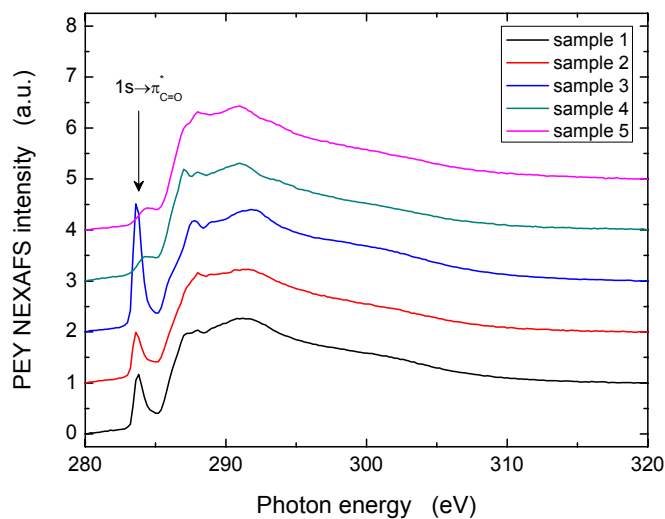


Figure 2.3 Normalized carbon edge data for various monolayer deposition temperatures and times (cf. Table 1). The data have been shifted vertically for clarity

Table 2.1 Description of the deposition conditions used in the NEXAFS experiments.

Sample #	Deposition Conditions	
Sample 1	-10°C for 1.5 hrs	
Sample 2	-10°C for 10 hrs	
Sample 3	-10°C for 15 hrs	
Sample 4	25°C for 1.5 hrs	
Sample 5	25°C for 15 hrs	

2.2.4 Aqueous based ATRP

The room temperature aqueous/solvent-based atom transfer radical polymerization (ATRP) system discussed earlier was chosen for the polymerization of methyl methacrylate[4, 6, 17, 20-23]. The composition of the polymerization solution was 50% monomer, 40% methanol (to solvate the monomer in water), and 10% water. The polymerization system also contained a catalyst, Cu(I)Cl, and an inhibitor, Cu(II)Cl₂. 2,2'-Dipyridyl was added as a ligand to complex with the copper compounds, which facilitated the polymerization and kept the whole system homogeneous. This setup closely followed the work done by Huck and Jones [21]. The use of this system produced a homogeneous solution that kept the growing polymer chains solvated throughout the entire reaction time.

2.3 Polymer Growth in Porous Silicon: Characterization via Infrared Spectroscopy (IR)

Infrared (IR) spectroscopy was used to follow the surface modification steps. The IR spectra generated a very clear picture about the transformation from p-Si to PMMA-modified

p-Si. The overlaid transmission IR data in Figure 2.4 shows the attachment of the BiB initiator to the surface of the porous silicon wafer (N-type, Antimony doped, 0.01-0.02 ohm·cm, supplied by Silicon Valley Microelectronics, Inc.). The main feature in this step is the appearance of a carbonyl stretch at $\approx 1732\text{ cm}^{-1}$ in the spectrum A of Figure 2.4. This feature was not observed prior to treatment of the porous silicon with BiB.

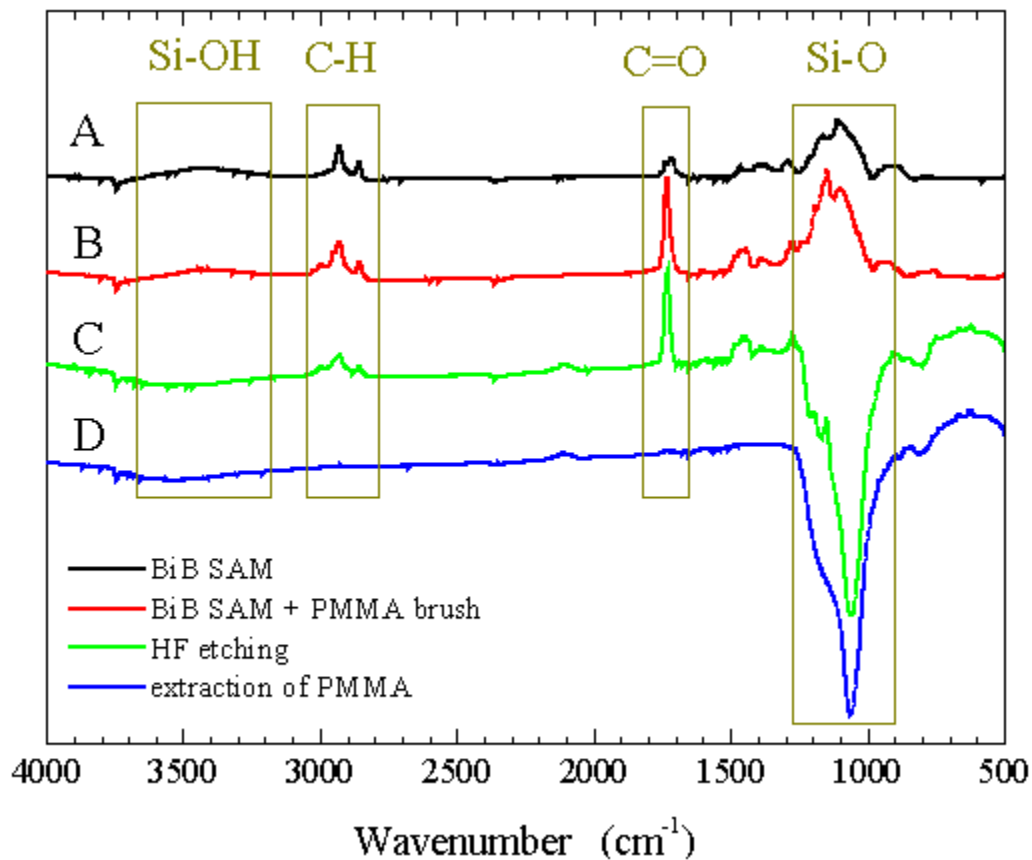


Figure 2.4 – IR of BiB deposition, PMMA growth, HF vapor etch, and PMMA extraction.

The polymer brush was then grown using the “grafting from” ATRP technique described earlier. The main characteristic for the presence of surface-bound PMMA is the slight shift and an increase in the relative intensity of the carbonyl stretch at $\approx 1738\text{ cm}^{-1}$, which can be observed by comparing spectrum B with spectrum A in Figure 2.4. As expected, after

polymerization, the carbonyl stretch intensity increases because of the increased number of C=O bonds that are in each repeat unit of the polymer. After polymerization, the sample was treated with HF vapor with the purpose of cleaving the Si-O bonds and to detach the polymer from the surface. This procedure was performed so that the polymer molecules could subsequently be desorbed/ablated for analysis via MS-DIOS. As expected, a loss of the Si-O peak ($\approx 1100\text{ cm}^{-1}$) was observed by comparing spectrum C with spectrum B in Figure 2.4. In order to confirm the polymer cleavage, the sample was extracted with methylene chloride to remove any physisorbed polymer. The disappearance of the carbonyl stretch after this procedure indicated that the polymer could be removed in this manner. After the methylene chloride extraction, the loss of the carbonyl stretch at 1738 cm^{-1} can be observed by comparing spectrum D with spectrum C in Figure 2.4. This experiment shows that both polymerization of PMMA and its cleavage from p-Si are feasible.

2.4 Mass Spectrometry of Absorbed Polymers

Desorption Ionization on Silicon (DIOS) has the potential advantage of using the same substrate for surface synthesis and the possibility of yielding a direct measure of molecular weight without the addition of a matrix for mass spectrometry analysis. The application of DIOS would require (1) illustrating the ability to grow the polymer brush in porous silicon (p-Si) (shown above via IR) and (2) finding a way to desorb/ablate the polymer from the surface so the grown chains would be detected by the mass spectrometer. The surface chemistry of p-Si is the same as hydride-terminated flat silicon; the difference is primarily the concave geometry of the pores. An advantage of this geometry is the greater surface area for polymerization, which facilitates easier sample analysis [1, 3, 24].

2.4.1 MALDI analysis of absorbed polymers

The next task was to analyze the molecular weight of the grown PMMA via DIOS. First, it was necessary to establish the feasibility of using MS-DIOS for analyzing PMMA by utilizing polymer standards of known molecular weight via MALDI. The pore size and overall morphology of the porous silicon are the key factors that allow the p-Si to act as a matrix [3, 24]. First, however, gaining an understanding of the capabilities of MALDI with a conventional matrix was required to compare with the DIOS technique. These experiments allowed the limits of molecular weight detection with the instrument to be tested using a conventional matrix with known standards. It has been reported previously that the upper limit of MALDI analysis on PMMA using conventional techniques while still being able to see each individual repeat unit is around 15 kDa [25-27].

Our MALDI analysis showed high signal-to-noise ratios for low molecular weight polymers. The spectra of 1.8, 3.25, 6.4, and 6.6 kDa PMMA are shown in Figures 2.5. These spectra were obtained by using 0.1M α -cyano-hydroxycinnamic acid as the matrix in a five to one ratio of matrix to PMMA standard (0.1 mM). The signal-to-noise ratio deteriorated once the molecular weight exceeded 15 kDa. Figure 2.6 shows the MALDI spectra of two higher molecular weight PMMA standards with M_n values of 12.3 and 22.2 kDa, respectively. The individual repeat unit is no longer observable in the second spectrum with $M_n = 22.2$ kDa. The signal-to-noise also decreases significantly for a sample with this higher molecular weight.

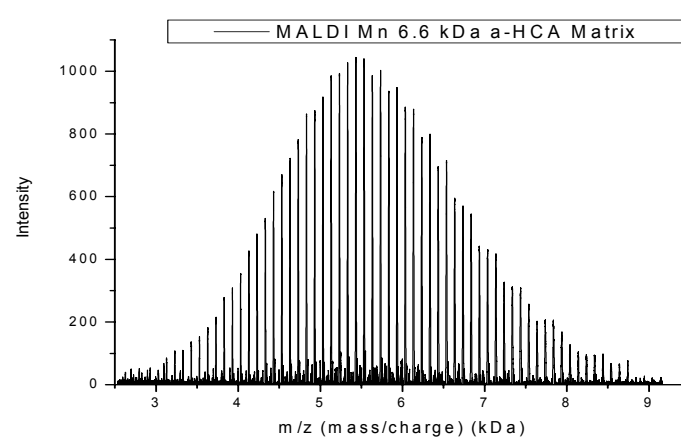
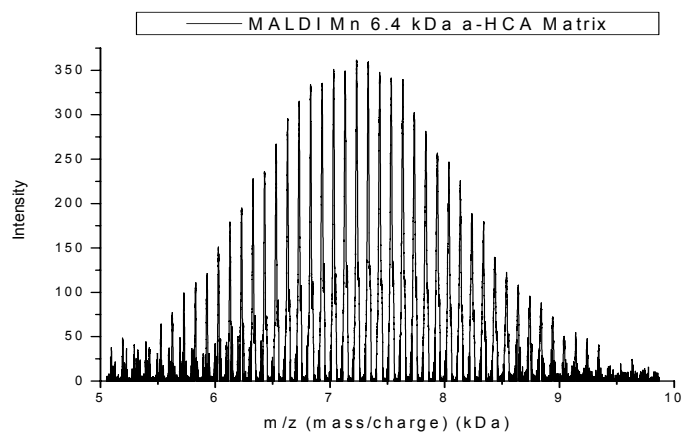
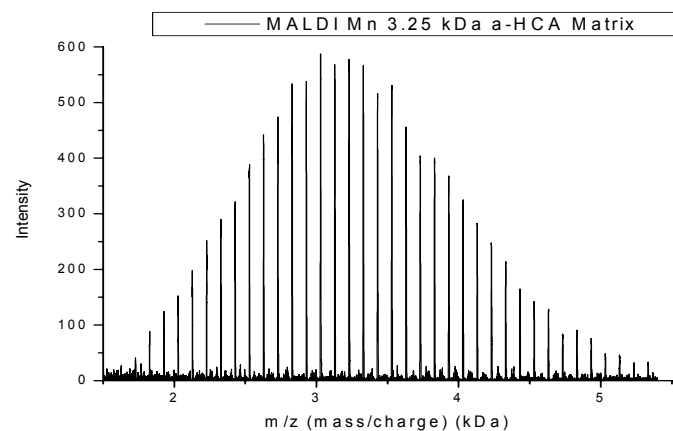
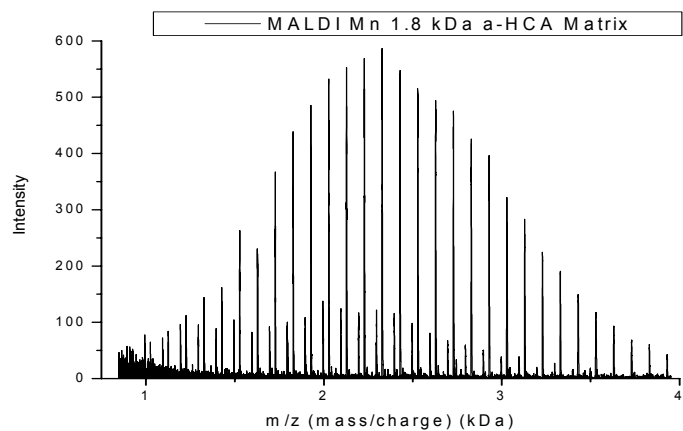


Figure 2.5 – MALDI spectra of four poly methyl methacrylate standards with nominal molecular weights of 1.8, 3.25, 6.4, and 6.6 kDa, respectively. The spectra are presented (top left to bottom right) according to the number average molecular weight provided by the manufacturer.

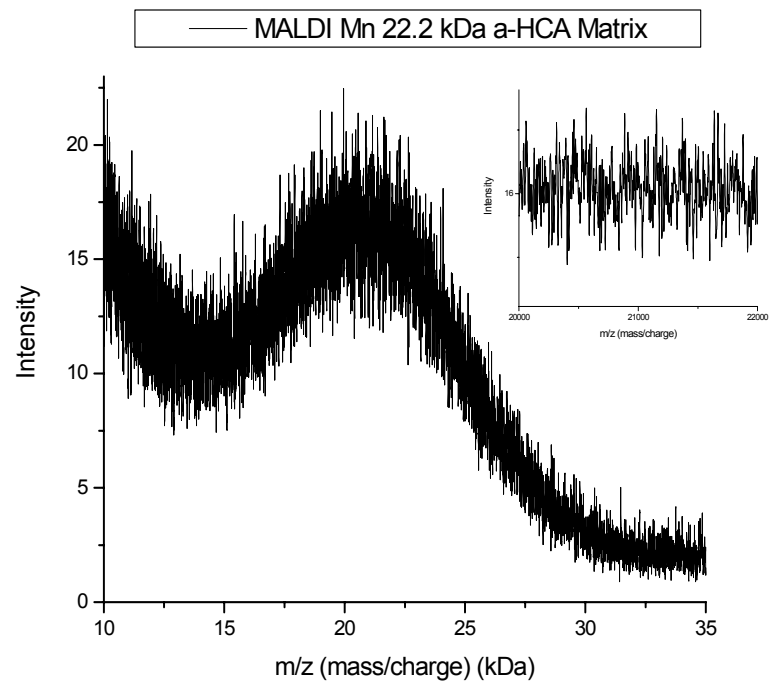
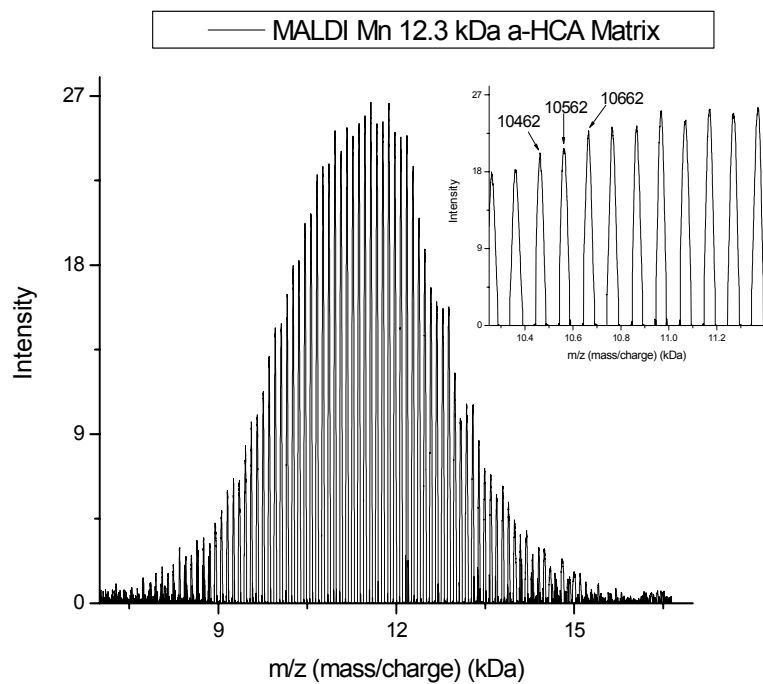


Figure 2.6 – MALDI spectra of two poly methyl methacrylate standards with nominal molecular weights of (left) 12.3 and (right) 22.2 kDa. The repeat unit of one hundred is no longer visible when going from the top spectrum to the bottom spectrum. The signal-to-noise is also significantly decreased.

2.4.2 DIOS analysis of absorbed polymers

The next step was to test the effectiveness of detecting PMMA standards using MS-DIOS before confronting the potential added complexities of molecular weight analysis of surface-grown polymer chains. Spectra were collected for the 1.8, 3.25, 6.4 and 6.6 kDa PMMA standards (Figure 2.7) on p-Si without added matrix to assist the ablation [1, 3, 24, 28]. Collection of spectra for the 1.8 and 3.25 kDa standards was accomplished with little effort to optimize the analysis conditions. However, in comparing these four standards, the spectra of the two lower molecular weight PMMA standards exhibited a higher signal-to-noise ratio and yielded higher counts (corresponding to the number of ions collected) than that of the 6.4 kDa and, as discussed further below, the 6.6 kDa standard.

In contrast to the analyses for the two standards with the lower molecular weights, attempts to collect a spectrum of the 6.4 and 6.6 kDa PMMA standard proved much more difficult. In many cases the spectrum collected from the 6.6 kDa PMMA standard had less than a 2 to 1 signal-to-noise ratio. After adjusting the accelerating voltage to optimize the signal a spectrum with better than 2 to 1 signal-to-noise was recorded. The number of counts decreased significantly for the 6.6 kDa spectra but still gave an accurate molecular weight distribution.

The MALDI spectra shown in Figure 2.7 obtained via the MS-DIOS technique has a comparable signal-to-noise ratio as compared to the MALDI spectra presented in Figure 2.5 via the conventional matrix assisted technique. Spectrum from the 6.6 kDa PMMA sample presented in Figure 2.7 appears to have a smaller intensity relative to that depicted in Figure 2.5. Comparing mass spectra obtained with added matrix to mass spectra obtained via the

MS-DIOS technique, the intensity of signal corresponding to the number of ion counts decreases more rapidly with MS-DIOS. This result suggests that the ablation of higher molecular weight species is less efficient in MS-DIOS as compared to the conventional MALDI technique.

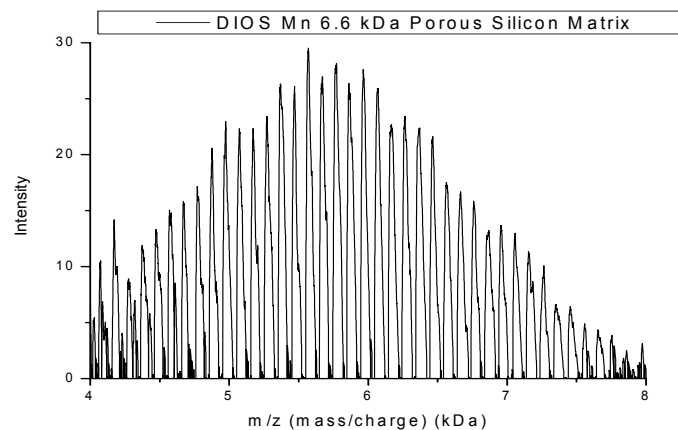
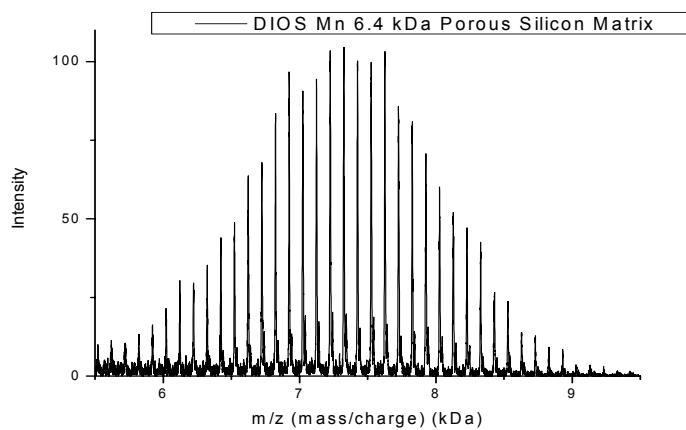
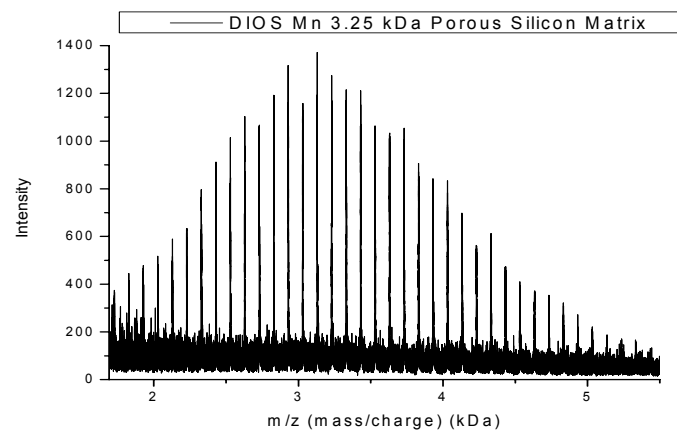
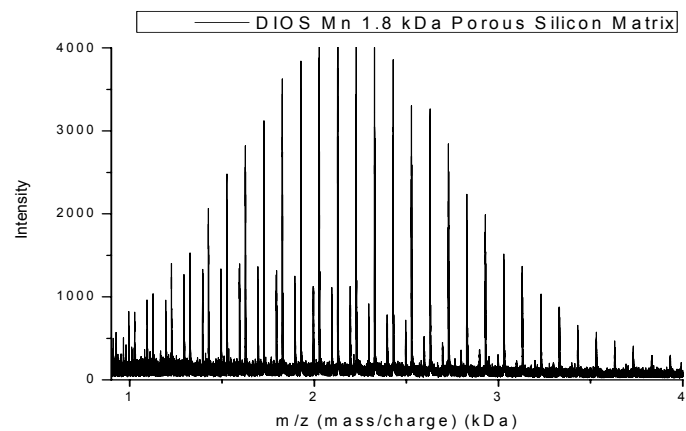


Figure 2.7 – DIOS spectra of four poly methyl methacrylate standards with nominal molecular weights of 1.8, 3.25, 6.4, and 6.6 kDa, respectively. The spectra are presented (top left to bottom right) according to the number average molecular weight provided by the manufacturer.

2.4.3 *Molecular weight analysis of MALDI and DIOS spectra*

The weight average molecular weight (M_w), number average molecular weight (M_n), and polydispersity index (PDI) were calculated using a two parameter Schultz distribution fit [32-33] for the PMMA standards collected using conventional MALDI and via the MS-DIOS technique [29]. The Schultz fit is designed to model the most probable fit for the molecular weight distribution. A “point-by-point” fit was also done yielding results to compare to the Schultz distribution fit. Unlike the Schultz distribution fits, which models the Gaussian curve of the polymers distribution, the point-by-point fit simply takes the local maxima of all the individual monomer units along with the relative intensities to find the M_w , M_n , and PDI. (See Appendix 1 for a complete description of the Schultz and point-by-point fit) The results of the Schultz distribution fit are shown below, Figures 2.8 through 2.12, in ascending order. The PMMA standards are arranged in ascending order with MALDI and MS-DIOS fits of the same M_n arranged as one figure.

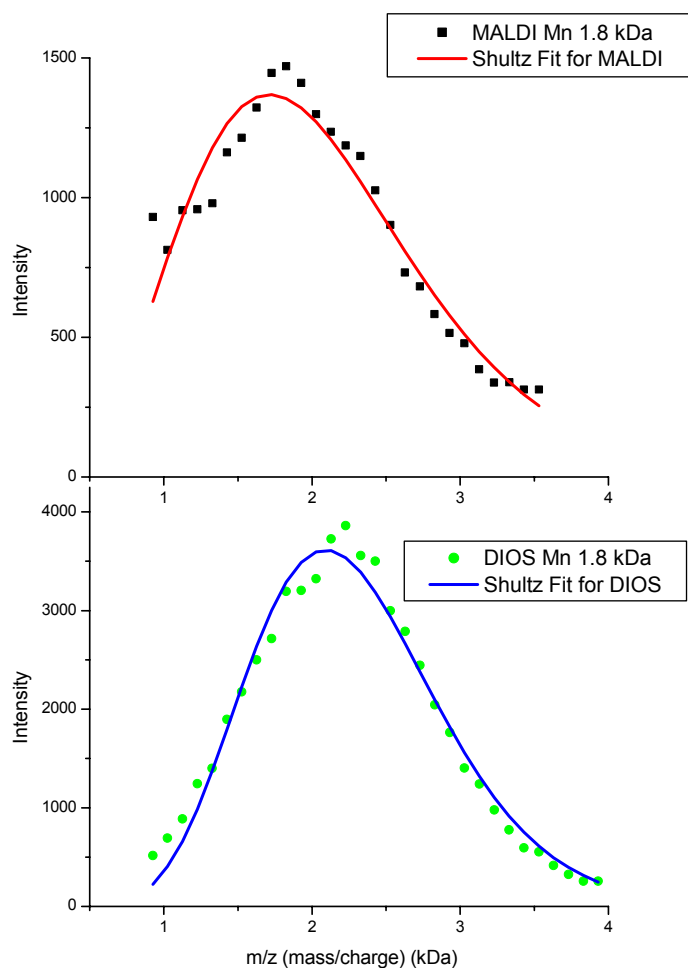


Figure 2.8 – MALDI and DIOS spectra comparison of the Schultz distribution and point by point fit of Poly(methyl methacrylate) standards with nominal molecular weight of 1.8 kDa (information given by manufacturer collected via GPC). The black squares (■) in the top spectrum and the green circles (●) in the bottom spectrum indicate the local maxima for each monomer unit. The line indicating the Schultz distribution fit is shown as a red line (□) in for the MALDI spectra and as a blue line (□) for the DIOS spectra.

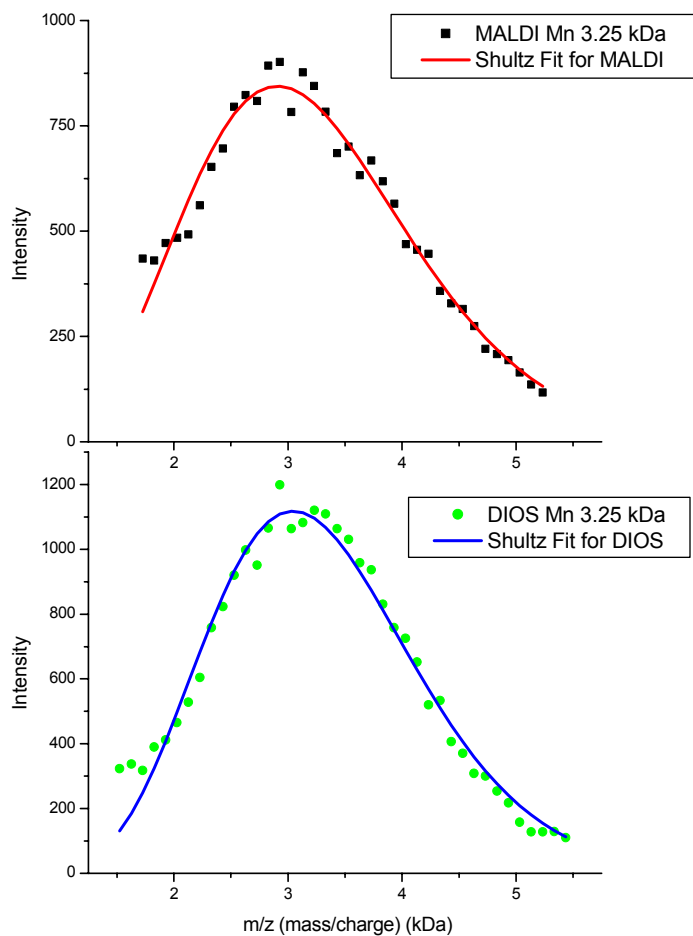


Figure 2.9 – MALDI and DIOS spectra comparison of the Schultz distribution and point by point fit of Poly(methyl methacrylate) standards with nominal molecular weight of 3.25 kDa (information given by manufacturer collected via GPC). The black squares (■) in the top spectrum and the green circles (●) in the bottom spectrum indicate the local maxima for each monomer unit. The line indicating the Schultz distribution fit is shown as a red line (□) in for the MALDI spectra and as a blue line (□) for the DIOS spectra.

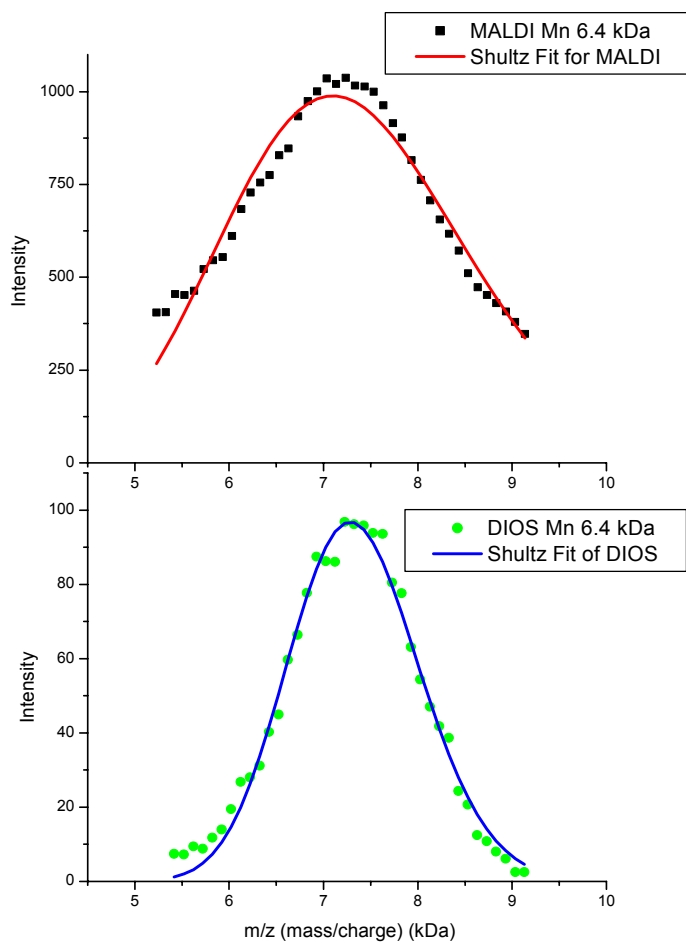


Figure 2.10 – MALDI and DIOS spectra comparison of the Schultz distribution and point by point fit of Poly(methyl methacrylate) standards with nominal molecular weight of 6.4 kDa (information given by manufacturer collected via GPC). The black squares (■) in the top spectrum and the green circles (●) in the bottom spectrum indicate the local maxima for each monomer unit. The line indicating the Schultz distribution fit is shown as a red line (□) in for the MALDI spectra and as a blue line (□) for the DIOS spectra.

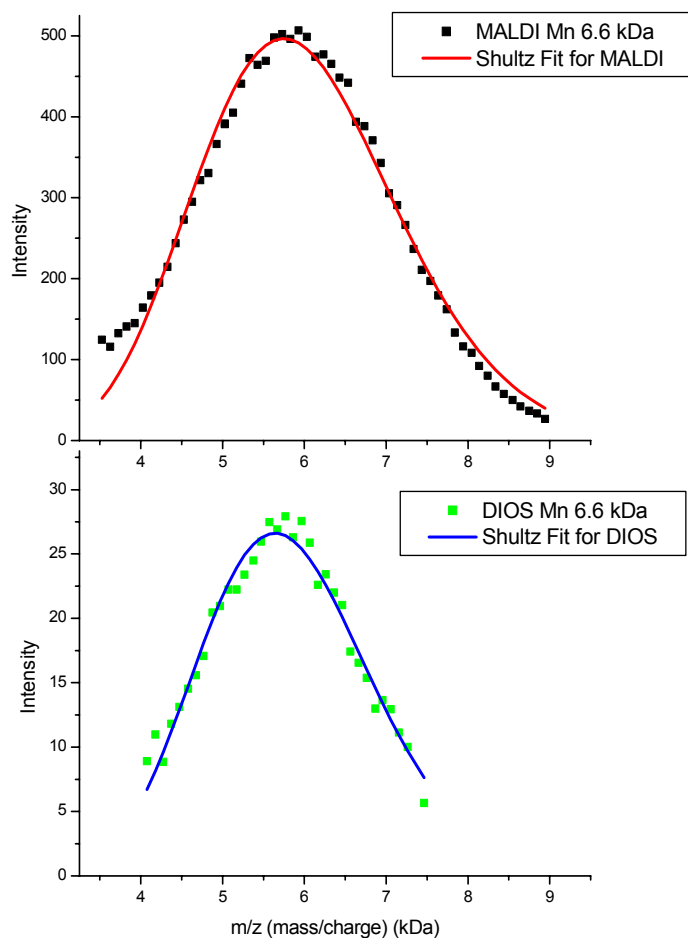


Figure 2.11 – MALDI and DIOS spectra comparison of the Schultz distribution and point by point fit of Poly(methyl methacrylate) standards with nominal molecular weight of 6.6 kDa (information given by manufacturer collected via GPC). The black squares (■) in the top spectrum and the green circles (●) in the bottom spectrum indicate the local maxima for each monomer unit. The line indicating the Schultz distribution fit is shown as a red line (□) in for the MALDI spectra and as a blue line (□) for the DIOS spectra.

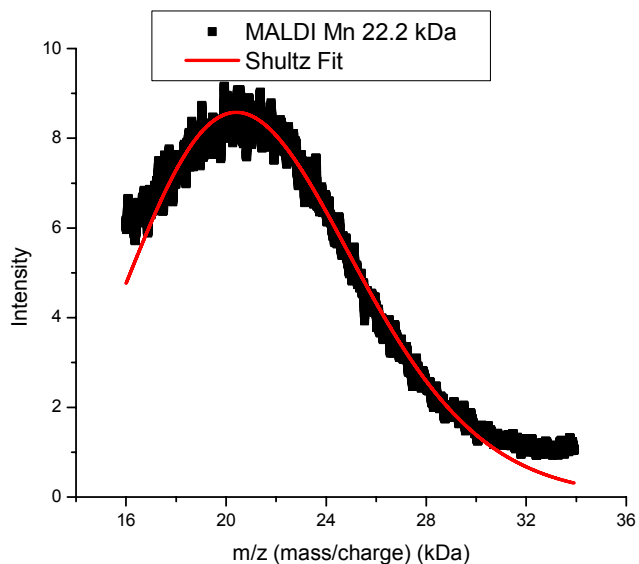
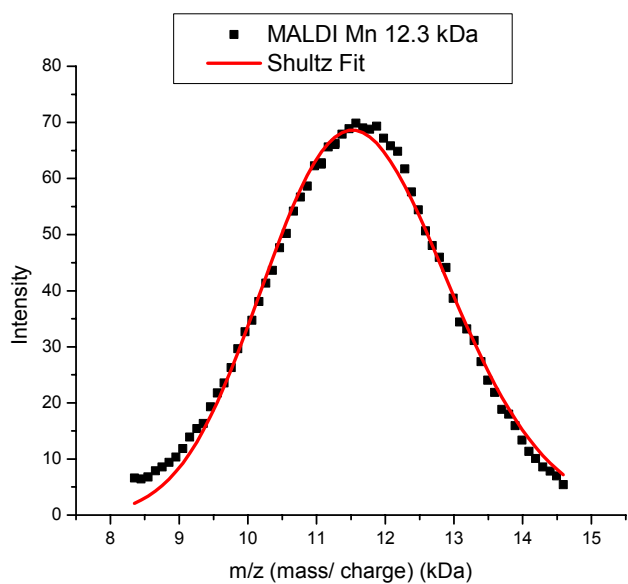


Figure 2.12 – MALDI spectra collected from Poly(methyl methacrylate) standards with nominal molecular weight of 12.3 and 22.2 kDa. The black squares (■) indicate the local maxima for each monomer unit with respect to the 12.2 kDa graph. The black squares (■) indicate all data points for the 22.2 kDa graph. The signal to noise was insufficient to determine local maxima. The Schultz distribution fit is shown as a red line (—) for each MALDI spectra.

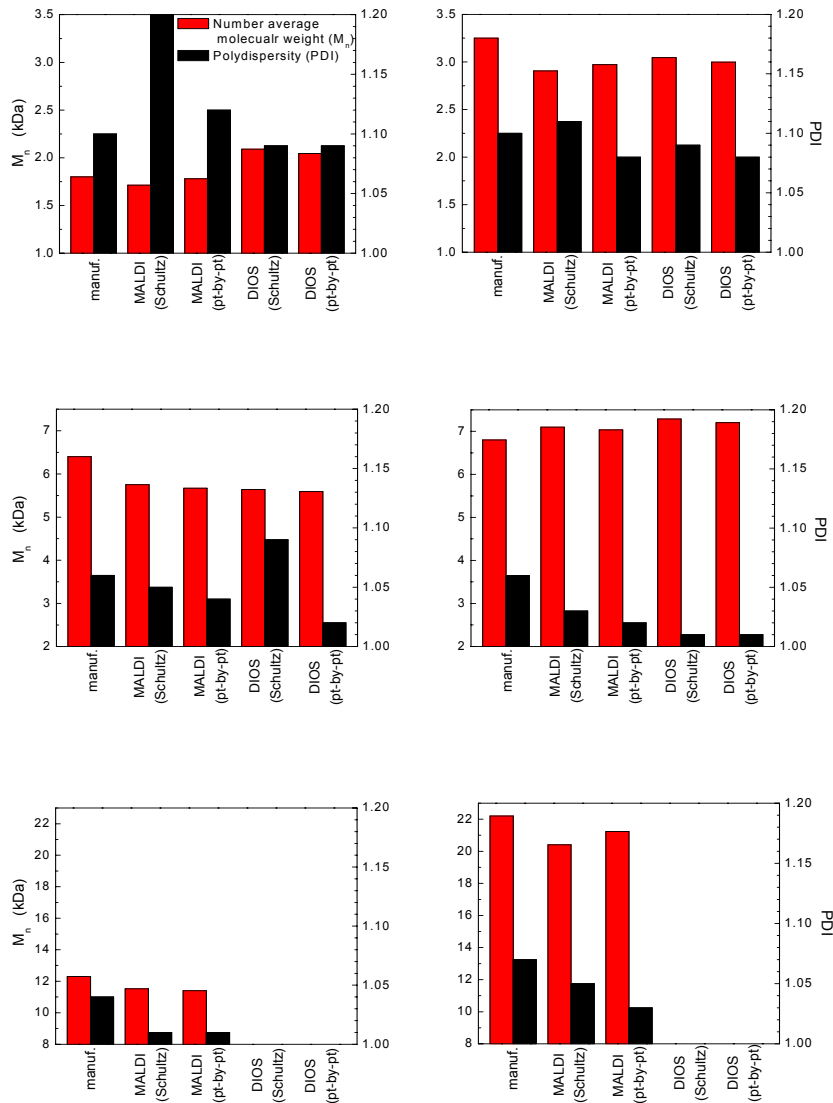


Figure 2.13 – Weight average molecular weight (M_w), number average molecular weight (M_n), and polydispersity index (PDI) values for poly(methyl methacrylate) standards. The manufacturer information is listed first, followed by the values obtained via conventional MALDI (Schultz distribution fit followed by point-by-point fit), and lastly the values obtained using the MS-DIOS technique (Schultz distribution fit followed by point-by-point fit). The manufacturers information was determined with Gel Permeation Chromatography (GPC). A MS-DIOS signal could not be obtained for the 12.3 and 22.2 kDa PMMA standards. The red bar (■) indicates number average molecular weight (M_n). The black bar (■) indicates polydispersity (PDI).

Table 2.2 – Weight average molecular weight (M_w), number average molecular weight (M_n), and polydispersity index (PDI) values for poly(methyl methacrylate) standards. The manufacturer information is listed first, followed by the values obtained via conventional MALDI, and lastly the values obtained using the MS-DIOS technique. The manufacturers information was determined with Gel Permeation Chromatography (GPC). The MALDI and MS-DIOS values were found with a Schultz distribution and point-by-point (Pt-by-Pt) fit.

	PMMA Standard	M_w (kDa)	M_n (kDa)	PDI
PMMA Standard (Manufacturer Info) (GPC)	1	2.00	1.80	1.10
	2	3.60	3.25	1.10
	3	6.80	6.40	1.06
	4	7.00	6.80	1.06
	5	12.90	12.30	1.04
	6	23.80	22.20	1.07
MALDI (Schultz distribution Fit)	1	2.06	1.71	1.20
	2	3.34	2.91	1.11
	3	6.01	5.75	1.05
	4	7.33	7.10	1.03
	5	11.68	11.52	1.01
	6	21.36	20.41	1.05
MALDI (Pt-by-Pt Fit)	1	2.00	1.78	1.12
	2	3.20	2.97	1.08
	3	5.89	5.67	1.04
	4	7.17	7.03	1.02
	5	11.53	11.39	1.01
	6	21.89	21.23	1.03
DIOS (Schultz distribution Fit)	1	2.29	2.09	1.09
	2	3.32	3.05	1.09
	3	5.84	5.64	1.09
	4	7.35	7.29	1.01
	5	No Signal	No Signal	N/A
	6	No Signal	No Signal	N/A
DIOS (Pt-by-Pt Fit)	1	2.23	2.05	1.09
	2	3.24	3.00	1.08
	3	5.71	5.59	1.02
	4	7.29	7.22	1.01
	5	No Signal	No Signal	N/A
	6	No Signal	No Signal	N/A

The results of both the Schultz distribution and point-by-point fits are shown in bar graphs in Figure 2.13. The MALDI and MS-DIOS spectra produced M_n values that are lower than the manufacturers listed molecular weights for every standard except the 6.4 kDa M_n PMMA standard [30]. Polymer Source, Inc. manufactured the 6.4 kDa standard while Polymer Standards Service produced all the other PMMA standards used. The MALDI and MS-DIOS spectra generate very comparable values for M_n , M_w , and PDI. The only exception to this is the high polydispersity found for the 1.8 kDa PMMA specimen by conventional MALDI, using the Schultz distribution fit. The high signal obtained because of low molecular weight material such as matrix and other contaminants made it difficult to attain the individual maxima at a molecular weight below ≈ 1.5 kDa. Table 1.2 gives the specific values for M_n , M_w , and PDI.

2.5 Desorption/ Ionization on Silicon (DIOS): Grown Polymers

Following the MS-DIOS study on polymer standards the next step was to grow polymer in the porous silicon. There are several considerations that may result in a different molecular weight of a polymer grown from a porous substrate from that grown from a less porous substrate. Growing polymer in the confined space of a pore may affect the rate of polymerization and consequently the molecular weight of the brush. The rate and extent of growth may be limited by the restricted rate of diffusion of the monomer and the catalyst into the pore. Thus, a linear molecular weight growth with time and small polydispersity that is normally seen with ATRP in bulk and on flat and convex surfaces may not be observed. Thus, the extent of polymer growth and the molecular weight of the polymer may be limited

by the size of the pore. Finally, the water-based polymerization reaction may prove challenging because of capillary effects that may prevent water from penetrating the small pores. All these issues have one thing in common – they depend upon the size of the pore.

2.5.1 Scanning electron microscopy image of porous silicon

The size of the pore can be tailored by altering the etching conditions during the p-Si substrate preparation. Our etching conditions followed the work done previously by Siuzdak [1]. The most important of these conditions are current density, dopant concentration, and white light intensity. Our p-Si substrate was prepared by electrochemically etching Antimony doped (0.01-0.02 ohm/cm) silicon. The silicon was immersed in a solution of concentrated HF acid and absolute ethanol (50/50 v/v). The immersed silicon sample was then exposed to $50\text{mW}/\text{cm}^2$ of white light while passing $\approx 5\text{mA}/\text{cm}^2$ of current through the etching solution for two minutes. After etching, a 1-minute “post-etch” in aqueous HF was performed. Pores measured by Siuzdak under very similar conditions yielded a diameter of about 70-120 nm and a depth of up to 200 nm [3]. Figure 2.14 shows the scanning electron microscopy (SEM) image of a cross section of a typical piece of porous silicon prepared in this manner. SEM analysis of our p-Si samples indicated a pore size diameter of less than 50 nm and a depth of less than 200 nm.

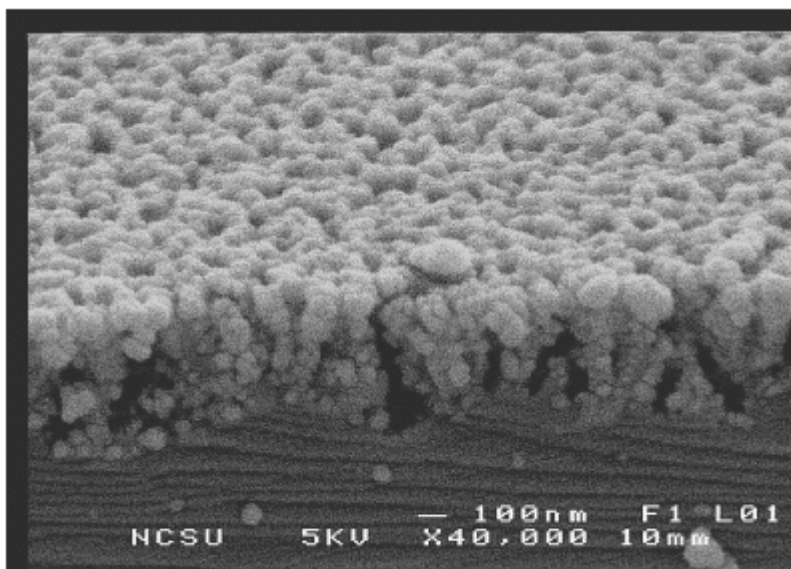


Figure 2.14 – SEM image of porous silicon cross-section. The porous silicon has been sputter coated with gold to increase image resolution.

2.5.2 DIOS on grown PMMA

Initiator was attached to the porous silicon samples and polymerization was carried out using procedures described in the Chapter 2 Experimental. MS-DIOS analysis was carried out on several different samples of varying polymerization time (from 1 hour to 10 hours). Figure 2.15 depicts representative data of the molecular weight of PMMA (grown for 3 hours) directly measured from the surface of porous silicon. The spectrum shows two groups of peaks separated by the mass of the repeat unit (100 Da). Each of these groups presumably differs by the size of the group that has terminated those polymer chains. The value of each respective distribution is xx09 and xx63. The value of the monomer unit increases by 100.1 (the repeat unit of MMA) from 609 to roughly 2509 Da for the xx09 distribution and from 663 to 2563 Da for the xx63 distribution. The signal-to-noise is too

low to observe a peak after 26 kDa. The specific cleavage of the initiator/polymer from the surface is unknown at this time.

Despite varying the polymerization time, the molecular weight of the PMMA measured was never found to be above ≈ 3 kDa. The observed molecular weight using DIOS suggest that the porous nature of the substrate is limiting polymer growth because there is no increase of molecular weight with time.

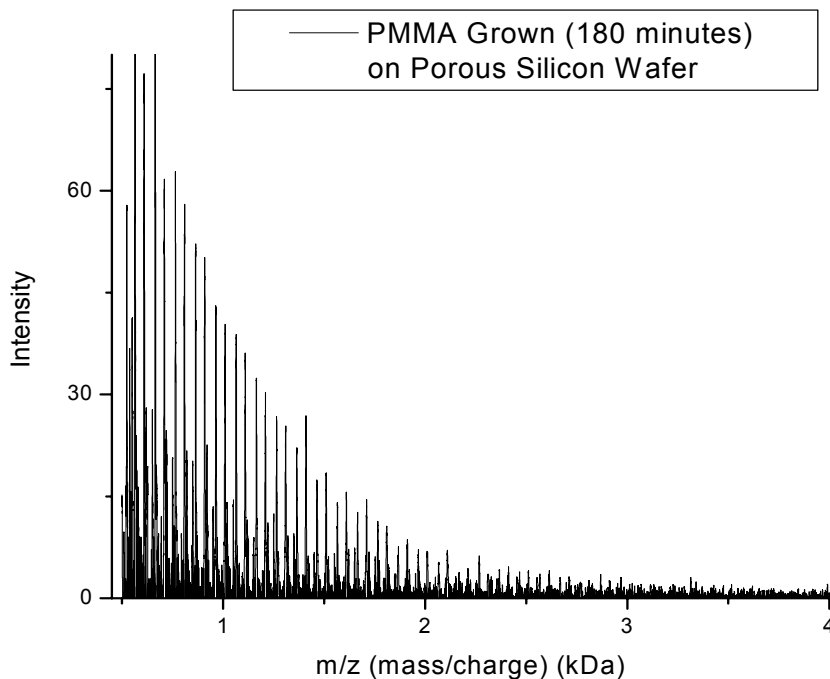


Figure 2.15 – DIOS Spectra of Grown (3 hours) PMMA in Porous Silicon.

There are several factors that may contribute to limiting molecular weight. As stated before, one important issue to consider is the size of the pore, which will severely restrict the space for polymerization and hence the actual size of the polymer chains. In addition, the pore size distribution and pore homogeneity can limit both diffusion of monomer to the

propagating site during growth as well as sterically restrict the propagating site if it becomes inaccessibly trapped within the pore. Another factor contributing to the limited molecular weight observed may be the effectiveness of the current MS-DIOS chip to ablate the polymer from the surface. The spectrum collected on PMMA standards suggests that the current DIOS chip will only ablate efficiently to a molecular weight less than about 10 kDa. However, as the molecular weights measured here are only ca. one third of this cutoff, this latter issue is not the likely reason for the small measured molecular weights.

2.5.3 Reactive ion etched (RIE) porous silicon

Two alternatives were investigated to address the limitation in molecular weight due to both the small diameter and the heterogeneity of the pores: (1) Reactive Ion Etching (RIE) of silicon and (2) commercially available Anodic Aluminum Oxide which will be described later in Chapter 3. RIE was used to create a very homogeneous pore size and distribution of pores [31]. Figure 2.16 shows a SEM image of a typical piece of RIE-etched porous silicon. The pore diameter and the distance between pores were varied and are detailed in Table 2.3. The RIE silicon substrate was polymerized for 2 hours in the water/methanol system described above. A sample MS-DIOS spectrum is presented in Figure 2.17. Unfortunately no signal of grown polymer was attained from this experiment. One reason for no signal is the lack of enough polymer on the surface of the RIE silicon. Another reason was larger pores were used to allow for longer polymer chains to grow. While longer chains may have grown, the pores were likely to large to produce a quality DIOS signal.

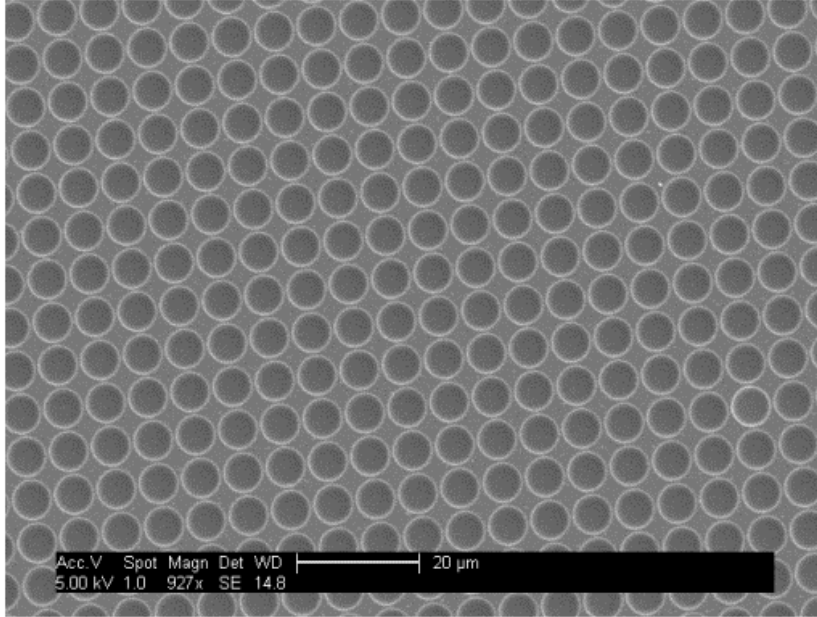
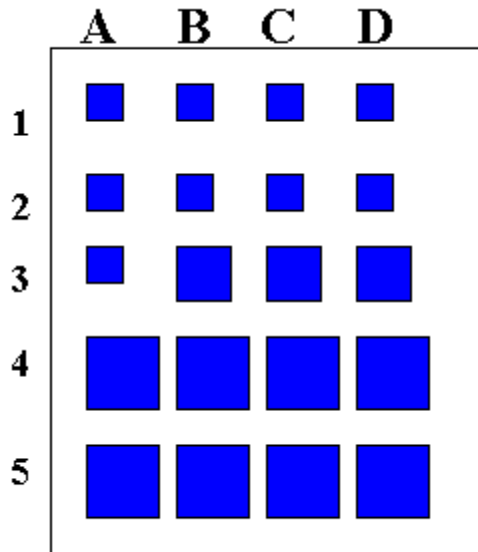


Figure 2.16 – SEM image of Reactive Ion Etched Silicon. Courtesy of Nancy Finkel (NCSU, Chemistry).

Table 2.3 – Chart showing breakdown of pore diameter, period, and the distance between pores for the different areas within the reactive ion etched silicon. Courtesy of Nancy Finkel (NCSU, Chemistry)



A	Pore Diameter (μm)	Blank	3.0	6.4	9.8
	Period (μm)	Blank	3.6	7.5	11.0
	Distance btw pores (μm)	Blank	0.6	1.1	1.2
B	Pore Diameter (μm)	1.0	3.4	6.0	8.4
	Period (μm)	1.6	4.8	9.0	14.0
	Distance btw pores (μm)	0.6	1.4	3.0	5.6
C	Pore Diameter (μm)	1.0	3.4	6.0	8.4
	Period (μm)	2.0	5.8	12	18.0
	Distance btw pores (μm)	1.0	2.4	6.0	9.6
D	Pore Diameter (μm)	1.0	3.3	6.0	8.6
	Period (μm)	2.5	9.5	14	22.0
	Distance btw pores (μm)	1.5	6.2	8.0	13.4

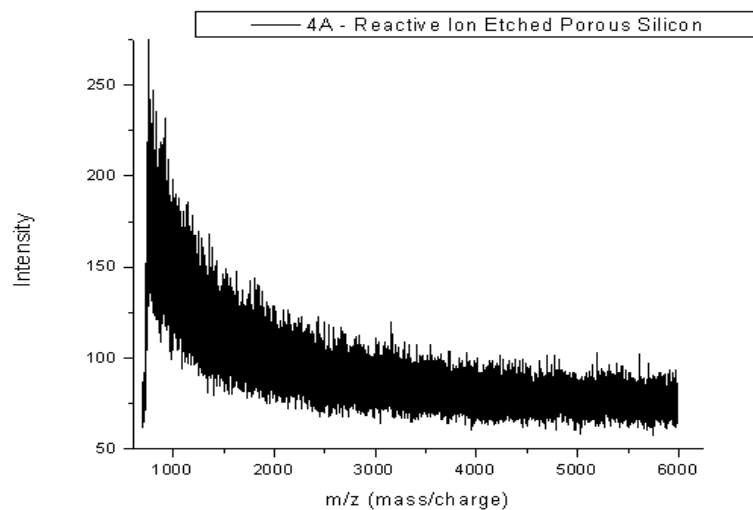


Figure 2.17 – DIOS spectra of RIE silicon. No signal from grown polymer is visible.

2.6 Conclusions

The growth of PMMA on porous silicon and the in situ analysis of the polymer via the DIOS technique were completed. The MALDI spectra of smaller PMMA ($M_n < 6$ kDa) standards collected using porous silicon as a matrix were reproducible and comparable in quality of signal intensity to spectra collected with a conventional matrix. However, larger molecular weight PMMA standards ($6 \text{ kDa} < M_n < 10 \text{ kDa}$) collected with porous silicon as a matrix showed a more rapid decrease in intensity when compared with those recorded using a conventional MALDI matrix. PMMA standards with an $M_n > 10 \text{ kDa}$ could not be collected via the DIOS technique. The inability of the DIOS technique to collect a spectrum of PMMA above 10 kDa reveals a molecular weight limitation with respect to PMMA analysis. Our analysis of PMMA grown on porous silicon reveals that the sub 50 nm pore size inside the porous silicon substrate only allowed for polymers with a maximum of ≈ 20 monomer units to be grown. We attribute the relatively short polymer chains grown due to the small

pores severely restricting the space for polymerization and diffusion of the monomer.

Attempts to create a silicon surface with homogeneous pores using Reactive Ion Etching

(RIE) proved successful but failed to yield a DIOS spectrum. An alternative substrate with

homogenous pores was required to increase molecular weight with an increase in

polymerization time. The alternative investigated was Anodic Aluminum Oxide (AAO).

2.7 Experimental

Preparation of Porous Silicon

The porous silicon substrate was created by electrochemical etching a n-type silicon wafer (Sb-doped, 0.01-0.02 ohm·cm, Silicon Valley Microelectronics) in a Teflon cell, whose configuration was similar to the cell used by Siuzdak et al [3]. The etching solution was a 1:1 (by volume) mixture of concentrated HF (49% Reagent Grade from Fisher) and absolute ethanol (100%, Fisher). The cell compartment that contains the silicon and the etching solution is illuminated with 50mW/cm² of white light from a fiber optic light source (Model I-150, Coherent, Inc.). While illuminated, about 4.6 mA/cm² of constant current is passed through the cell chamber for one minute. After the etching process, the porous silicon (p-Si) sample is washed with absolute ethanol and dried under a nitrogen stream. Following the original etch; a one-minute “post-etch” is performed using a 10% aqueous solution of HF for one minute. After the “post-etch” process, the p-Si sample is washed with absolute ethanol and dried under a nitrogen stream. If the sample was not being used immediately, it was immersed in absolute ethanol until use.

Deposition of Aminotriethoxysilane (APTES)

The synthesis of the two-step surface initiator was adopted from the work of Kong and co-workers [17]. The vapor technique consisted of refluxing a 10 mM solution of aminopropyltriethoxysilane (APTES, 98%, Aldrich) in toluene (Reagent Grade) while the silicon wafers (UVO cleaned, 20 minutes) were suspended in the condensing vapor for 6 hours. The silicon wafer was removed and rinsed with toluene and dried with a gentle stream of nitrogen.

Amidization of APTES with 2-bromoisobutyric acid

The synthesis of the two-step surface initiator was adopted from the work of Kong and co-workers [17].

Synthesis of (11-(2-Bromo-2-methyl)propionyloxy)undecyltrichlorosilane

The synthesis of the surface initiator was adopted from the work of Matyjaszewski and co-workers [19].

Initiator attachment to Porous Silicon

The first step was to attach initiator to the porous silicon substrate. The porous silicon substrate was exposed to ultraviolet/ozone cleaning (UVO) prior to initiator attachment. The (11-(2-Bromo-2-methyl)propionyloxy)undecyltrichlorosilane (BiB) (20 μ L of 5%BiB in anhydrous toluene) was added to cold anhydrous toluene (20mL, 99.8%, Sigma-Aldrich) containing the porous silicon wafer and placed in the freezer ($\approx 0^{\circ}\text{C}$) for at least 12 hours. The p-Si-initiated wafers were rinsed with toluene (Reagent grade) and allowed to dry under a gentle stream of nitrogen. A transmission infrared spectrum was taken of the p-Si substrate following this step as shown in Chapter 2.3.

Polymerization of PMMA in Porous Silicon

Following this, a single homogeneous solution containing all the components needed for the ATRP polymerization of PMMA was prepared. The actual breakdown of monomer/aqueous/solvent makeup for the polymerization was 34.9g of the methyl methacrylate (MMA, 99%, Alfa Aesar) monomer, 32.2g of methanol (Reagent Grade) (to

solvate the monomer in water), and 7g of DI water. The polymerization system also contained 0.64g of Cu(I)Cl (99%, Aldrich) catalyst and 0.011 g of Cu(II)Cl₂ (99%, Aldrich) inhibitor. 2.06g of 2,2'-Dipyridyl (99%, Aldrich) was added as a ligand to complex with the copper compounds and keep the whole system homogenous. The solution was prepared under a constant nitrogen stream in a 200ml two-neck round bottom flask to keep oxygen from penetrating the system. Oxygen will oxidize the Cu(I)Cl. The polymerization solution was then removed with a syringe and placed in 20ml vials that contained a single p-Si wafer functionalized with the BIB initiator. The solution was then bubbled briefly with nitrogen and tightly sealed. The polymerizations were carried out for times ranging from 30 minutes to 10 hours. At the end of each respective time, the polymerization solution was poured into a waste container and the porous silicon wafer was rinsed with methanol and blown dry with a nitrogen stream. A transmission infrared spectrum was taken of the p-Si substrate following this step as shown in Chapter 2.3.

PMMA cleavage from Porous Silicon

The PMMA modified p-Si was placed in Petri dish along with 2-3mL of concentrated HF acid (49% Reagent Grade from Fisher) that was contained in a smaller Petri dish. The HF vapors were allowed to react with Si-O bonds for 40 minutes. A transmission infrared spectrum was taken of the p-Si substrate following this step as shown in Chapter 2.3. For the infrared spectroscopy experiment the PMMA cleaved p-Si substrate was washed with methylene chloride (HPLC Grade, Sigma-Aldrich). A transmission infrared spectrum was taken of the p-Si substrate following this step as shown in Chapter 2.3.

DIOS Analysis of PMMA grown in Porous Silicon

3-5 μL aliquots of THF were dropped onto the surface of the cleaved PMMA modified p-Si in order to draw the polymer out of the pores to the surface for easier ablation. Sodium Trifluoroacetate (NaTFA 98% Sigma-Aldrich) was used to charge the polymer. The sodium trifluoroacetate solution was prepared for concentrations ranging from 0.5-5mg/mL (in THF). 2-3 μL aliquot of the sodium trifluoroacetate were added to the surface of the porous silicon at different positions of the porous silicon substrate to facilitate detection in the MALDI. An Applied Biosystems Voyager STR MALDI-TOF mass spectrometer was used for the molecular weight analysis. It was operated at an accelerating voltage of 20 kV in linear mode and positive ions were collected. Grid voltage was 90%. Laser intensity was adjusted to optimize signal. Generally, laser intensity between 1800-1900 proved sufficient. All settings are specific to the Applied Biosystems Voyager STR MALDI-TOF mass spectrometer.

MALDI Analysis of Adsorbed PMMA

A 5mg/mL (in HPLC grade THF or acetone) solution of PMMA (1.8, 3.25, 6.4, 6.6, 12.3, and 22.2 kDa) (Polymer Standards Service, Inc.) standards was prepared in a small 5ml vial. A 0.1M (in THF) solution of α -cyanohydroxycinnamic acid (99% Sigma-Aldrich) is prepared in a 1mL centrifuge tube. The PMMA standard of interest was then mixed in a specific ratio. The ratio used varied from 3-5 to 1 (by volume) of α -cyanohydroxycinnamic to PMMA standard. The sample target was then loaded in the MALDI. An Applied Biosystems Voyager STR MALDI-TOF mass spectrometer was used for the molecular weight analysis. It was operated at an accelerating voltage of 20 kV in linear mode and positive ions were collected. Grid voltage was 90%. Laser intensity was adjusted to

optimize signal. Generally, laser intensity between 1800-1900 proved sufficient. All settings are specific to the Applied Biosystems Voyager STR MALDI-TOF mass spectrometer.

2.8 References

1. Wei, J., J.M. Buriak, and G. Siuzdak, *Desorption-ionization mass spectrometry on porous silicon*. Nature, 1999. **399**(6733): p. 243-246.
2. Zhang, Q.C., et al., *Desorption/ionization mass spectrometry on porous silicon*. Chinese Journal of Analytical Chemistry, 2001. **29**(12): p. 1365-1369.
3. Shen, Z.X., et al., *Porous silicon as a versatile platform for laser desorption/ionization mass spectrometry*. Analytical Chemistry, 2001. **73**(3): p. 612-619.
4. Huang, X.Y. and M.J. Wirth, *Surface-initiated radical polymerization on porous silica*. Analytical Chemistry, 1997. **69**(22): p. 4577-4580.
5. Ejaz, M., et al., *Controlled graft polymerization of methyl methacrylate on silicon substrate by the combined use of the Langmuir-Blodgett and atom transfer radical polymerization techniques*. Macromolecules, 1998. **31**(17): p. 5934-5936.
6. Huang, X. and M.J. Wirth, *Surface initiation of living radical polymerization for growth of tethered chains of low polydispersity*. Macromolecules, 1999. **32**(5): p. 1694-1696.
7. Kruse, R.A., et al., *Experimental factors controlling analyte ion generation in laser desorption/ionization mass spectrometry on porous silicon*. Analytical Chemistry, 2001. **73**(15): p. 3639-3645.
8. Wu, K.J. and R.W. Odom, *Characterizing synthetic polymers by MALDI MS*. Analytical Chemistry, 1998. **70**(13): p. 456A-461A.
9. Pasch, H. and F. Gores, *Matrix-Assisted Laser-Desorption Ionization Mass-Spectrometry of Synthetic-Polymers .2. Analysis of Poly(Methyl Methacrylate)*. Polymer, 1995. **36**(10): p. 1999-2005.
10. Murgasova, R. and D.M. Hercules, *MALDI of synthetic polymers - an update*. International Journal of Mass Spectrometry, 2003. **226**(1): p. 151-162.
11. Huang, H.Q. and L.S. Penn, *Dense tethered layers by the "grafting-to" approach*. Macromolecules, 2005. **38**(11): p. 4837-4843.
12. Ionov, L., et al., *Gradient mixed brushes: "Grafting to" approach*. Macromolecules, 2004. **37**(19): p. 7421-7423.
13. Biesalski, M. and J. Ruhe, *Synthesis of a poly(p-styrenesulfonate) brush via surface-initiated polymerization*. Macromolecules, 2003. **36**(4): p. 1222-1227.
14. Tillman, N., A. Ulman, and T.L. Penner, *Formation of Multilayers by Self-Assembly*. Langmuir, 1989. **5**(1): p. 101-111.
15. Tillman, N., et al., *Incorporation of Phenoxy Groups in Self-Assembled Monolayers of Trichlorosilane Derivatives - Effects on Film Thickness, Wettability, and Molecular-Orientation*. Journal of the American Chemical Society, 1988. **110**(18): p. 6136-6144.
16. Sagiv, J., *Organized Monolayers by Adsorption .1. Formation and Structure of Oleophobic Mixed Monolayers on Solid-Surfaces*. Journal of the American Chemical Society, 1980. **102**(1): p. 92-98.
17. Kong, X.X., et al., *Amphiphilic polymer brushes grown from the silicon surface by atom transfer radical polymerization*. Macromolecules, 2001. **34**(6): p. 1837-1844.

18. Bain, C.D., J. Evall, and G.M. Whitesides, *Formation of Monolayers by the Coadsorption of Thiols on Gold - Variation in the Head Group, Tail Group, and Solvent*. Journal of the American Chemical Society, 1989. **111**(18): p. 7155-7164.
19. Matyjaszewski, K., et al., *Polymers at interfaces: Using atom transfer radical polymerization in the controlled growth of homopolymers and block copolymers from silicon surfaces in the absence of untethered sacrificial initiator*. Macromolecules, 1999. **32**(26): p. 8716-8724.
20. Huang, W.X., et al., *Functionalization of surfaces by water-accelerated atom-transfer radical polymerization of hydroxyethyl methacrylate and subsequent derivatization*. Macromolecules, 2002. **35**(4): p. 1175-1179.
21. Jones, D.M. and W.T.S. Huck, *Controlled surface-initiated polymerizations in aqueous media*. Advanced Materials, 2001. **13**(16): p. 1256-1259.
22. Jones, D.M., A.A. Brown, and W.T.S. Huck, *Surface-initiated polymerizations in aqueous media: Effect of initiator density*. Langmuir, 2002. **18**(4): p. 1265-1269.
23. Robinson, K.L., et al., *Controlled polymerization of 2-hydroxyethyl methacrylate by ATRP at ambient temperature*. Macromolecules, 2001. **34**(10): p. 3155-3158.
24. Tinsley-Bown, A.M., et al., *Tuning the pore size and surface chemistry of porous silicon for immunoassays*. Physica Status Solidi a-Applied Research, 2000. **182**(1): p. 547-553.
25. Jackson, A.T., et al., *Utilizing time-lag focusing matrix-assisted laser desorption/ionization mass spectrometry for the end group analysis of synthetic polymers*. Rapid Communications in Mass Spectrometry, 1997. **11**(5): p. 520-526.
26. Nielen, M.W.F., *Maldi time-of-flight mass spectrometry of synthetic polymers*. Mass Spectrometry Reviews, 1999. **18**(5): p. 309-344.
27. Jackson, A.T., et al., *Time-lag focusing and cation attachment in the analysis of synthetic polymers by matrix-assisted laser desorption ionization-time-of-flight mass spectrometry*. Journal of the American Society for Mass Spectrometry, 1997. **8**(2): p. 132-139.
28. Seino, T., et al., *Laser desorption/ionization on porous silicon mass spectrometry for accurately determining the molecular weight distribution of polymers evaluated using a certified polystyrene standard*. Analytical Sciences, 2005. **21**(5): p. 485-490.
29. Zimm, B.H., *Apparatus and Methods for Measurement and Interpretation of the Angular Variation of Light Scattering - Preliminary Results on Polystyrene Solutions*. Journal of Chemical Physics, 1948. **16**(12): p. 1099-1116.
30. Jackson, C., B. Larsen, and C. McEwen, *Comparison of most probable peak values as measured for polymer distributions by MALDI mass spectrometry and by size exclusion chromatography*. Analytical Chemistry, 1996. **68**(8): p. 1303-1308.
31. Finkel, N.H., et al., *Ordered silicon nanocavity arrays in surface-assisted desorption/ionization mass spectrometry*. Analytical Chemistry, 2005. **77**(4): p. 1088-1095.
32. Peebles, L.H. *Molecular Weight Distribution in Polymers*; Wiley-Interscience: New York, 1971.
33. Schultz, G.V.Z. *Phys. Chem.* 1939, B43, 25.

Chapter 3: Surface-Based Polymerization in Anodic Aluminum Oxide

3.1 Motivation

MS-DIOS has previously proven to be effective in determining the molecular weight of proteins [1-5]. We have shown that it can be used to show the molecular weight of ATRP-grown PMMA in situ as well. Unfortunately, the limitation of the pore size on the ATRP growth of the PMMA only allows for a polymer brush of two to three thousand molecular weight. A substrate with a larger and more homogeneous pore size is required to allow for larger polymer chains to be grown.

Anodic Aluminum Oxide (AAO) was seen as an alternative to grow larger PMMA, however AAO does not possess porous silicon's unique quality of being a matrix replacement. Thus, the molecular weight analysis had to be done ex situ. Anodic Aluminum Oxide (AAO) was explored as a possible substrate replacement for porous silicon as a substrate upon which to grow and to evaluate the molecular weights of polymer brushes. AAO is used as a nano/micron pore sized filter and as a template for the production of carbon nanotubes [6-9]. The larger pore size in AAO (0.2 μm) relative to porous silicon (p-Si) (≈ 50 nm) should allow for a more constant diffusion of the monomer/catalyst needed for a controlled atom transfer radical polymerization (ATRP) reaction. AAO has the advantage of a homogeneous pore distribution whereas p-Si gave a distribution of pore size upon etching. The pore size can be chosen to fit a specific need since it is available commercially. Figure 3.1 shows an example of a scanning electron microscopy (SEM) image of AAO.

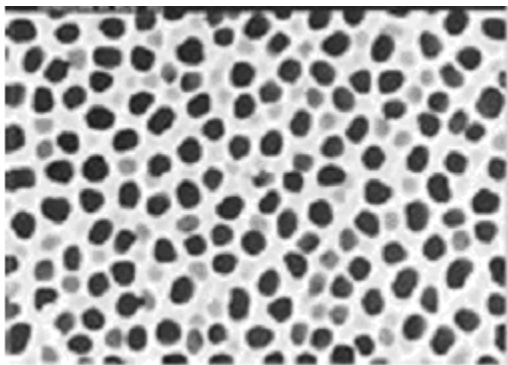


Figure 3.1 – Scanning electron microscopy image of Anodic Aluminum Oxide. Image courtesy of Whatman Corporation.

3.2 Polymer Growth in Anodic Aluminum Oxide: Characterization via Infrared Spectroscopy (IR)

As was discussed before in Chapter 2 for porous silicon, infrared (IR) spectroscopy was used to follow the surface modification steps of the AAO membrane. The IR spectra generated a very clear picture about the transformation from AAO to poly(methyl methacrylate) (PMMA)-modified AAO. The overlaid transmission IR data in Figure 3.2 shows the attachment of the [(11-(2-Bromo-2-methyl) propionyloxy) undecyltrichlorosilane (BiB) monolayer to the surface [10]. The main feature in this step is the appearance of a carbonyl stretch at $\approx 1738\text{ cm}^{-1}$ in spectrum A of Figure 3.2. This feature was not observed prior to treatment of the AAO membrane with BiB. The polymer brush was then grown using the “grafting from” ATRP technique described earlier in Chapter 1 [10-19]. The main characteristic for the presence of pore grown PMMA was a slight shift and an increase in the relative intensity of the carbonyl stretch at 1732 cm^{-1} , which can be observed by comparing spectrum B with spectrum A in Figure 3.2. As expected, after polymerization, the carbonyl stretch has a higher intensity because of the increased number of C=O bonds, each of them

representing a repeat unit of PMMA. After polymerization, the Si-O bonds of the initiator were cleaved with 10% aqueous HF in order to detach the polymer from the surface of the AAO membrane. Subsequently, chloroform was used to separate the surface grown-PMMA from the aqueous HF solution. The chloroform solution containing the surface grown-PMMA was extracted and small drops were placed on an ultraviolet/ozone (UVO)-cleaned silicon wafer (N-type, phosphorus doped, 1-5 ohm/cm², Silicon Valley Microelectronics, Inc.). The chloroform was allowed to evaporate and the transmission IR of the “cleaved PMMA” is shown in spectrum D of Figure 3.2. Spectrum C shows a 1 mM (in chloroform) PMMA standard dropped on a UVO cleaned silicon wafer. The chloroform was allowed to evaporate and a transmission IR was taken of the physisorbed PMMA on the silicon wafer. The spectra are nearly identical confirming the presence of the “cleaved PMMA” in the chloroform of spectrum D. This experiment shows that both polymerization of PMMA and its cleavage from the AAO membrane are feasible.

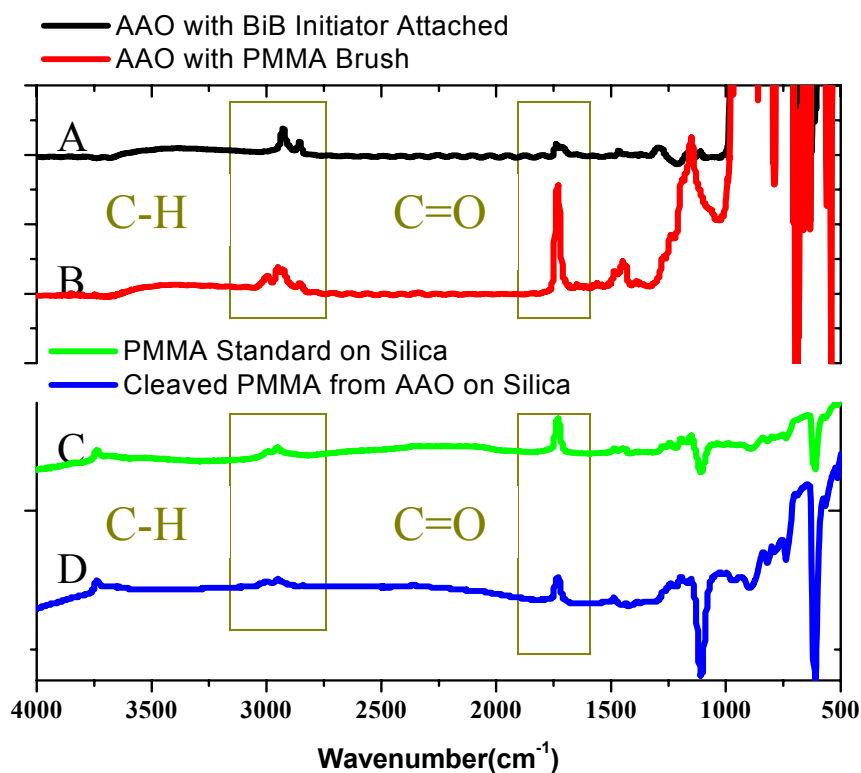


Figure 3.2 – IR of BiB deposition, PMMA growth, PMMA standard on silica, and cleaved PMMA.

3.3 Anodic Aluminum Oxide – Grown Polymers

3.3.1 PMMA cleavage from AAO

The next step was to analyze the molecular weight of the AAO-grown PMMA. Concentrated HF was originally used to dissolve the AAO matrix, thus liberating the PMMA. However, the HF modified the AAO-grown PMMA present. Specifically, the observed repeat unit after treatment with concentrated HF was about 75 Da, which is much lower than the expected 100.1 Da for a neat MMA. The ester functionality present in each MMA monomer units is susceptible to hydrolysis in the presence of a strong acid [20, 21]. Thus, there is a possibility of hydrolysis taking place when exposed to concentrated HF. A similar problem occurred with the cleavage of the PMMA from the porous silicon with HF vapor. The

exposure time was decreased with regards to the porous silicon until the expected repeat unit was observed. For the AAO case, the concentration of the aqueous HF solution was decreased until the expected repeat unit of 100.1 Da was observed as well. Figure 3.3 shows the partial MALDI spectra of AAO-grown PMMA that was cleaved with concentrated HF. Figures 3.4 through 3.7 show MALDI spectra containing repeat units of 100.1 Da. The insert in Figure 3.4 in the bottom spectrum shows a zoomed in MALDI spectrum with a repeat unit of 100.1 Da.

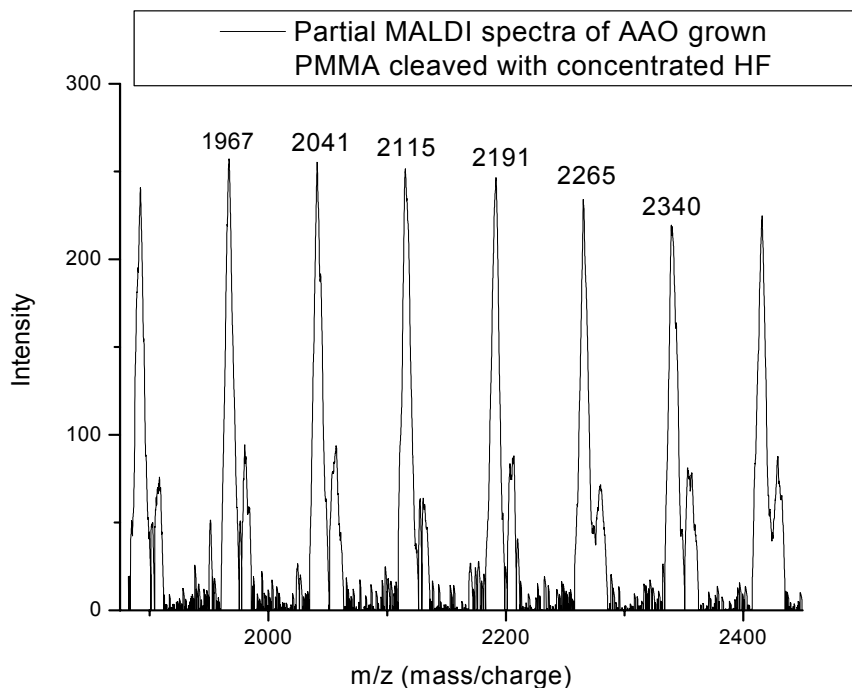


Figure 3.3 – Zoomed in MALDI spectra of a Poly(methyl methacrylate) sample grown for 30 minutes and cleaved from the AAO with concentrated HF. The repeat unit of the HF-modified polymer is approximately 75 Da.

3.3.2 MALDI spectra of cleaved PMMA

After completing the experiments to determine a method to cleave and extract the PMMA from the pores of the AAO, the next step was to grow both pore grown PMMA and solution grown PMMA under the exact same conditions. The polymerizations times were 30, 60, 90, and 130 minutes. The spectra of both the surface and solution grown PMMA are shown below in Figure 3.4 through Figure 3.7 and are arranged according to polymerization time [22-28].

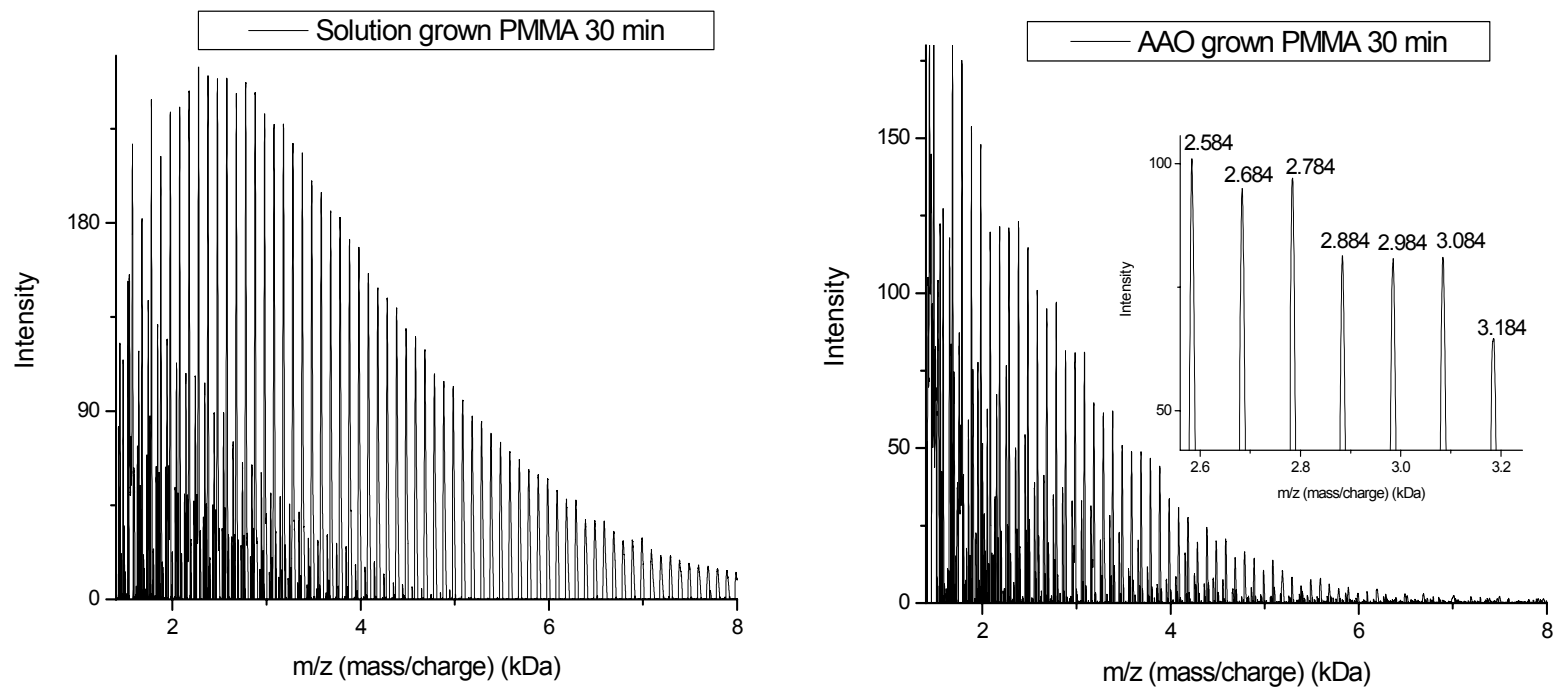


Figure 3.4 – MALDI spectra of two poly methyl methacrylate samples grown for 30 minutes. The left spectrum corresponds to PMMA grown in solution. The right spectrum corresponds to PMMA grown in the pores of an AAO membrane. The inset in the right spectra shows the repeat unit of 100 Da.

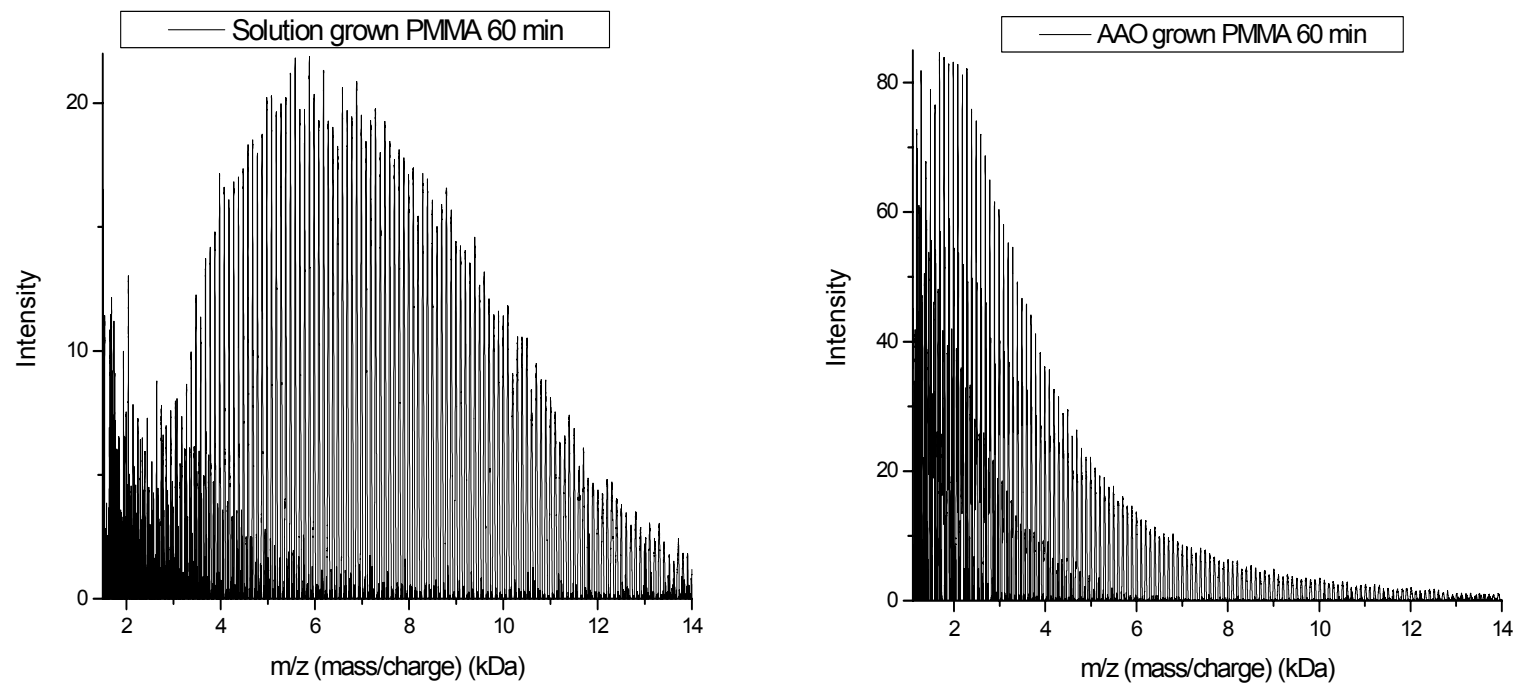


Figure 3.5 – MALDI spectra of two poly methyl methacrylate samples grown for 60 minutes. The top spectrum corresponds to PMMA grown in solution. The bottom spectrum corresponds to PMMA grown in the pores of an AAO membrane.

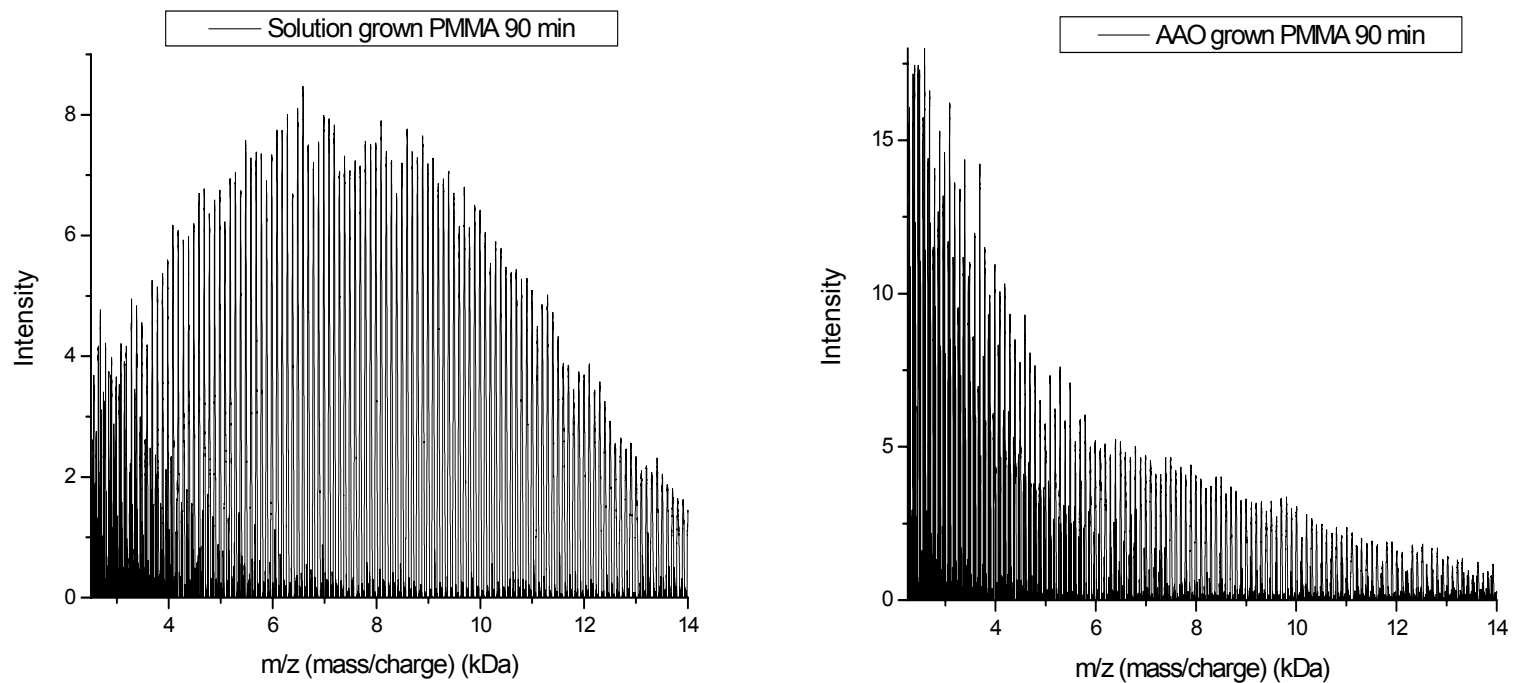


Figure 3.6 – MALDI spectra of two poly methyl methacrylate samples grown for 90 minutes. The top spectrum corresponds to PMMA grown in solution. The bottom spectrum corresponds to PMMA grown in the pores of an AAO membrane.

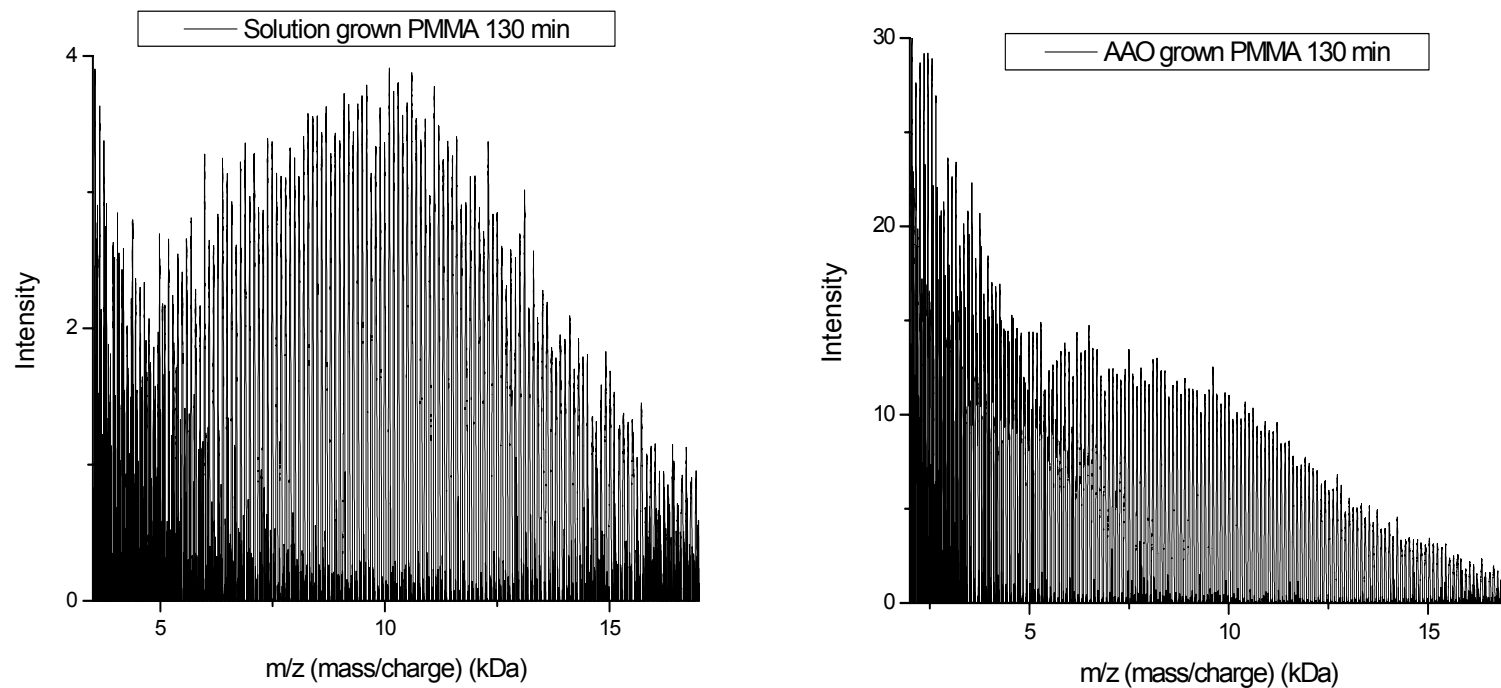


Figure 3.7 – MALDI spectra of two poly(methyl methacrylate) samples grown for 130 minutes. The top spectrum corresponds to PMMA grown in solution. The bottom spectrum corresponds to PMMA grown in the pores of an AAO membrane.

A quick inspection of the MALDI spectra reveals stark differences between the solution- and AAO-grown polymers. For a given polymerization time, the solution polymerization produces polymers with a higher molecular weight relative to the AAO-grown polymers. The weight average molecular weight (M_w), the number average molecular weight (M_n), and the polydispersity index (PDI) were evaluated using both the Schultz distribution fit [34-35] and the “point-by-point” analysis for both solution and AAO-grown polymers [29]. The Schultz fit is designed to model the most probable fit for the molecular weight distribution. A “point-by-point” fit was also done yielding results to compare to the Schultz distribution fit. Unlike the Schultz distribution fits, which models the Gaussian curve of the polymers distribution, the point-by-point fit simply takes the local maxima of all the individual monomer units along with the relative intensities to find the M_w , M_n , and PDI. (See Appendix 1) Most of the MALDI data at low molecular weights are hard to resolve because of overlapping MALDI signal from the matrix material [2, 30]. The complications due the matrix and other contaminants are mostly observed to affect the AAO grown polymerizations. For a given polymerization time, all AAO-grown polymers have a smaller molecular weight relative to the solution-grown polymers. They also possess a lower signal-to-noise ratio because of the much smaller amount of material present.

3.3.3 End group determination of AAO-grown PMMA

MALDI spectra of AAO-grown PMMA are clearly comprised of multiple molecular weight distributions of PMMA. Thus, with the exception of the data corresponding to 120 mins, the fits shown have two distributions for each of the respective times (t). The signal-

to-noise ratio in the $t=120$ min spectrum was too low to obtain and analyze a second distribution even though there is likely one present. The reason for the presence of multiple molecular weight distributions (and hence multiple spectra) in the AAO-grown polymer is associated with cleaving the AAO-grown PMMA from the substrate. While cleaving the polymer brush from the AAO matrix, several different cleavage mechanisms are possible. The cleavage of the Si-O could take place as SiO, SiO₂, or SiO₃, depending on where the actual Si-O bond breakage occurs. (Figure 3.8) The molecular weight of the initiator without taking in account any oxygen atoms attached to the silicon is 268 Da. Figure 3.8 shows the initiator with a single oxygen atom attached to the initiator, resulting in molecular weight of 284 Da. Because the molecular weight of the repeat unit, MMA, is 100.1 Da the value of every monomer unit will end approximately with the number “84”. Figure 3.9 shows the initiator with two oxygen atoms attached to the initiator. The resulting molecular weight would be 300 Da. Because the molecular weight of the repeat unit, MMA, is 100.1 Da the value of every monomer unit will end with the number “00”. Figure 3.10 shows another possibility that exists. HF could hydrolyze the ester bond located within the initiator itself. This type of a cleavage would leave a carboxylic acid group attached to every monomer with a molecular weight of 86 Da. Because the molecular weight of the repeat unit, MMA, is 100.1 Da the value of every monomer unit will end with the number “86”. The Schultz distribution and point-by-point models fit two sets of distributions for the pore grown polymerizations as well as a set for the single distribution found for the solution polymerization. The values of “84” and “00” were the numbers found at the end of each monomer unit in the MALDI spectra of the AAO grown PMMA. These values can be seen in the zoomed-in MALDI spectra shown in Figures 3.8 and 3.9.

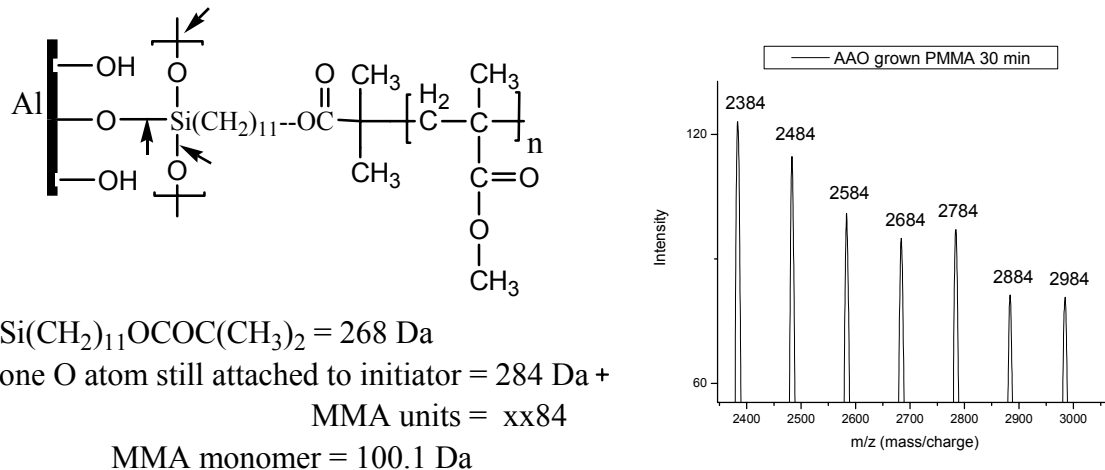


Figure 3.8 – (Left) Schematic showing the surface initiator plus MMA monomer attached to the AAO membrane. The black arrows denote the site at which bond cleavage takes place. (Right) Zoomed-in MALDI spectra of 30 min AAO polymerization. Each monomer unit is separated by 100 Da and has an end with the number “84”.

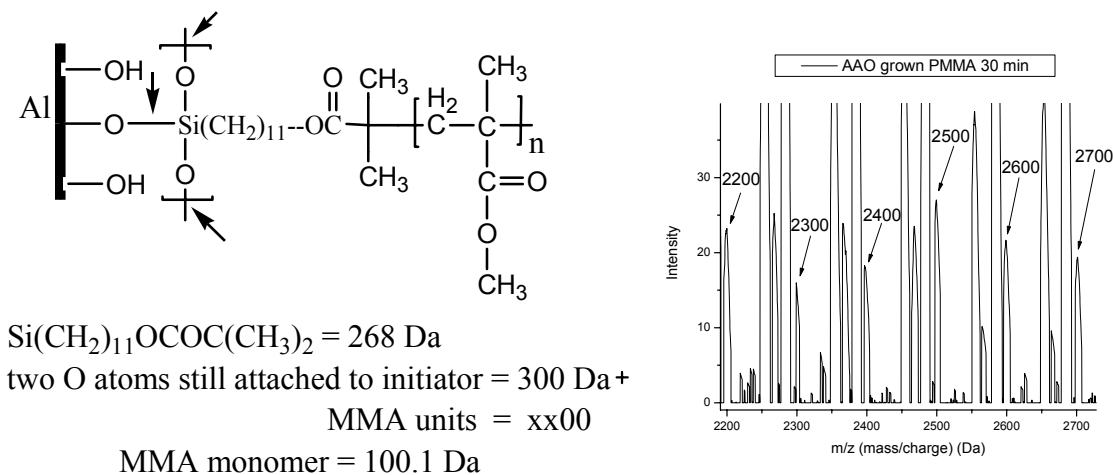
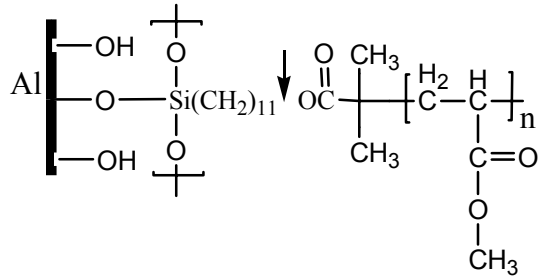


Figure 3.9 – Schematic showing the surface initiator plus MMA monomer attached to the AAO membrane. The black arrows denote the site at which bond cleavage takes place. (Right) Zoomed-in MALDI spectra of 30 min AAO polymerization. Each monomer unit is separated by 100 Da and has an end with the number “00”.



$\text{OCOC}(\text{CH}_3)_2 = 86 \text{ Da}$

MMA monomer = 100.1 Da

Figure 3.10 – Schematic showing the surface initiator plus MMA monomer attached to the AAO membrane. The black arrow denotes the site at which bond cleavage takes place.

3.3.4 Molecular weight analysis of MALDI spectra

The lack of a distinguishable lower molecular weight region affects the Schultz distribution and point-by-point fits. In the case of the Schultz distribution fit, the obscured lower molecular weight region tends to produce a fit with a higher polydispersity due to broadening of the Gaussian peak. The point-by-point fit is not affected in this way primarily because it only uses the data present thus giving a smaller polydispersity but higher number and weight average molecular weight. The reason for higher molecular weight values as fit by the point-by-point distribution relative to the Schultz distribution fit is because data points (<1500 Da) corresponding to smaller molecular weights were not included in the point-by-point distribution fit. While the lack of smaller data points because of matrix and other lower molecular weight contaminants affects the plots of both distribution fits, the method of fitting is different for the Schultz and point-by-point fits. The Schultz distribution yields M_n , M_w , and PDI based upon the curve generated. Thus, if the Gaussian peak is ill defined and broad, the PDI will be large. The point-by-point distribution yields M_n , M_w , and PDI based upon

the individual data points. Thus, because only higher maxima are included, the point-by-point distribution fit gives values with higher molecular weight.

The M_n values of the solution polymerization (top) and AAO-grown PMMA (bottom) as fitted by the Schultz distribution and point-by-point fit are plotted as a function of the polymerization time in Figures 3.11 through 3.14. The M_n values found for the solution polymerization by the Schultz distribution and point-by-point fit are fairly consistent. The one exception is the data obtained for the 30 minute long solution polymerization. The reason for the discrepancy in the 30-minute fits is the inability to assign the relative amounts of polymer in the lower molecular weight region of the Gaussian curve, which tends to shift the M_n fit to a higher value. The lack of a complete lower molecular weight region is also the reason for the slight difference in the 60 minute long polymerization fits. The difference is less noticeable in the 60-minute solution polymerization because the M_n value is shifted away from the region of high signal obtained from the matrix and other contaminants. Linear dependence of molecular weight on polymerization time and low PDI are the two key attributes of a well-controlled ATRP. The plot in Figure 3.16 is linear and the polydispersities of the solution grown PMMA are all less than 1.35 as seen in Table 3.1, indicating a well-controlled solution ATRP system.

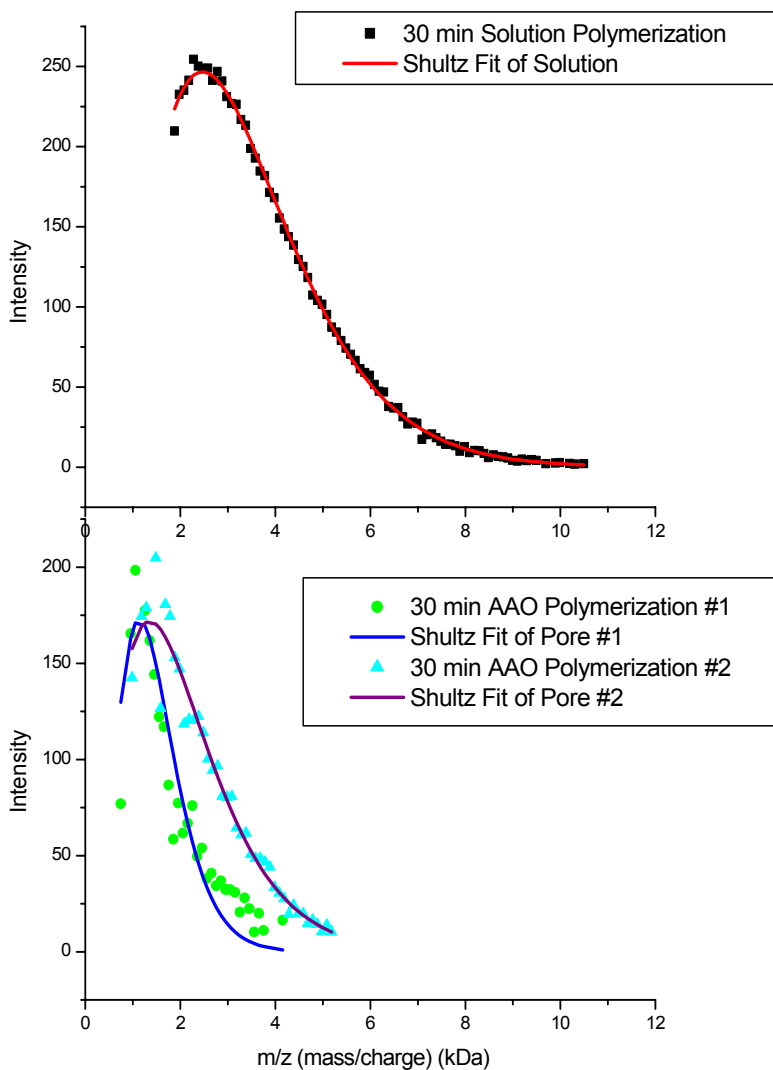


Figure 3.11 – Comparison of solution and pore grown (30min) poly(methyl methacrylate). The data is fit using a Schultz distribution and a point-by-point fit. The top plot shows the solution polymerization, while and the two AAO-grown distribution plots are shown in the plot split to the bottom. The black squares (■) in the top spectrum and the green circles (●) and blue triangles (▲) in the bottom spectrum indicate the local maxima for each monomer unit. The line indicating the Schultz distribution fit is shown as a red line (□) in for the solution polymerization, as a blue line (□) for the first AAO-polymerization distribution, and as a purple line (□) for the second AAO-polymerization distribution.

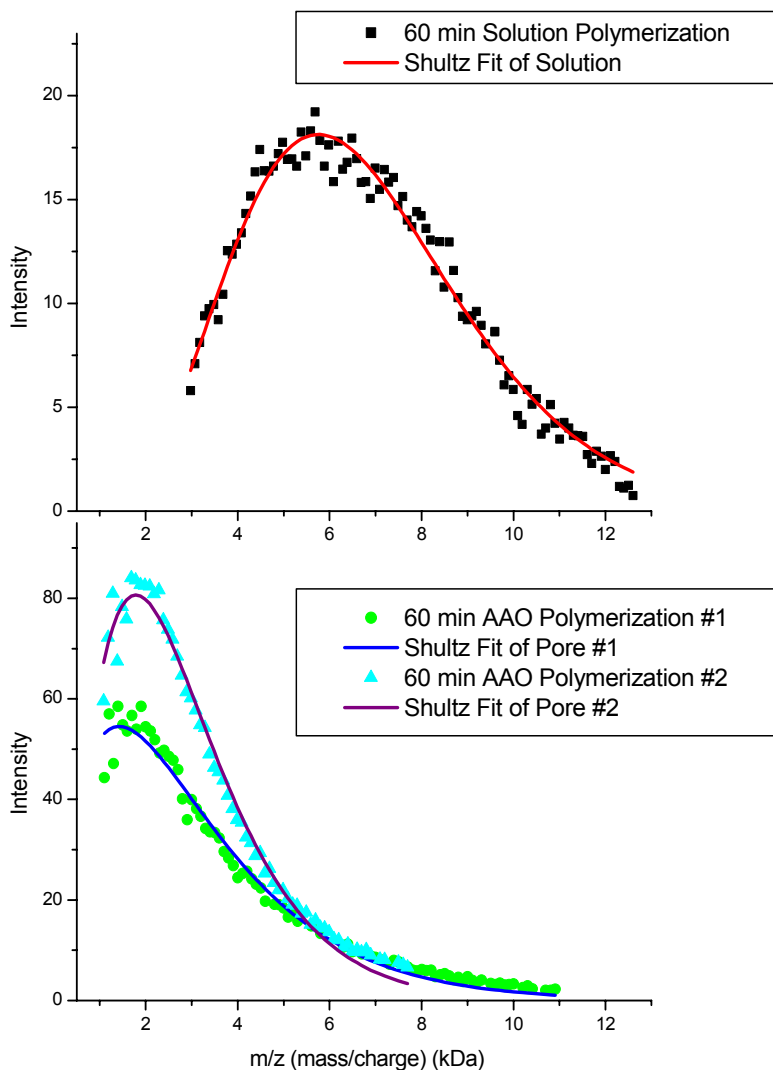


Figure 3.12 – Comparison of solution and pore grown (60min) poly(methyl methacrylate). The data is fit using a Schultz distribution and a point-by-point fit. The top plot shows the solution polymerization, while and the two AAO-grown distribution plots are shown in the plot split to the bottom. The black squares (■) in the top spectrum and the green circles (●) and blue triangles (▲) in the bottom spectrum indicate the local maxima for each monomer unit. The line indicating the Schultz distribution fit is shown as a red line (□) in for the solution polymerization, as a blue line (□) for the first AAO-polymerization distribution, and as a purple line (□) for the second AAO-polymerization distribution.

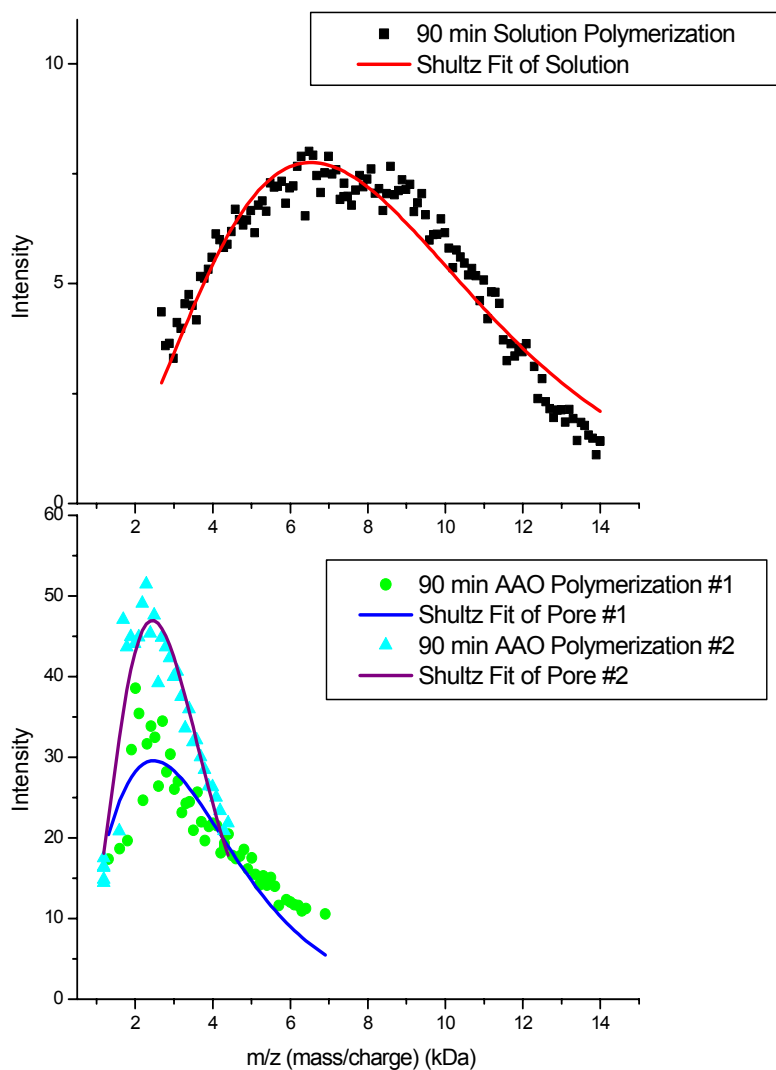


Figure 3.13 – Comparison of solution and pore grown (90min) poly(methyl methacrylate). The data is fit using a Schultz distribution and a point-by-point fit. The top plot shows the solution polymerization, while and the two AAO- grown distribution plots are shown in the plot split to the bottom. The black squares (■) in the top spectrum and the green circles (●) and blue triangles (▲) in the bottom spectrum indicate the local maxima for each monomer unit. The line indicating the Schultz distribution fit is shown as a red line (□) in for the solution polymerization, as a blue line (□) for the first AAO-polymerization distribution, and as a purple line (□) for the second AAO-polymerization distribution.

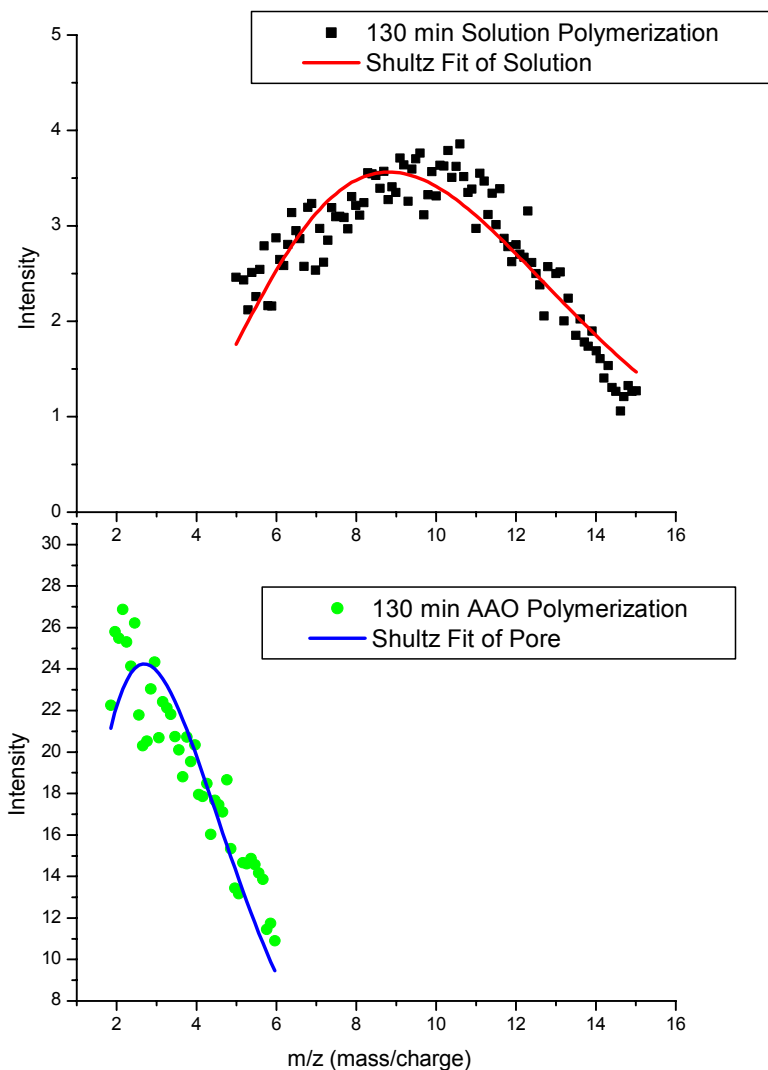


Figure 3.14 – Comparison of solution and pore grown (130min) poly(methyl methacrylate). The data is fit using a Schultz distribution and a point-by-point fit. The top plot shows the solution polymerization and the AAO- grown distribution plot is shown in the plot split to the bottom. The black squares (■) in the top spectrum and the green circles (●) in the bottom spectrum indicate the local maxima for each monomer unit. The line indicating the Schultz distribution fit is shown as a red line (□) in for the solution polymerization and as a blue line (□) for the first AAO-polymerization.

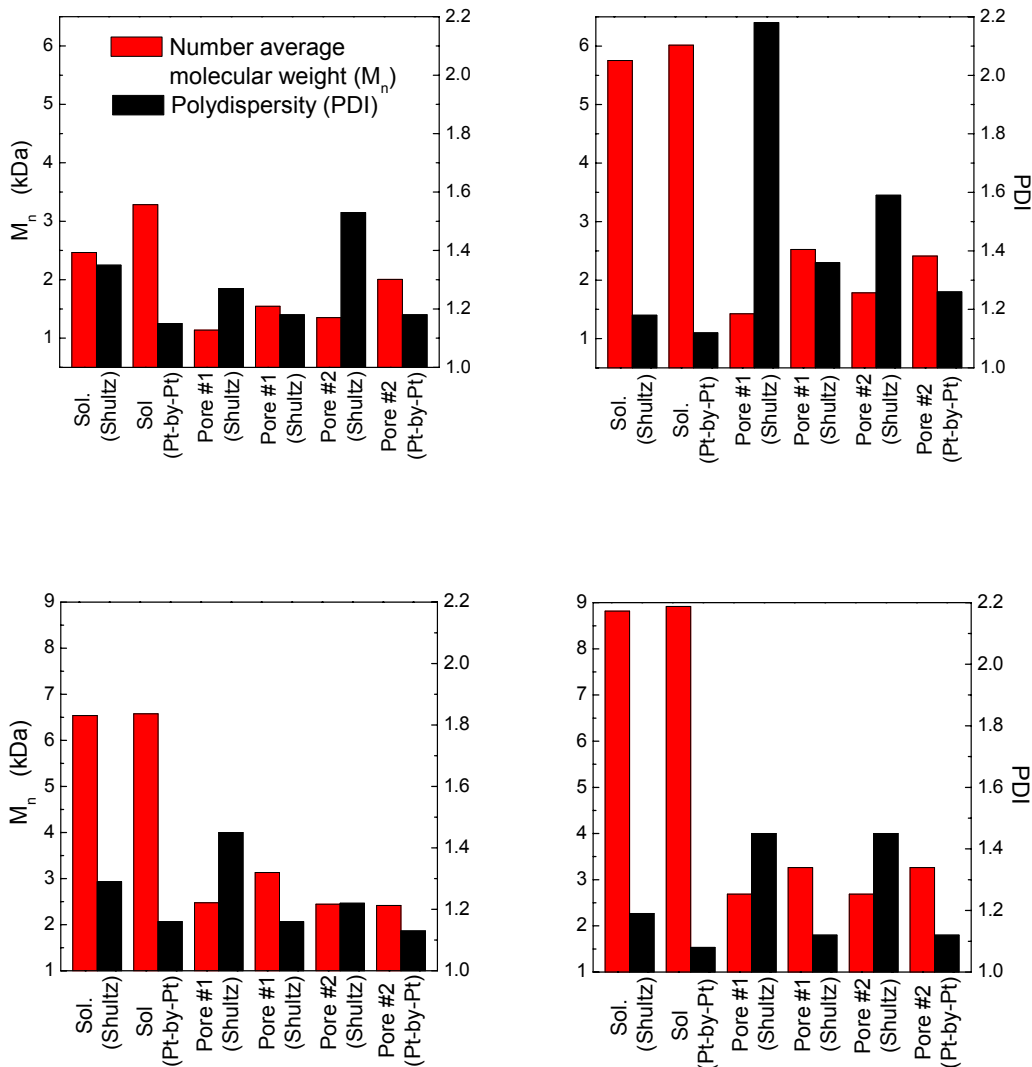


Figure 3.15 – Weight average molecular weight, number average molecular weight, and polydispersity values for grown poly(methyl methacrylate). The solution polymerization information is listed first (Schultz distribution fit followed by point-by-point fit) followed by the values obtained for both pore distributions (Schultz distribution fit followed by point-by-point fit). Both solution and AAO-grown PMMA was collected via conventional MALDI. The grown PMMA is shown in ascending order (30 (top left), 60 (top right), 90 (bottom left), 130 minutes (bottom right)). The red bar (■) indicates number average molecular weight (M_n). The black bar (■) indicates polydispersity (PDI).

Table 3.1 – Weight average molecular weight, number average molecular weight, and polydispersity values for grown poly(methyl methacrylate). The solution polymerization information is listed first, followed by the values obtained for the two AAO polymerization distributions. The values were found with a Schultz distribution and point-by-point (Pt-by-Pt) fit.

	Time	M _w (kDa)	M _n (kDa)	PDI
Solution Polymerization (Schultz distribution)	30	3.33	2.47	1.35
	60	6.79	5.76	1.18
	90	8.44	6.54	1.29
	130	10.51	8.82	1.19
Solution Polymerization (Pt-by-Pt Fit)	30	3.76	3.28	1.15
	60	6.72	6.02	1.12
	90	7.66	6.58	1.16
	130	9.63	8.92	1.08
AAO Polymerization #1 (Schultz distribution)	30	1.44	1.14	1.27
	60	3.10	1.42	2.18
	90	3.60	2.48	1.45
	130	3.89	2.69	1.45
AAO Polymerization #1 (Pt-by-Pt Fit)	30	1.83	1.55	1.18
	60	3.42	2.52	1.36
	90	3.64	3.13	1.16
	130	3.65	3.26	1.12
AAO Polymerization #2 (Schultz distribution)	30	2.07	1.35	1.53
	60	2.83	1.78	1.59
	90	2.98	2.44	1.22
	130	3.89	2.69	1.45
AAO Polymerization #2 (Pt-by-Pt Fit)	30	2.36	2.01	1.18
	60	3.04	2.41	1.26
	90	2.72	2.42	1.13
	130	3.65	3.26	1.12

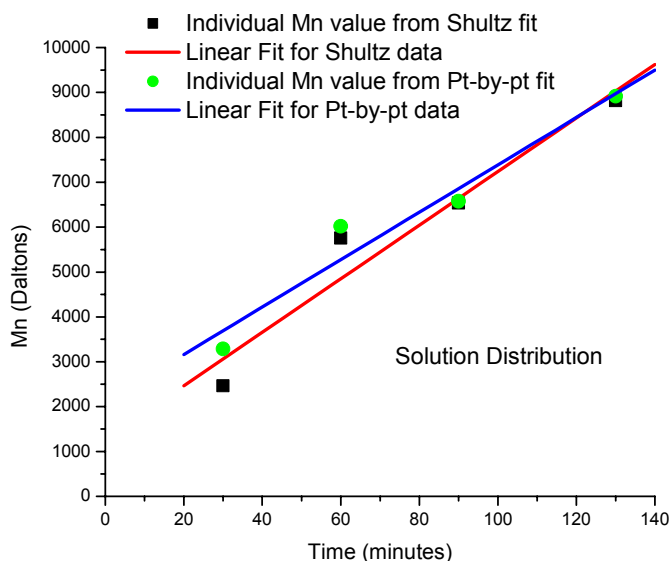


Figure 3.16 –The figure plots number average molecular weight (M_n) of solution grown polymer samples with the increasing polymerization time (30, 60, 90, and 130 min). The black square (■) indicates the M_n value as fit by the Schultz distribution model. The red line (□) indicates the linear fit of the Schultz distribution data. The filled green circles (●) indicate the M_n value as fit by the point-by-point analysis of the local maxima of each monomer unit. The blue line (□) indicates the linear fit of the (Pt-by-pt) data.

The M_n values of the first and second distribution of the AAO-grown polymers as fitted by the Schultz distribution and point-by-point fit are presented as a function of the polymerization time in Figures 3.11 through 3.14. The difference between the Schultz distribution fit and the point-by-point fit are very clear. The Schultz distribution fit yields a lower M_n value for every polymerization time. Once again, the reason for the difference is the lack of the clearly visible lower molecular weight region on the Gaussian curve, which shifts the M_n fit to a higher value. The only exception is the 90-minute time AAO-polymerization in the second distribution. In this case, a whole Gaussian curve could be established, thus the two models fit the data to about the same M_n value.

The difference between the solution and AAO-grown molecular weight distributions is that the AAO-grown PMMA has a much lower molecular weight at every polymerization time. Just as in the case of the p-Si substrate, the pore size of the AAO seems to be limiting the polymerization rate. The maximum number of monomer units observed in the polymerization of MMA in p-Si was about 25 (see Chapter 2) with the majority of the signal coming from less than 10 monomer units. While the AAO pore still limits the extent of polymerization of MMA, the maximum number of monomer units was around 150 (hence about 6 times larger relative to p-Si) and an analysis of M_n , M_w , and PDI could be performed.

While it appears from the data presented in Figures 3.17 and 3.18 that the molecular weight of AAO-grown PMMA increases linearly with time, as expected in a well-controlled ATRP reaction, more experiments need to be carried out to confirm this trend. The other essential element of a well-controlled ATRP system involves low PDI. Most of the PDI values for the AAO-grown PMMA are below 1.5. There is a large difference in the PDI found for the Schultz distribution fit versus those found for the point-by-point fit. The Schultz distribution fit values for PDI are always higher than the values obtained from the point-by-point fit. As mentioned earlier, the Schultz distribution fit is lacking the low molecular weight region and in some cases a clearly defined peak. Both of these factors lead to an ill-defined peak and a broad polydispersity. Still, even with these difficulties, the PDI is always <1.5 with the exception of the 60 minute polymerization in AAO (distribution #1). The PDI is large for that particular sample because a Gaussian peak is not clearly defined by

the individual data points. Because of the low signal to noise ratios, especially with regards to the AAO-grown polymerizations, a secondary means of characterization was sought.

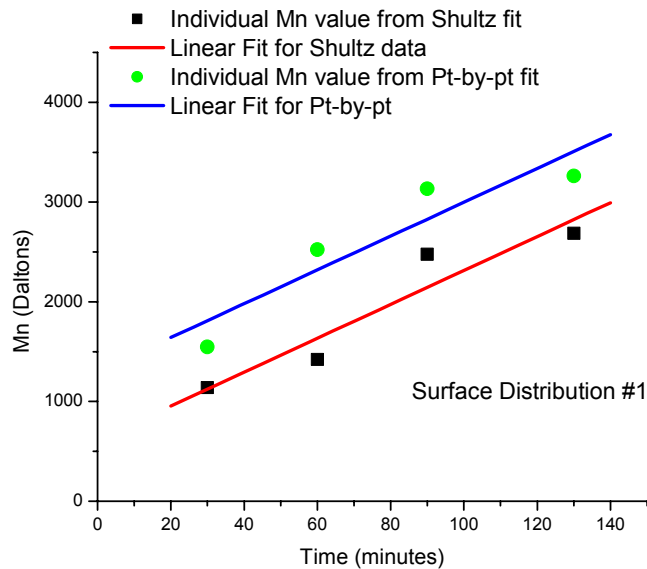


Figure 3.17 –The figure plots number average molecular weight (M_n of surface distribution #1) with increasing polymerization time (30, 60, 90, and 130 min). The black square (■) indicates the M_n value as fit by the Schultz distribution model. The red line (□) indicates the linear fit of the Schultz distribution data. The filled green circles (●) indicate the M_n value as fit by the point-by-point analysis of the local maxima of each monomer unit. The blue line (□) indicates the linear fit of the point-by-point data.

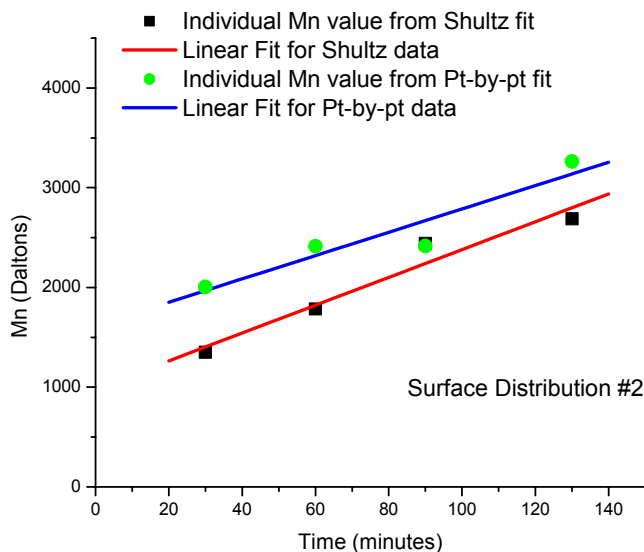


Figure 3.18 –The figure plots number average molecular weight (M_n of surface distribution #2) with increasing polymerization time (30, 60, 90, and 130 min). The black square (■) indicates the M_n value as fit by the Schultz distribution model. The red line (□) indicates the linear fit of the Schultz distribution data. The filled green circles (●) indicate the M_n value as fit by the point-by-point analysis of the local maxima of each monomer unit. The blue line (□) indicates the linear fit of the point-by-point data.

3.3.5 Gel Permeation Chromatography (GPC) of AAO-grown PMMA

The second technique used to characterize both the solution and pore grown PMMA was Gel Permeation Chromatography (GPC). Several problems occurred while trying to analyze the solution and pore grown PMMA with the GPC. As will be illustrated below, the primary problem was getting the solution and AAO-grown PMMA purified to get accurate chromatograms from the GPC. Examples of chromatograms of the AAO grown PMMA (90 minutes), solution grown PMMA (90 minutes), and a PMMA standard ($M_n = 3250$) are shown in Figure 3.19. The chromatogram of the AAO grown PMMA reveals the existence of two peaks, while the solution grown PMMA and the PMMA standard show only one peak

(as expected). Both the solution and the AAO grown PMMA eluted at much faster times than expected from the PMMA standards.

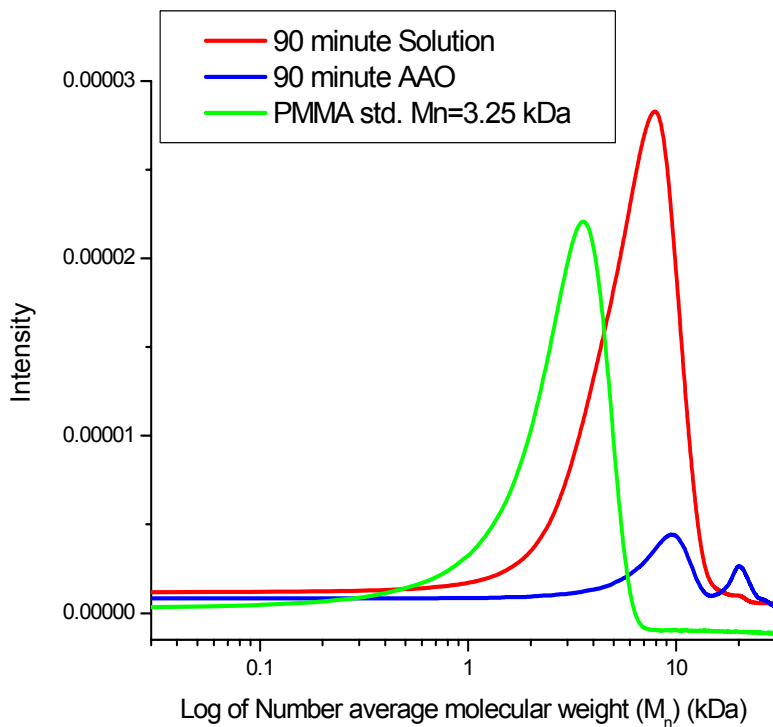


Figure 3.19 – Sample chromatogram for the 90-minute polymerization of PMMA in solution and in the AAO pores. A chromatogram of a 3.25 kDa PMMA standard is also shown. One peak was observed for the solution-grown PMMA and the PMMA standard. Two peaks were observed for the AAO-grown PMMA. A calibration curve of three PMMA standards was used to convert elution time (the standard x-axis for the chromatograms output) into a log 10 scale of number average molecular weight. The y-axis shows the intensity as collected by the refractive index detector.

For the case of the AAO-grown polymer, there is the possibility that the PMMA was incompletely cleaved from the AAO. If cleavage products were attached to the PMMA chains, their apparent molecular weight would be higher than expected. In fact, elution times from the GPC were always faster than expected elution time, consistent with this proposal. The AAO never fully dissolved in 10% aqueous HF solution based upon the appearance of partially dissolved AAO floating on the surface of the aqueous solution. After the addition of chloroform, the AAO was no longer visible, possibly scavenging the attached AAO into the organic phase. If the PMMA were not completely separated from the AAO then the AAO particles/PMMA would elute at a much faster rate due to the increased size of these AAO/PMMA aggregates compared to fully detached PMMA chains. As a result, the aggregated AAO/PMMA would produce exceptionally high and unrealistic molecular weights. The elution times of the AAO grown PMMA yielded number average molecular weights 3-4 times the size of the results produced by the MALDI.

For the case of the solution grown polymer, there is the possibility of copper salts not being completely removed from the PMMA resulting in a faster than expected elution time. Brittain and co-workers had previously reported on the difficulties of removing the copper salts used as catalysts for ATRP in the polymerization of MMA [31, 32]. A comparison of the number average molecular weight obtained for the solution polymerization via MALDI and GPC can be seen in Table 3.2. Table 3.2 illustrates the number average molecular weight results of the GPC analysis of the solution-grown PMMA are larger for every polymerization time.

Table 3.2 – The table shows the number average molecular weight for solution grown poly(methyl methacrylate) (PMMA). The Schultz distribution and point-by-point fit of the MALDI data is followed by the number average molecular weight obtained using a refractive index detector. A calibration curve was created with PMMA standards and used to determine the molecular weights in the GPC.

	M _n (kDa) MALDI (Schultz distribution Fit)	M _n (kDa) MALDI (Pt-by-Pt)	M _n (kDa) GPC
30 minutes	2.47	3.28	4.71
60 minutes	5.76	6.02	8.38
90 minutes	6.54	6.58	7.91
130 minutes	8.82	8.92	9.96

A plot of M_n of the five PMMA standards given by the manufacturer (GPC) versus M_n of the same five PMMA standards obtained via the MALDI for both the Schultz distribution and point-by-point method is shown in Figure 3.20. The GPC values provided by the manufacturer are consistently larger than those measured by the MALDI [33]. The M_n values determined by GPC for the solution polymerization and the MALDI data for the solution polymerization (Schultz distribution and point-by-point) are plotted in Figure 3.20 as well. The expectation was that the plot of the GPC vs. MALDI data for the solution polymerization would fall on correlation line created by the plot of the GPC vs. MALDI for the PMMA standards. The results of the GPC vs. MALDI plot of the solution polymerization shift the points off the fit line towards the GPC axis. While the high molecular weight samples fall close to the correlation line, there are significant deviations

observed for the low molecular weight specimens. Thus, the difference in the computed M_n provided by these two characterization techniques (GPC vs. MALDI) cannot be the only reason for higher than expected values from the GPC. The most likely reason for this deviation is the fact that ATRP-grown PMMA is not free of all the copper salts; salt aggregation with PMMA is causing the PMMA to move through the columns at a faster rate (hence appearing as having a higher molecular weight in the GPC experiment).

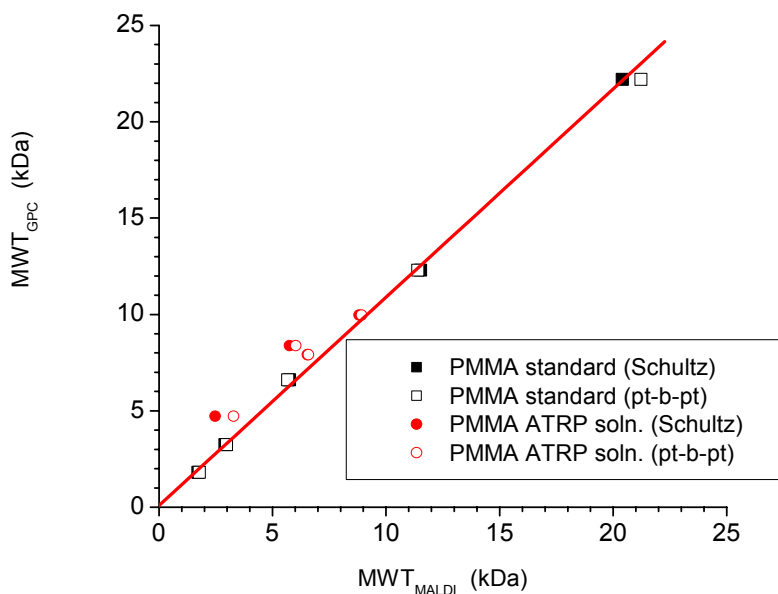


Figure 3.20 –The figure plots number average molecular weight given by the manufacturer (GPC) with the number average molecular weight found with MALDI. The filled black squares (■) indicate the M_n value of the PMMA standards as fit by the Schultz distribution model. The open black squares (□) indicate the M_n value of the PMMA standards as fit by the point-by-point analysis of the local maxima of each monomer unit. The filled red circles (●) indicate the M_n value of the solution grown PMMA as fit by the Schultz distribution model. The open red circles (○) indicate the M_n value of the solution grown PMMA as fit by the point-by-point analysis of the local maxima of each monomer unit. The red line (—) indicates the linear fit of the Schultz distribution and point-by-point data.

3.4 Conclusions

The use of Anodic Aluminum Oxide (AAO) as a substrate replacement for porous silicon produced polymers that increased linearly in molecular weight with increasing polymerization time. The homogeneous pore distribution of the AAO membrane yielded polymers with relatively low PDI and smaller molecular weights relative to the solution-polymerized MMA. We attribute the decrease of the AAO-grown PMMA molecular weight to the confinement effect as well as changes in the rate of polymerization inside the AAO pores relative to that in the free solution. Gel Permeation Chromatography was unsuccessful in directly corroborating the results of the molecular weight analysis obtained with the MALDI. We attribute the purification difficulties for the solution polymerization to copper salt aggregation with the PMMA. The AAO grown polymers could have the same problem with copper aggregation. In addition, the separation of the AAO from the PMMA grown in the PMMA would cause similar aggregation, causing erroneous GPC results. The characterization of the polymers grown in the confined geometries as well as the solution polymer was accomplished using ex situ MALDI analysis with a conventional matrix.

3.5 Experimental

Initiator attachment to Anodic Aluminum Oxide (AAO)

The first step was to attach initiator to the AAO membrane. The AAO membrane (0.2 μm , Whatman) was ultraviolet/ozone (UVO) cleaned for 20 minutes on each side. The (11-(2-Bromo-2-methyl)propionyloxy)undecyltrichlorosilane (BiB) (20 μL of 5% BiB in anhydrous toluene) was added to cold anhydrous toluene (20 mL, 99.8%, Sigma-Aldrich) containing the AAO wafer and placed in the freezer ($\approx 0^\circ\text{C}$) for at least 12 hours. The AAO-initiated wafers were rinsed with toluene (Reagent grade) and allowed to dry under a gentle stream of nitrogen. Careful consideration was given not to break the AAO membrane so an infrared spectrum could be collected. The AAO membrane was placed on a glass slide while being rinsed and dried. A transmission infrared spectrum was taken of the AAO membrane following this step as shown in Chapter 3.2.

Polymerization of PMMA in Anodic Aluminum Oxide

Following this, a single homogeneous solution containing all the components needed for the ATRP polymerization of PMMA was prepared. The actual breakdown of monomer/aqueous/solvent makeup for the polymerization was 34.9g of the methyl methacrylate (MMA, 99%, Alfa Aesar) monomer, 32.2g of methanol (Reagent Grade) (to solvate the monomer in water), and 7g of DI water. The polymerization system also contained 0.64g of Cu(I)Cl (99%, Aldrich) catalyst and 0.011 g of Cu(II)Cl₂ (99%, Aldrich) inhibitor. 2.06g of 2,2'-Dipyridyl (99%, Aldrich) was added as a ligand to complex with the copper compounds and keep the whole system homogenous. The solution was prepared

under a constant nitrogen stream in a 200ml two-neck round bottom flask to keep oxygen from penetrating the system. The polymerization solution was then removed with a syringe and placed in 20ml vials that contained a single AAO membrane functionalized with the BIB initiator. In addition, four vials were filled with polymerization media and 1 μ l of ethyl 2-bromoisobutyrate (98%, Aldrich) was added to initiate polymerization in solution to compare with the surface-initiated polymerizations. The solution was then bubbled briefly with nitrogen and tightly sealed. The polymerizations times were 30, 60, 90, and 130 minutes. At the end of each respective time, the polymerization solution was poured into a 200ml jar and filled with methanol (Reagent Grade, Aldrich) to precipitate the solution-grown polymer. The methanol/polymer media was exposed to oxygen for 30 minutes. This ensures that all the CuCl has been oxidized to CuCl₂ and the polymerization has been effectively stopped. The precipitated PMMA was placed in the freezer and allowed to settle. The solution was then decanted and dissolved in chloroform. The polymer was then run through several (2-3) pipets filled with activated alumina to remove the CuCl₂. Chloroform was used to elute the PMMA. A transmission infrared spectrum was taken of the solution grown PMMA by allowing the dissolved PMMA to evaporate on a UVO cleaned silicon wafer (N-type, Phosphorus doped, 1-5 ohm·cm, supplied by Silicon Valley Microelectronics, Inc.) following this step as shown in Chapter 3.2.

PMMA cleavage from Anodic Aluminum Oxide (AAO)

The PMMA modified AAO membranes were removed from the vial and washed with copious amounts of methanol. A transmission infrared spectrum was taken of the AAO membrane following this step as shown in Chapter 3.2. The PMMA modified AAO

membranes were then placed in a 200ml plastic container and a 10% aqueous HF (49% Reagent Grade from Fisher) solution was added. The sample was allowed to sit for a minimum of 30 minutes. At this point, 10 ml of chloroform was added and stirred to capture the PMMA chains in the organic phase. The chloroform was extracted with a syringe and placed in a small vial (5ml).

MALDI Analysis of Solution and AAO Grown PMMA

The chloroform/PMMA solution was prepared in a small 5ml vial. A 0.1M (in THF) solution of α -cyanohydroxycinnamic acid (99% Sigma-Aldrich) is prepared in a 1mL centrifuge tube. The PMMA was then mixed in a specific ratio. The ratio used varied from 3-5 to 1 (by volume) of α -cyanohydroxycinnamic to PMMA. An Applied Biosystems Voyager STR MALDI-TOF mass spectrometer was used for the molecular weight analysis. It was operated at an accelerating voltage of 20 kV in linear mode and positive ions were collected. Grid voltage was 90%. Laser intensity was adjusted to optimize signal. Generally, laser intensity between 1800-1900 proved sufficient. All settings are specific to the Applied Biosystems Voyager STR MALDI-TOF mass spectrometer.

Gel Permeation Chromatography (GPC) Analysis of Solution and AAO Grown PMMA

Both AAO and solution grown polymers were dissolved in chloroform (HPLC grade, Aldrich) and filtered through glass microfiber filters (Whatman 0.45 μ L pore size). Samples were placed in 1mL GPC vials and loaded into the autosampler with a bulk flow rate of 0.3 mL/min. Each autoinjection was 100 μ L. Three Waters Styragel HR columns were used in series—500 to 500,000 Da for column one, 50 to 100,000 Da for column two, and 500 to 30,000 Da for column three. A Wyatt $\text{\textcircled{R}}$ Optilab Rex differential refractometer was the

concentration detector and the unknown samples were compared to PMMA standards (MW = 1.8, 3.25, 6.8, and 12.3 kDaltons).

3.6 References

1. Trauger, S.A., et al., *High sensitivity and analyte capture with desorption/ionization mass spectrometry on silylated porous silicon*. Analytical Chemistry, 2004. **76**(15): p. 4484-4489.
2. Wei, J., J.M. Buriak, and G. Siuzdak, *Desorption-ionization mass spectrometry on porous silicon*. Nature, 1999. **399**(6733): p. 243-246.
3. Tinsley-Bown, A.M., et al., *Tuning the pore size and surface chemistry of porous silicon for immunoassays*. Physica Status Solidi a-Applied Research, 2000. **182**(1): p. 547-553.
4. Thomas, J.J., et al., *Desorption-ionization on silicon mass spectrometry: an application in forensics*. Analytica Chimica Acta, 2001. **442**(2): p. 183-190.
5. Shen, Z.X., et al., *A mass spectrometry plate reader: Monitoring enzyme activity and inhibition with a desorption/ionization on silicon (DIOS) platform*. Chembiochem, 2004. **5**(7): p. 921-927.
6. Xiong, S.X., Q. Wang, and H.S. Xia, *Preparation of polyaniline nanotubes array based on anodic aluminum oxide template*. Materials Research Bulletin, 2004. **39**(10): p. 1569-1580.
7. Jung, K.H., et al., *Fabrication of gold dot and tubular gold arrays using anodic aluminum oxide film as template*. Japanese Journal of Applied Physics Part 1-Regular Papers Brief Communications & Review Papers, 2005. **44**(7A): p. 5300-5303.
8. Zhang, Z.Y., et al., *Nanocompression and nanocharacterization research of anodic aluminum oxide film*. Rare Metal Materials and Engineering, 2005. **34**: p. 392-396.
9. Park, D.H., et al., *Synthesis and characterization of polythiophene and poly (3-methylthiophene) nanotubes and nanowires*. Synthetic Metals, 2005. **153**(1-3): p. 341-344.
10. Matyjaszewski, K., et al., *Polymers at interfaces: Using atom transfer radical polymerization in the controlled growth of homopolymers and block copolymers from silicon surfaces in the absence of untethered sacrificial initiator*. Macromolecules, 1999. **32**(26): p. 8716-8724.
11. Ejaz, M., et al., *Controlled graft polymerization of methyl methacrylate on silicon substrate by the combined use of the Langmuir-Blodgett and atom transfer radical polymerization techniques*. Macromolecules, 1998. **31**(17): p. 5934-5936.
12. Huang, X.Y. and M.J. Wirth, *Surface-initiated radical polymerization on porous silica*. Analytical Chemistry, 1997. **69**(22): p. 4577-4580.
13. Huang, X. and M.J. Wirth, *Surface initiation of living radical polymerization for growth of tethered chains of low polydispersity*. Macromolecules, 1999. **32**(5): p. 1694-1696.
14. Huang, W.X., et al., *Functionalization of surfaces by water-accelerated atom-transfer radical polymerization of hydroxyethyl methacrylate and subsequent derivatization*. Macromolecules, 2002. **35**(4): p. 1175-1179.
15. Jones, D.M. and W.T.S. Huck, *Controlled surface-initiated polymerizations in aqueous media*. Advanced Materials, 2001. **13**(16): p. 1256-1259.
16. Jones, D.M., A.A. Brown, and W.T.S. Huck, *Surface-initiated polymerizations in aqueous media: Effect of initiator density*. Langmuir, 2002. **18**(4): p. 1265-1269.

17. Kong, X.X., et al., *Amphiphilic polymer brushes grown from the silicon surface by atom transfer radical polymerization*. *Macromolecules*, 2001. **34**(6): p. 1837-1844.
18. Matyjaszewski, K., T.E. Patten, and J.H. Xia, *Controlled/"living" radical polymerization. Kinetics of the homogeneous atom transfer radical polymerization of styrene*. *Journal of the American Chemical Society*, 1997. **119**(4): p. 674-680.
19. Matyjaszewski, K. and J.H. Xia, *Atom transfer radical polymerization*. *Chemical Reviews*, 2001. **101**(9): p. 2921-2990.
20. Smith, P. and L. Goulet, *Effect of the Addition of Amine Diluents on the Physical-Properties of Poly(Methyl Methacrylate-Co-Methacrylic Acid) Copolymers Obtained by Partial Hydrolysis of Pmma*. *Journal of Polymer Science Part B-Polymer Physics*, 1993. **31**(3): p. 327-338.
21. Wang, Q. and X. Xu, *Structure and Properties of P(Mma-Maa) Peo Intermacromolecular Complex Formed through Hydrogen-Bonding*. *Science in China Series B-Chemistry*, 1991. **34**(12): p. 1409-1417.
22. Cottrell, J.S., M. Koerner, and R. Gerhards, *The characterization of synthetic polymers by matrix-assisted laser desorption/ionization mass spectrometry*. *Rapid Communications in Mass Spectrometry*, 1995. **9**(15): p. 1562-1564.
23. Koster, S., et al., *Endgroup determination of synthetic polymers by electrospray ionization Fourier transform ion cyclotron resonance mass spectrometry*. *Journal of the American Society for Mass Spectrometry*, 2000. **11**(6): p. 536-543.
24. Macha, S.F., P.A. Limbach, and P.J. Savickas, *Application of nonpolar matrices for the analysis of low molecular weight nonpolar synthetic polymers by matrix-assisted laser desorption/ionization time-of-flight mass spectrometry*. *Journal of the American Society for Mass Spectrometry*, 2000. **11**(8): p. 731-737.
25. Macha, S.F. and P.A. Limbach, *Matrix-assisted laser desorption/ionization (MALDI) mass spectrometry of polymers*. *Current Opinion in Solid State & Materials Science*, 2002. **6**(3): p. 213-220.
26. Montaudo, G., et al., *Characterization of Polymers by Matrix-Assisted Laser-Desorption Ionization Time-of-Flight Mass-Spectrometry - Molecular-Weight Estimates in Samples of Varying Polydispersity*. *Rapid Communications in Mass Spectrometry*, 1995. **9**(5): p. 453-460.
27. Murgasova, R. and D.M. Hercules, *MALDI of synthetic polymers - an update*. *International Journal of Mass Spectrometry*, 2003. **226**(1): p. 151-162.
28. Yalcin, T., Y.Q. Dai, and L. Li, *Matrix-assisted laser desorption/ionization time-of-flight mass spectrometry for polymer analysis: Solvent effect in sample preparation*. *Journal of the American Society for Mass Spectrometry*, 1998. **9**(12): p. 1303-1310.
29. Zimm, B.H., *Apparatus and Methods for Measurement and Interpretation of the Angular Variation of Light Scattering - Preliminary Results on Polystyrene Solutions*. *Journal of Chemical Physics*, 1948. **16**(12): p. 1099-1116.
30. Nielen, M.W.F., *Maldi time-of-flight mass spectrometry of synthetic polymers*. *Mass Spectrometry Reviews*, 1999. **18**(5): p. 309-344.
31. Liou, S., et al., *Atom transfer radical polymerization of methyl methacrylate with polyethylene-functionalized ligands*. *Macromolecules*, 2000. **33**(12): p. 4295-4296.
32. Honigfort, M.E. and W.J. Brittain, *Use of JandaJel resins for copper removal in atom transfer radical polymerization*. *Macromolecules*, 2003. **36**(9): p. 3111-3114.

33. Jackson, C., B. Larsen, and C. McEwen, *Comparison of most probable peak values as measured for polymer distributions by MALDI mass spectrometry and by size exclusion chromatography*. *Analytical Chemistry*, 1996. **68**(8): p. 1303-1308.
34. Peebles, L.H. *Molecular Weight Distribution in Polymers*; Wiley-Interscience: New York, 1971.
35. Schultz, G.V.Z. *Phys. Chem.* 1939, B43, 25.

Chapter 4: Fast Directed Motion of “Fakir” Droplets

4.1 Introduction

Practical studies of liquid movement across substrates have enhanced our understanding of several academic and industrial fields such as microfluidics, biosensors and drug delivery. Controlling wetting properties and topography of surfaces can facilitate faster and more efficient ways of moving liquids. Specifically, altering these parameters can affect the speed and mechanism by which the droplet travels on a substrate [1-13]. A liquid droplet placed on a surface bearing a spatial chemical heterogeneity can traverse in the direction of the lower contact angle because of the imbalance of surface energies acting on various parts of the droplet and the tendency of the droplet to establish a new equilibrium. Chaudhury and Whitesides demonstrated this concept of controlled drop motion driven by variable wettability originating from the substrate. They showed that a liquid drop can move along a wettability gradient and in some circumstances can even climb up an inclined plane [1]. In their seminal paper, Chaudhury and Whitesides also recognized the importance of contact angle hysteresis, *i.e.*, the difference between the advancing and receding contact angles, on the drop motion. Specifically, they identified that liquid movement occurs when the receding contact angle of the back (receding) edge of the drop is larger than the advancing contact angle of the front (advancing) edge of the drop. However, contact angle hysteresis will serve to reduce the difference between the advancing and receding edge of the drop, therefore possibly slowing or halting drop motion. To overcome the latter problem, Daniel and Chaudhury used an external force by supplementing the chemical gradient driving force with an in-plane vibration of the drop [2]. They demonstrated that substrate vibration helped to

overcome the relatively large contact angle hysteresis ($\approx 20^\circ$) thus increasing the drop velocity up to ≈ 5 times.

Recently, Daniel and coworkers provided more insight about the various molecular parameters that influence the motion of liquid drops on chemically heterogeneous surfaces [3]. They argued that the drop velocity (v) is related to the surface tension of the liquid (γ), the radius of the droplet on the surface (R), and the position-dependent change of wettability [2-4]:

$$v \cong \frac{\gamma R}{\eta_s} \frac{d \cos(\theta)}{dx} \quad (1)$$

In Equation (1) θ is the contact angle of the liquid with the substrate and η_s represents a viscosity parameter that denotes the friction at the liquid/solid interface [4]. Defining the capillary number as $Ca = v/v^* = v\eta/\gamma$, where v^* equals the surface tension (γ) divided by the liquid bulk viscosity (η), Equation (1) can be rewritten as:

$$Ca = K \cdot R \frac{d \cos(\theta)}{dx} = K \cdot R^* \quad (2)$$

where the coefficient K accounts for the corrections to η due to the frictional forces at the liquid/solid interface, and $R^* = R \frac{d \cos(\theta)}{dx}$. Daniel and coworkers demonstrated the general validity of Equation (2) by studying the motion of droplets of various liquids on surfaces covered with a molecular gradient made of self-assembled monolayer of $H_3C(CH_2)_9SiCl_3$ (H10-SAM) prepared on flat silica-covered substrates. Data of Ca vs. R^* from 4 different liquids had approximately identical slopes, indicating that K was very similar in all cases

studied and was presumably dictated primarily by the surface energy of the substrate. They also established the effect of the contact angle hysteresis on the droplet motion. Daniel and coworkers showed that in the Ca vs. R^* plot the hysteresis appeared to cause only a change in the intercept in the data but not the slope. By utilizing this approach, the researchers were able to visually separate the effect of friction and contact angle hysteresis on drop motion. Specifically, the findings of Daniel and coworkers indicate that, regardless of the hysteresis, the velocity of the droplet will increase (hence the slope in the Ca vs. R^* plot increases) when the friction at the liquid/solid interface decreases.

From this perspective, one can reason that higher drop velocities can be achieved by lowering the frictional forces experienced by the drop as it traverses the gradient. This concept contrasts with the earlier focus [2] on overcoming hysteresis to maximize the velocity of the drop. Because of low surface energy and low friction of fluorine moieties, liquid droplets moving along surfaces comprising variable density of fluorinated groups should move faster, relative to the motion of a droplet moving on an analogous hydrocarbon surface. Moreover, the friction may be further decreased at the liquid/solid interface by utilizing substrates with small pores that cannot be wet by a moving liquid. Quéré and Bico have shown that wettability at the liquid/solid interface can be lowered if air is trapped below the liquid in the holes of the rough surface. In such a situation, the liquid positions itself on the surface in a similar fashion as an Indian “fakir” lying on the points of a bed of sharp nails [16-18]. The contact angle (θ^*) of a “fakir” droplet residing on such physically rough substrates is given by [16]:

$$\cos(\theta^*) = -1 + \phi_s (\cos(\theta) + 1) \quad , \quad (3)$$

where ϕ_s is the fraction of the liquid/solid interface below the drop. Such a situation should facilitate a decrease in the friction and a corresponding increase in velocity of the droplet because of the decreased contact area at the liquid/solid interface.

In this Letter we utilize the above two concepts in facilitating fast motion of water droplets across a surface-bound wettability gradient. First, we measure the velocity of water droplets on molecular gradients made of semifluorinated SAMs on flat silica substrates and show that these are higher than the velocities observed by Daniel and coworkers on H10-SAM substrates. Next we demonstrate that further increase in drop velocity can be achieved by advancing water droplets along substrates comprising wettability gradients of semifluorinated SAMs that reside on top of porous substrates. Using a simple scaling model we demonstrate that the significant increase in the drop velocity on the porous substrates, relative to the motion on flat silica, correlates with the substrate porosity and hence reduced contact area at the solid/liquid interface.

4.2 Results and Discussion

4.2.1 Characterization of semifluorinated wettability gradient

Wettability gradients of semifluorinated molecules of heptadecafluoro-1,1,2,2-Tetrahydrodecyl trichlorosilane (F8H2) were prepared on flat and porous silica substrates using the procedure outlined in the experimental section. Porous silica substrates were prepared by an electrochemical etch (for details see the experimental section) and imaged using scanning electron microscopy. Figure 4.1 (left) highlights the cross-sectional morphology of the porous silica substrate. The spatial variation of fluorine concentration

(Figure 4.1 (right)) in the porous silicon specimen was established using combinatorial near-edge X-ray absorption fine structure (NEXAFS) spectroscopy [19]. The results of the combinatorial NEXAFS experiments confirm that the surface is decorated with F8H2 molecules whose grafting density varies gradually across the sample. Moreover, the NEXAFS data reveal that the relative density of fluorine is higher in the porous region indicated by the elevated circle in the specimen. In contrast, the unetched area surrounding the porous medium reveals a lower concentration of F8H2. This result reflects the greater surface area within the porous region and indicates that the surfaces of the pores are (at least partially) filled with the F8H2 molecules.

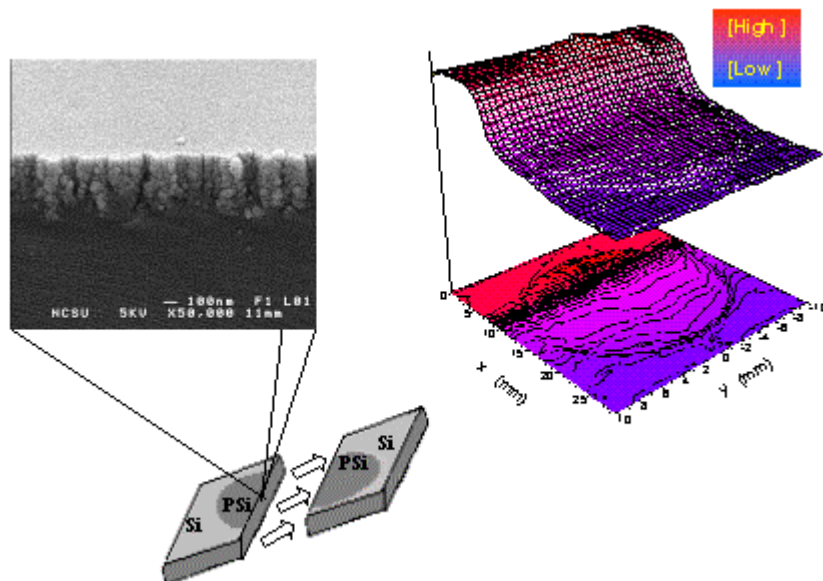


Figure 4.1 - (Left) Cross sectional scanning electron microscopy image of porous silicon. The diagram depicts the outline of the porous region after etching. (Right) Relative fluorine concentration on the porous substrate decorated with the gradient in F8H2 self-assembled monolayer as determined from the combinatorial near-edge x-ray absorption fine structure spectroscopy experiments.

4.2.2 Contact angle hysteresis

Given the previous emphasis on contact angle hysteresis, a comparison of the wettability of both the flat and porous surface was established using contact angle measurements. In Figure 4.2 we plot the advancing (θ_a) and receding (θ_r) contact angles of deionized water on both the flat and porous gradient surface. These angles were determined with the aid of imaging software from dynamic water contact angles measured at various positions along the substrate during droplet motion. These values were utilized to quantify contact angle hysteresis (CAH). In this work, CAH is defined as $(\cos \theta_a - \cos \theta_r)$. The experimental values for CAH averaged across the substrate are 0.44 (± 0.025) and 0.58

(± 0.023) for the flat and porous substrates, respectively. Thus, the CAH is slightly higher on the porous substrate than on the flat substrate. This fortuitous behavior allows us to determine whether friction or CAH is most important in governing drop velocity across the gradient.

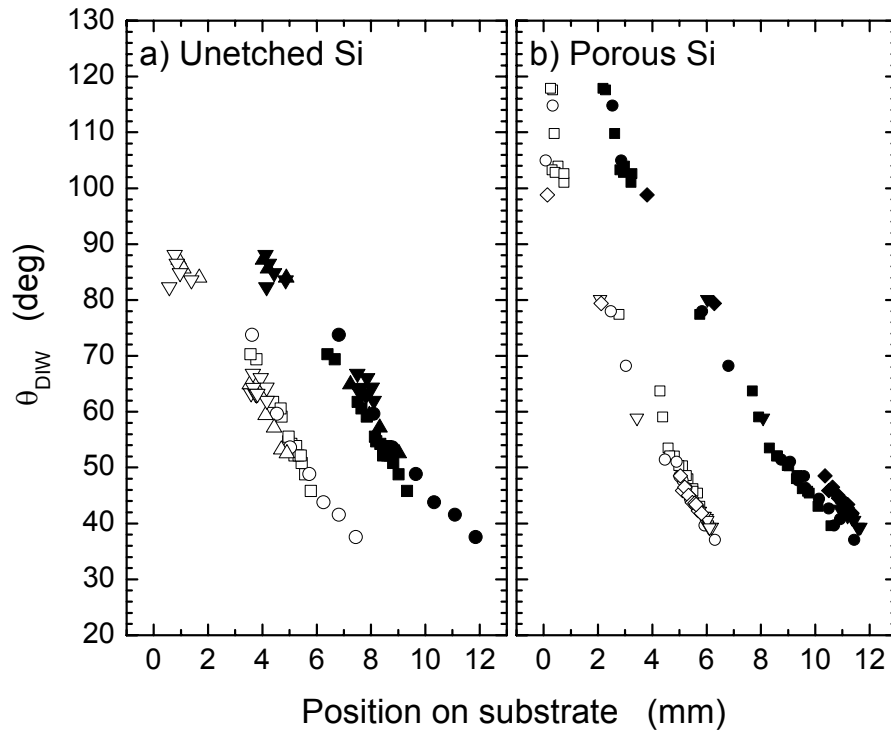


Figure 4.2 - Advancing (solid symbols) and receding (open symbols) contact angles of deionized water as a function of the position on the F8H2 molecular gradient created on top of a flat (a) and porous (b) silicon substrate. The volume of the probing liquid was 4 (■), 6 (●), 8 (▲), 10 (▼), and 12 (◆) μ l.

4.2.3 *Velocities of drops moving on flat and porous substrates decorated with semifluorinated wettability gradients*

Because v^* ($=\gamma/\eta$) is the same in all our experiments, the slope of the Ca ($=v/v^*$) vs. R^* plot provides a direct measure of the drop velocity. These slopes can be assessed from Figure 3, which shows the dependence of the capillary number on R^* for water droplets of various volumes (4 -12 μL) moving across flat (open symbols) and porous (solid symbols) substrates covered with the F8H2-SAM gradient. First, we compare the velocities of water droplets moving on flat substrates decorated with F8H2 gradients to those of the analogous hydrocarbon gradient [3]. The slopes in the Ca vs. R^* plots are ≈ 0.015 and ≈ 0.007 for the F8H2 specimen and the hydrocarbon gradient, respectively, revealing the velocity of water drop is approximately twice as high as the F8H2 substrate relative to that on the H10 gradient. Next, we use the same analysis to determine how incorporating porosity into the substrate affects the drop velocity. The data in Figure 3 reveals that water droplets move faster along the F8H2 gradient created on the porous substrate relative to the F8H2 gradient on flat silica. The graph of Ca vs. R^* shows that the slope corresponding to the motion on the porous substrate is ≈ 0.035 . This is ≈ 2.3 times faster than the motion on the flat substrate covered with the same F8H2 molecular gradient.

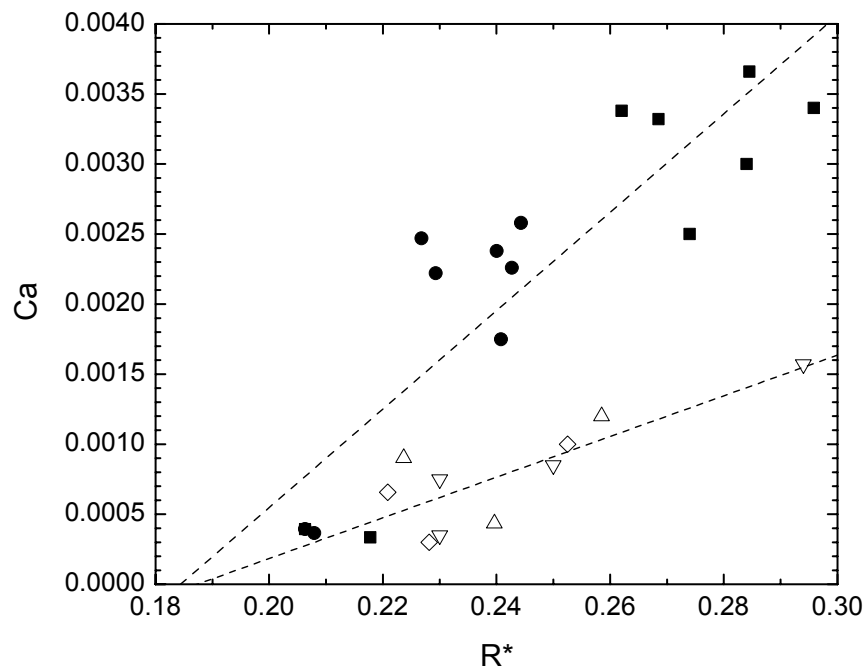


Figure 4.3 - Capillary number ($Ca=v/v^*$) as a function of the normalized drop radius ($R^*=R\partial\cos(\theta)/\partial x$) associated with motion of a droplet of deionized water along the F8H2 molecular gradient created on top of a flat (open symbols) and porous (solid symbols) silicon substrate. During the course of the experiment the drop velocity was collected at multiple positions on the sample. The data presented in Figure 3 have been compiled from the drop velocity data collected at the constant contact angle of water equal to: 70° (∇), 65° (Δ), 60° (\square), 100° (\blacksquare), and 80° (\bullet). The lines are meant to guide the eye.

If lower CAH were the primary force responsible for faster drop motion, one would expect that the CAH of the porous substrate were lower than that of the flat substrate. As discussed earlier, Daniel and coworkers infer the effect of CAH on the drop motion from the R^* intercept in the Ca . vs. R^* plot. From Figure 4.3, the close proximity of the R^* intercept for the data collected on porous and flat substrates reveals that the CAH is approximately the same in both cases. This observation is in accord with our earlier conclusion, namely that the

CAH on the porous substrate is similar to or slightly larger than that on the flat substrate (*cf.* Figure 4.2). Hence, the rapid increase of the drop velocity on the porous substrate relative to that on the flat surface must originate from a different effect, namely the reduced frictional forces at the liquid/substrate interface (*cf.* Equation 2).

4.3 Conclusions

Although there are some controversies regarding the friction of fluorinated surfaces [14-15], self-assembled monolayers made of fluorine-containing species are believed to provide surfaces with lower surface energy and lower friction. Our results seem to confirm the notion that the F8H2 surfaces possess lower friction and thus facilitate higher speeds of water droplets. Reduced friction at the liquid/substrate interface is also responsible for the observed faster motion of water droplets on porous substrates, relative to flat surfaces. Using the water contact angle on a homogeneous F8H2-SAM on the flat substrate ($\theta = 102^\circ$) and the corresponding contact angle of a F8H2-SAM on the rough substrate ($\theta^* = 125^\circ$), the fraction of the liquid/substrate interface below the drop (ϕ_s) is ≈ 0.5 (*cf.* Equation 3). Based on the work of Beake and Leggett, who established that the frictional forces on substrates made of mixed self-assembled monolayers scaled approximately linearly with the cosine of the contact angle [20], we expect that the frictional forces between the drop and the textured substrate will reduce $\approx 1/\phi_s$ times [21]. Hence, the slope in the Ca vs. R^* plot for motion on the rough substrate should be about twice of that on the flat substrate. From the data in Figure 4.3, the slopes are 0.035 and 0.015 for the rough and flat substrates, respectively, which gives a ratio of ≈ 2.3 , in reasonable agreement with the predicted value of ≈ 2 ($1/\phi_s$).

In spite of the simplicity of this scaling model (for convenience, we have neglected any additional contributions to the friction, such as the line tension at the air/liquid/solid interface), our analysis strongly suggests that the decreased contact area between the liquid and the porous substrate leads to the decreased frictional forces between the droplet and the substrate and results in the faster motion of droplets on the rough substrates relative to that on flat specimens. Combining chemical gradients with surface roughness offers a powerful method for controlling the movement of liquids on surfaces. For example, applications of rough surfaces for liquid movement may facilitate enhanced liquid removal capabilities. Advancements have been made in applying a thin non-wettable coating on windshields to remove rain droplets on vehicles, aircrafts, and virtually any glass surface. By tailoring the porosity of the glass this could in turn remove moisture droplets and contaminants at a faster pace and with greater efficiency. More in depth studies are underway to better understand the mechanism of motion for rough substrates.

4.4 Experimental

Preparation of Porous Silicon

The porous silicon substrate was created by electrochemical etching a n-type silicon wafer (Sb-doped, 0.01-0.02 ohm·cm) in a Teflon cell, whose configuration was similar to the cell used by Siuzdak et al [22]. The etching solution was a 1:1 (by volume) mixture of concentrated HF (49% Reagent Grade from Fisher) and absolute ethanol (100%, Fisher). The cell compartment that contains the silicon and the etching solution is illuminated with 50mW/cm² of white light from a fiber optic light source (Model I-150, Coherent, Inc.). While illuminated, about 4.6 mA/cm² of constant current is passed through the cell chamber for one minute. After the etching process, the porous silicon sample is washed with absolute ethanol and dried under a nitrogen stream.

Preparation of F8H2 Gradient on Porous and Flat Surface

Our method closely follows that suggested by Chaudhury and Whitesides [1]. First, the substrate (porous or flat) was treated in an ultraviolet/ozone (UVO) chamber (Model 42, Jelight Company, Inc) for 20 minutes in order to generate a large number of the surface-bound hydroxyl groups necessary for the attachment of the semifluorinated organosilane molecules. A mixture of heptadecafluoro-1,1,2,2-Tetrahydrodecyl trichlorosilane (95%, F8H2, Gelest, Inc.) and paraffin oil (1:3 w/w) was placed in a small container, which was positioned near the edge of the UVO-treated silicon substrate. During the gradient formation, the system was maintained in an enclosed chamber with controlled temperature (22-24°C) and humidity (40-50%). As the F8H2 molecules evaporated, they diffused in the vapor and generated a concentration gradient, which was then imprinted onto the substrate.

After 2-3 minutes, the sample was removed from the chamber, thoroughly washed with ethanol and dried with a stream of with nitrogen.

Characterization of the porous silicon surface

Combinatorial near-edge x-ray absorption fine structure (NEXAFS) spectroscopy measurements provided information about the spatial concentration of fluorine on the porous substrate [18]. The experiments were performed at the National Synchrotron Light Source at Brookhaven National Laboratory. The samples were placed onto a four-degree of freedom goniometer, which allowed X-Y in-plane scanning of the sample in the soft x-ray beam. The partial electron yield (PEY) signal originating from the specimen was collected as a function the X and Y coordinates at the fixed angle between the sample surface and the electric vector of the x-ray beam ($=55^\circ$) at the three different energies of the x-rays: 680 eV (K pre-edge of fluorine), 692 eV ($1s \rightarrow \sigma^*_{C-F}$), and 720 eV (K post-edge of fluorine). The plot in Figure 1b was generated by standard normalization of the PEY data using the pre-, post-edge, and the $1s \rightarrow \sigma^*_{C-F}$ data [19].

The morphology of the porous silicon specimens was probed using a scanning electron microscope (SEM, model Hitachi S-3200). Prior to the SEM experiment, the sample was sputter-coated with gold.

Measurement of contact angles and drop velocity

Drop movement was recorded using a CCD camera interfaced with a PC mounted perpendicular to a Rame-Hart 1000 goniometer stand. This CCD allowed for the recording of the drop motion in situ as the liquid was placed by a microsyringe on the gradient

substrate. Measurements were then taken for the dynamic contact angle of the droplet on the substrate surface via Scion image software. The drawback of the aforementioned CCD camera is that it was relatively slow speed and only had the ability to capture about 15 frames per second. The slow speed of the CCD camera resulted in the estimation of the position of the drop and thus created relatively wide scatter of the velocity data in the v/v^* vs. R^* plot.

4.4 References

- 1) Chaudhury, M.K.; Whitesides, G.M. *Science* **1992**, *256*, 1539.
- 2) Daniel, S.; Chaudhury, M.K. *Langmuir* **2002**, *18*, 3404.
- 3) Daniel, S.; Sircar, S.; Gliem, J.; Chaudhury, M.K. *Langmuir* **2004**, *20*, 4085.
- 4) Greenspan, H.P. *J. Fluid Mech.* **1978**, *84*, 125.
- 5) Ondarcuhu, T.; Veyssie, M. *J. Phys. (Paris) II* **1988**, *1*, 75.
- 6) Brochard, F. *Langmuir* **1989**, *5*, 432.
- 7) Domingues Dos Santos, F.; Ondarcuhu, T. *Phys. Rev. Lett.* **1995**, *75*, 2972.
- 8) Ichimura, K.; Oh, S.-K.; Nakagawa, M. *Science* **2000**, *288*, 1624.
- 9) Daniel, S.; Chaudhury, M.K.; Chen, J.C. *Science* **2001**, *291*, 633.
- 10) Lee, S.-W.; Laibinis, P.E.; *J. Am. Chem. Soc.* **2000**, *122*, 5395.
- 11) Suda, H.; Yamada, S. *Langmuir* **2003**, *19*, 529.
- 12) Choi, S.-H.; Zhang-Newby, B-m. *Langmuir* **2003**, *19*, 7427.
- 13) Bain, C. *ChemPhysChem* **2001**, *2*, 580.
- 14) Perry, S.S.; Lee, T.R. *Langmuir* **1999**, *15*, 3179.
- 15) DePalma, V.; Tillman, N. *Langmuir* **1989**, *5*, 868.
- 16) Bico, J.; Thiele, U.; Quéré, D. *Coll. Surf. A* **2002**, *206*, 41.
- 17) Quéré, D.; Lafuma, A.; Bico, J. *Nanotechnology* **2003**, *14*, 1109.
- 18) Quéré, D. *Nature Materials* **2002**, *1*, 14.

19) Genzer J.; Fischer D. A.; Efimenko K. *App. Phys. Lett.* **2003** 82, 266

20) Beake, B.D.; Leggett, G.J. *Phys. Chem. Chem. Phys.* **1990**, 1, 3345.

21) Here we neglect any additional contributions to the friction arising from the line tension.

22) Shen, Z.; Thomas, J. J.; Averbuj, C.; Broo, K. M.; Engelhard, M.; Crowell, J. E.; Finn, M.G.; Siuzdak, G. *Anal. Chem.* **2001**, 73, 612.

Chapter 5: Outlook

The principal goal of this PhD thesis was centered around nanometer-sized pores: 1) investigating the confinement effect on surface-initiated polymerization in the pore and 2) utilizing porous materials as novel substrates for motion of liquid droplets along surface wettability gradients. The confinement effect of the pore on an ATRP polymerization was explored using porous silicon (p-Si) and anodic aluminum oxide (AAO). The confinement effect of the small pore of both p-Si and AAO down slow the rate of polymerization relative to a bulk solution polymerization. We hypothesize that the rate and extent of growth is limited by the restricted rate of diffusion of the monomer and the catalyst into the pore, wetting of pore walls with solvent and the overall confinement of the pore size on the polymer growth due to polymer crowding. Nanometer-sized pores were also used as the platform, on which wettability gradients were formed. We showed that a higher drop velocity was achieved using the wettability gradient on porous silicon relative to the wettability gradients formed on flat silicon substrates.

5.1 SEM study of porous silicon

In chapter 2 we studied p-Si as a substrate for the direct molecular weight characterization of surface initiated polymer chain. The size of the pore and overall porosity of the silicon substrate have a direct affect on the signal obtained in MS-desorption ionization on silicon DIOS. A detailed study of pore size and its effect on the MS-DIOS signal was not undertaken and clear relationship has not been presented in the literature. A scanning electron microscopy (SEM) study detailing the change in pore size through the variation of etching conditions (etch time, current, and white light intensity) could allow for larger pore

sizes to be created that are MS-DIOS active. In situ molecular weight characterization of much larger surface pore-grown polymers could be possible if the pores are large enough and MS-DIOS yields a quality signal. Also in chapter 2 reactive ion etching (RIE) was explored briefly as a method to create homogeneous porous silicon. An SEM investigation of RIE porous silicon could yield detailed information on the upper size limit of the pore that produces an effective MS-DIOS signal. These two approaches could lead to an increase in the size of the polymer chain grown as well as an enhancement in the MS-DIOS signal. A study of this nature could overcome the limitations described in chapter 2.

5.2 Systematic study of pore size in anodic aluminum oxide (AAO)

In chapter 3 we utilized an alternative substrate for the investigation of the confinement effect on pore grown polymer chains. Namely, AAO was explored as an alternative substrate to porous silicon for the homogeneous pores in AAO. While AAO cannot act as a matrix for in situ molecular weight characterization like p-Si, an ex situ characterization procedure was established and detailed in chapter 3. The development of the molecular weight characterization of AAO-grown PMMA allows for a more systematic study of the concave confinement of the pores on surface-initiated polymerization. Thus, a systematic examination that focuses on varying pore size while keeping polymerization times constant could be very beneficial in fully understanding the limitations placed on polymer chain growth inside a pore. Another variable that could be explored is the polymerization system. The polymerization media utilized throughout this work was water based. An organic based polymerization media could allow monomer and catalyst to be delivered inside

the pore more efficiently due to the decreased capillary effects associated with an organic solvent *versus* a more polar solvent system used in this work.

5.3 Replacement of porous silicon with AAO for water motion on wettability gradients

In chapter 4 we reported on the motion of water droplets on porous and flat silicon surfaces decorated with molecular gradients comprising semifluorinated (SF) organosilanes. We demonstrate that SF molecular gradients deposited on flat silica substrates facilitate faster motion of water droplets relative to the specimens covered with an analogous hydrocarbon gradient. Further increase in the drop speed is achieved by advancing the droplet along a porous substrate coated with a SF wettability gradient. An investigation of the viability of AAO as a replacement for p-Si could prove beneficial. The obvious improvement of AAO over porous silicon would be the homogeneous nature of the pores associated with AAO. The homogeneous nature of the pores would allow for a precise determination of the affect the fraction of air trapped under the liquid drop has on liquid motion. In addition, sample preparation time would be decreased and made more innocuous due to use of HF in the preparation of porous silicon. If the use of AAO was successful, a systematic study of pore size could be investigated. Current efforts in this area of the Gorman and Genzer groups are focused on changing the viscosity of the liquid used for motion on the wettability gradient. At present, the substrate investigated is flat silicon but could be expanded to include a study of porous substrate.

Appendix 1 – Schultz and “Point-by-Point” Distribution Fits

Each distribution is characterized by its weight-average molecular weight, \overline{M}_w , and number average molecular weight, \overline{M}_n . The ratio $\overline{M}_w/\overline{M}_n$ denotes the so-called polydispersity index (PDI). In general, each polymerization reaction yielded polymers that are controlled/”living” with a PDI less than 1.5. In the past, various empirical functions have been introduced to describe experimentally measured molecular weight distributions. One of them, suggested by Schulz, is a two-parameter most probable distribution having a general form:

$$w(N) = \frac{(-\ln p)^{k+1} N^k p^N}{\Gamma(k+1)} \quad , \quad (1)$$

where p and k are adjustable parameters, N is the degree of polymerization and Γ is the Gamma function. \overline{M}_w and \overline{M}_n are related to the p and k parameters through:

$$\overline{M}_n = -\frac{k}{\ln(p)} \quad , \quad (2)$$

$$\overline{M}_w = -\frac{k+1}{\ln(p)} \quad (3)$$

In addition to parameters p and k , a multiplication parameter (A) was used to match the weight fraction $w(N)$ with the experimental data sets.

The following equations were used to determine the weight-average molecular weight, \overline{M}_w , and number average molecular weight, \overline{M}_n using the so-called “point-by-point” distribution fit:

$$\overline{M}_n = \frac{1}{\sum_i \frac{w_i}{M_i}}, \quad (4)$$

$$\overline{M}_w = \sum w_i M_i, \quad (5)$$

where w_i is the weight fraction of the i -th component of the distribution having molecular weight of M_i .

The \overline{M}_w , \overline{M}_n , and PDI were determined from the MALDI data by first localizing the maxima of the intensity for each peak in the MALDI spectra and fitting them to equations 1-3 (Schultz distribution) and 4-5 (point-by-point method). As discussed in Chapters 2 and 3, two subsequent MALDI peaks were separated by the molecular weight of a single methyl methacrylate (MMA) repeat unit. The analysis of poly(methyl methacrylate) (PMMA) brushes prepared by grafting from polymerization of MMA on AAO was more challenging. In all samples, we identified multiple overlapping distributions our MALDI spectra. As discussed in detail in Chapter 3, these distributions (each of them having the expected resulted from different end groups present in the cleaved PMMA chains) resulted from different cleavage of the PMMA brushes from the AAO substrate. Each of the molecular weight distribution deconvoluted from the overall MALDI spectra was analyzed separately.

Appendix 2 – Mass Spectrometry Characterization of various Dendrimers via MALDI

Mass spectrometry analysis was carried out on a variety of dendrimers. The dendrimers included amphiphilic iron-sulfur core dendrimers (Generation 1, 2, and 3), a 3,5-aromatic and 2,6-aromatic iron-sulfur core dendrimer (Generation 2), and osmium and ruthenium tris(bipyridine) core dendrimers (Generation 1). The MALDI spectra are shown in Figures A2.1 through A2.7 in the order listed above. An Applied Biosystems Voyager STR MALDI-TOF mass spectrometer was used for the mass spectrometry analysis. All spectra were collected in positive ion mode except for the aromatic iron-sulfur core dendrimers. The aromatic iron-sulfur core dendrimers were collected in negative mode. In all cases, the matrix used was dithranol (99%, Aldrich) (0.2M in THF). The dendrimer was made to concentration of 5mg/mL in THF. The dendrimer was mixed with the dithranol solution in a 1 through 5 to 1 ratio of matrix to dendrimer and spotted on the target and allowed to evaporate. The iron-sulfur core dendrimers were oxygen sensitive and were prepared in a glove box. The accelerating voltage, grid voltage, and intensity of the laser played important roles in producing quality spectra. General parameters for quality spectra are:

$M_w < 10,000$ Da

Accelerating Voltage – 20,000-22,000 Volts

Grid Voltage – 90-95%

Laser Intensity – 1800 or lower

$M_w > 10,000$ Da

Accelerating Voltage – 22,000-25,000 Volts

Grid Voltage – 95-99%

Laser Intensity – 1900 or lower

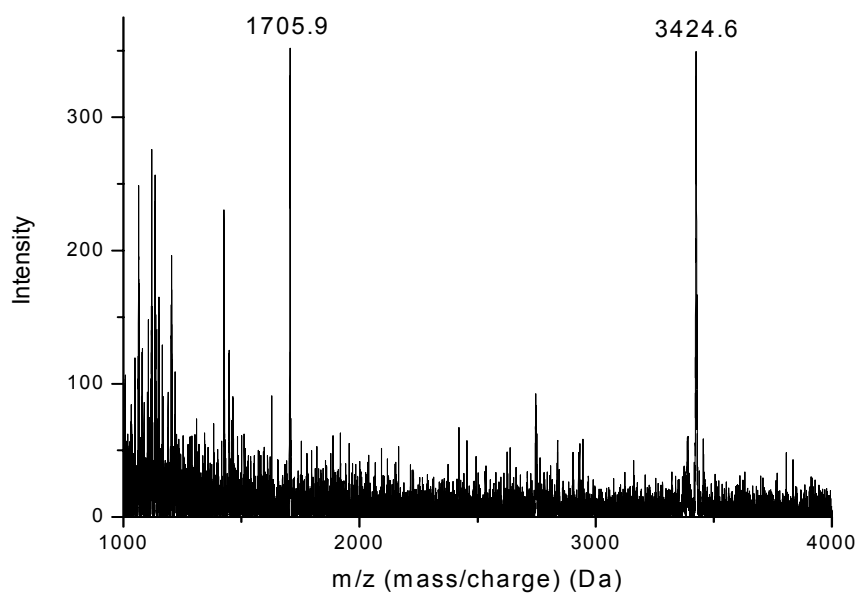


Figure A2.1 – Amphiphilic iron-sulfur core dendrimer (Generation 1)

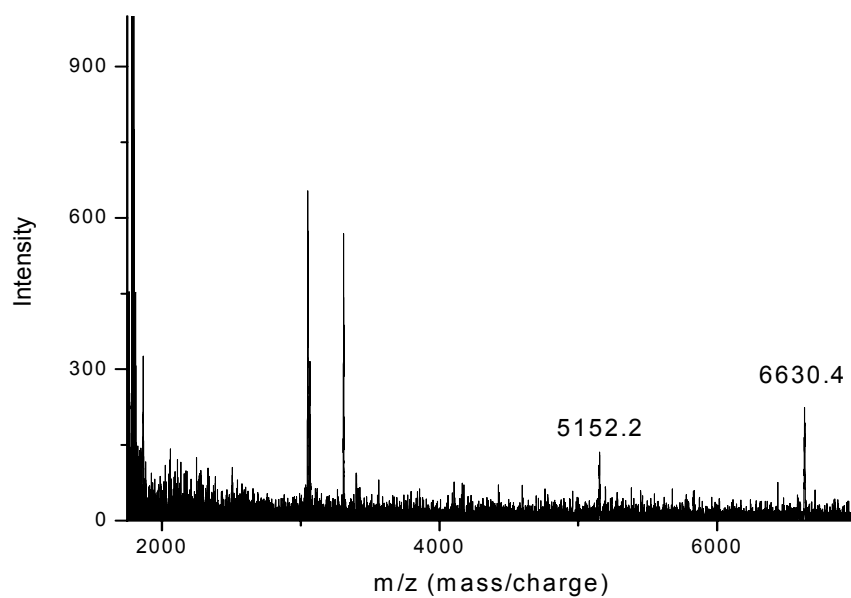


Figure A2.2 – Amphiphilic iron-sulfur core dendrimer (Generation 2)

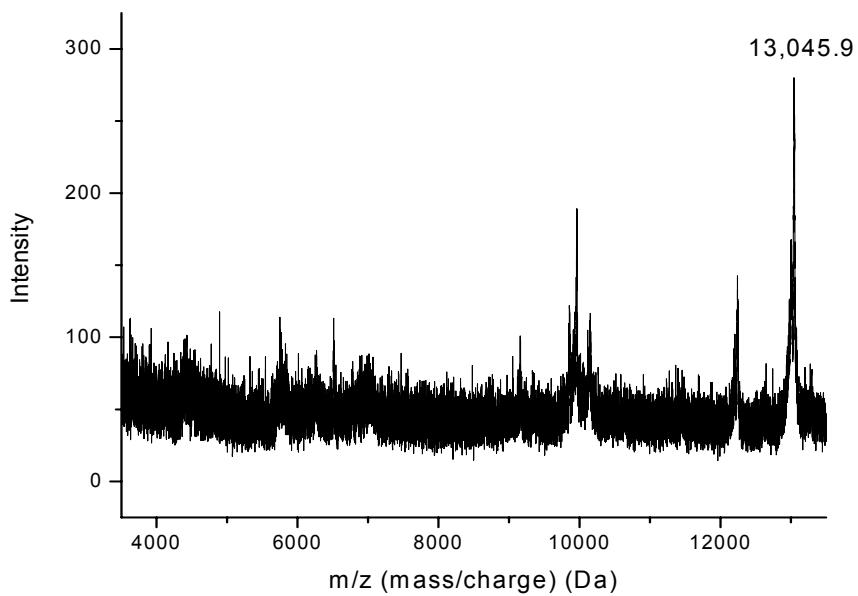


Figure A2.3 – Amphiphilic iron-sulfur core dendrimer (Generation 3)

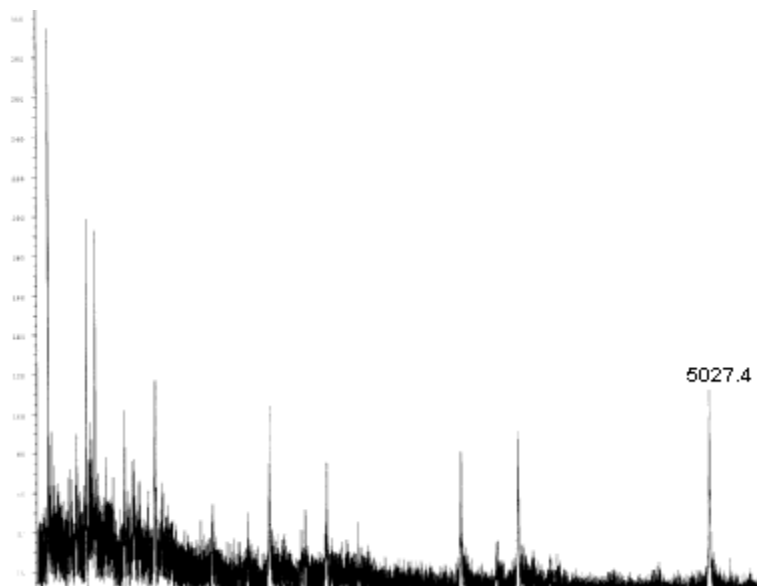


Figure A2.4 – 3,5-aromatic iron-sulfur core dendrimer (Generation 2)

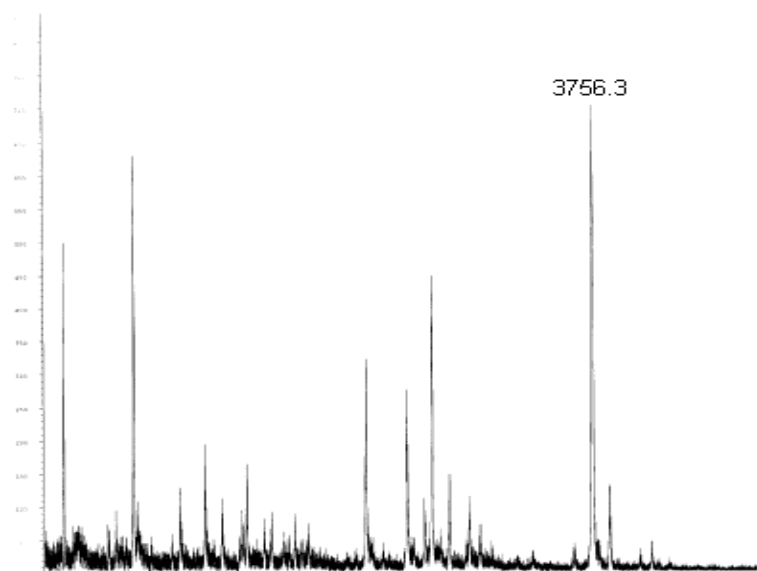


Figure A2.5 – 2,6-aromatic iron-sulfur core dendrimer (Generation 2)

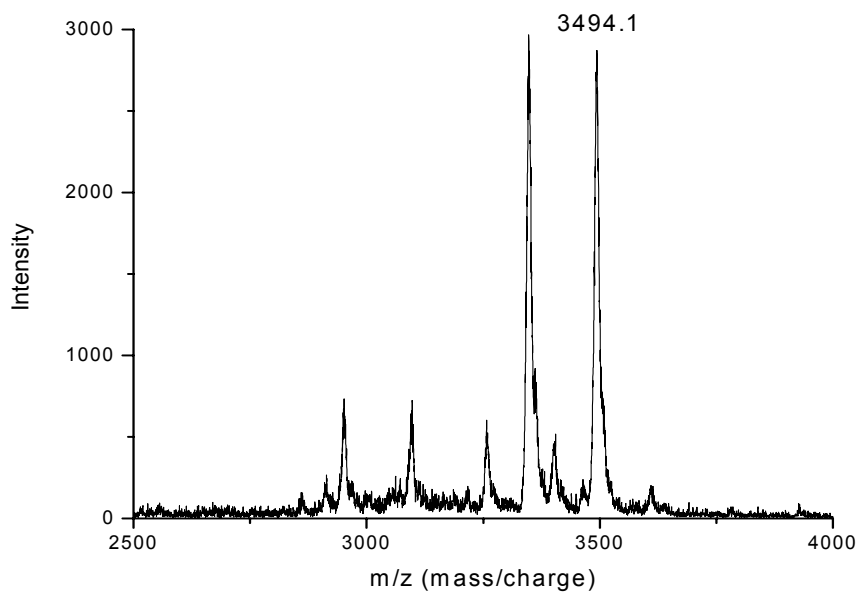


Figure A2.6 – Osmium Tris(bipyridine) core dendrimer (Generation 1)

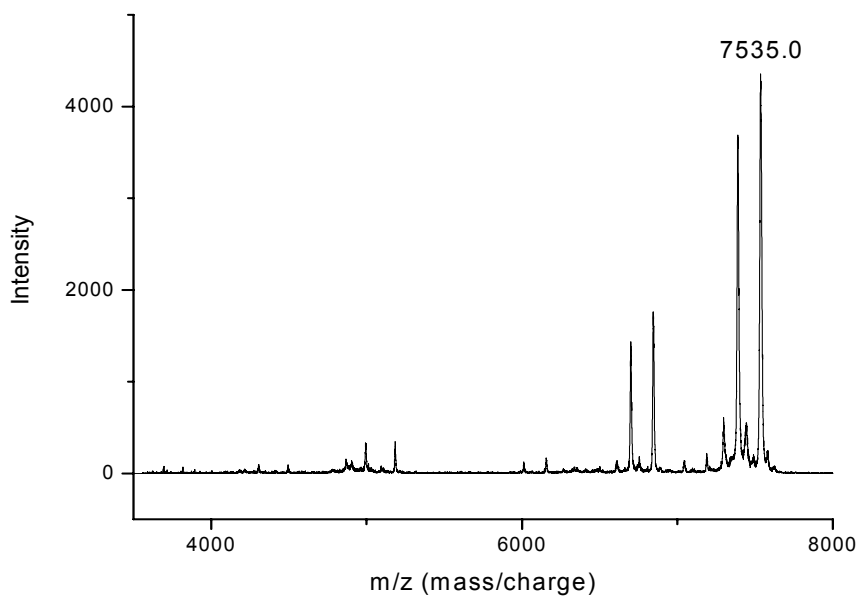


Figure A2.7 – Ruthenium Tris(bipyridine) core dendrimer (Generation 1)